Development and Applications of Nanofabricated Electrodes for Scanning Electrochemical Microscopy

by

Hui Xiong

BE, East China University of Science and Technology, 1998

MS, East China University of Science and Technology, 2000

Submitted to the Graduate Faculty of

Arts and Sciences in partial fulfillment

of the requirements for the degree of

Doctor of Philosophy

University of Pittsburgh

2007

UNIVERSITY OF PITTSBURGH

SCHOOL OF ARTS AND SCIENCES

This dissertation was presented

by

Hui Xiong

It was defended on

Dec 05, 2007

and approved by

Stephen G. Weber, Professor, Department of Chemistry

Adrian C. Michael, Associate Professor, Department of Chemistry

Minhee Yun, Assistant Professor, Department of Electrical & Computer Engineering

Dissertation Advisor: Shigeru Amemiya, Assistant Professor, Department of Chemistry

DEVELOPMENT AND APPLICATIONS OF NANOFABRICATED ELECTRODES FOR SCANNING ELECTROCHEMICAL MICROSCOPY

Hui Xiong, PhD

University of Pittsburgh, 2007

Over the last decade, dramatic progresses in fabrication and synthesis of nanomaterials have enabled reproducible and controlled production of nanometer-sized structures with desired size, shape, physical and chemical properties. Nanostructures created in this fashion are essential building blocks of complex nanosystems for various applications. In particular, electronically conductive nanostructures are attractive candidates as electrode materials for both fundamental studies and electrochemical applications in fields such as sensors, energy storage, functional molecular electronic devices, and electrocatalysis.

In my Ph.D. work, I explored frontiers in nanoscale electrochemistry utilizing novel electrode systems based on conductive nanostructures with shape and size controlled by advanced nanofabrication/synthesis methods. Specifically, I developed a new methodology based on scanning electrochemical microscopy (SECM) to discover that an individual one-dimensional nanostructure such as a metal nanoband and a single-walled carbon nanotube serves as a highly reactive electrode. This discovery is of great importance for future applications of the novel nanomaterials. Moreover, by integrating modern nanofabrication methods, I created nanometer-sized electrodes with controlled size and geometry. The significance of this achievement is that better spatial resolution will be obtainable by utilizing these nanofabricated electrodes as probes of SECM.

TABLE OF CONTENTS

LIST OF TABLES

LIST OF FIGURES

ACKNOWLEDGEMENTS

I would like to express my sincere gratitude to Professor Shigeru Amemiya for his guidance, support, and inspiration throughout my graduate research. I have been deeply impressed by his knowledge and enthusiasm toward scientific research and education. I believe that the experience in his group will be invaluable in my career as a professional scientist.

I would like to thank Professors Stephen Weber, Adrian Michael and Minhee Yun for serving on my committee and for their advice towards my education.

I would like to thank Dr. Jidong Guo for helpful discussions, support, and his invaluable friendship. I would also like to acknowledge all current and former members of Amemiya group for their supports: Gregg Kotchey, Jiyeon Kim, Darrick Gross, Dr. Yi Yuan, Patrick Rodgers, Yushin Kim, Dr. Eunkyoung Kim, Dr. Jing Ping, and Jing Wang.

I would like to thank the following groups and individuals for their help with different instruments and samples for my research: Asher group (sputtering), Mr. Chris Bowman and Mr. Tim Fisher at CMU (sputtering), Mr. Guy Lavallee at PSU, Kong group at MIT (samples of carbon nanotube), Weber group (samples of carbon fiber), Mr. Albert Stewart (SEM), Mr. Mike Mcdonald (NFCF).

I gratefully acknowledge the financial support from the University of Pittsburgh for an Andrew Mellon Predoctoral Fellowship.

I would also like to thank all my friends for listening to me whenever I want to share the happiness or seek for comforts at hard times.

Last but not least, I would like to thank my family for their support, trust, and unconditional love.

1. INTRODUCTION TO SCANNING ELECTROCHEMICAL MICROSCOPY

Part of this chapter has been published as S. Amemiya, J. Guo, H. Xiong, D.A. Gross, *Anal. Bioanal. Chem.* 2006, 386, 458-471.

A combination of scanning electrochemical microscopy (SECM) and the nanofabricated/synthesized electrode systems is of fundamental importance. SECM is advantageous, in principle, for allowing spatially resolved characterization of the nanostructured electrode systems, which are not accessible by traditional electrochemical methods. Moreover, while SECM has been versatile in studying various interfaces such as liquid/liquid, solid/liquid, and gas/liquid interfaces at micrometer scale, nanoelectrodes produced by advanced nanofabrication methods as SECM probes increase the spatial resolution of SECM to nanometer scale to obtain more insights into the important interface systems.

Here we introduce the basic principles of SECM, which are useful for above-mentioned nanoscale studies. SECM (the same acronym is also used for the instrument, i.e., the microscope) is a scanning probe technique, which is based on scanning a small tip, i.e., ultramicroelectrode (UME; an electrode with one dimension of 25 μm or smaller), in close vicinity of the surface of a substrate in an electrochemical cell setup. SECM is a “chemical microscope”[1] which provides a spatially resolved view of both chemical reactivity and topographic information of a substrate. In SECM experiments (Figure 1-1), an UME tip is brought near the substrate surface, where the electrochemical response at the tip is recorded as a function of the lateral tip position (x, y) for imaging, of the tip-substrate separation (z) in approach curve measurements, or of time at a fixed tip position in chronoamperometry. In this chapter we present principles of primary working modes of SECM, in particular, we explain the most commonly used feedback operation mode and imaging mode in details.

1.1 OPERATIONAL MODES OF SECM

Several SECM operational modes have been developed since its introduction in 1989.[2] The main modes of operation of SECM are based on amperometric measurements at the UME probe. When a redox-active molecule (mediator) is electrolyzed at a diffusion-limited rate at an UME (e.g. a disk UME) in the bulk solution ($O + ne^- \rightarrow R$; Figure 1-2a), the steady-state limiting current at the tip of a disk UME, $i_{T,\infty}$, is given by

$$i_{T,\infty} = 4nFDc_0a \tag{1}$$

where n is the stoichiometric number of electrons transferred in the tip reaction, F is the Faraday constant, D and c_0 are the diffusion coefficient and the concentration of the redox molecule in the bulk solution, respectively, and a is the disk radius. While Eq. (1) holds for a disk-shaped UME, similar equations hold for UMEs of other geometry.

When the tip is brought to close vicinity of the substrate, the tip current is perturbed by the substrate. A plot of the tip current, i_T, versus the tip-substrate distance, d, is called an

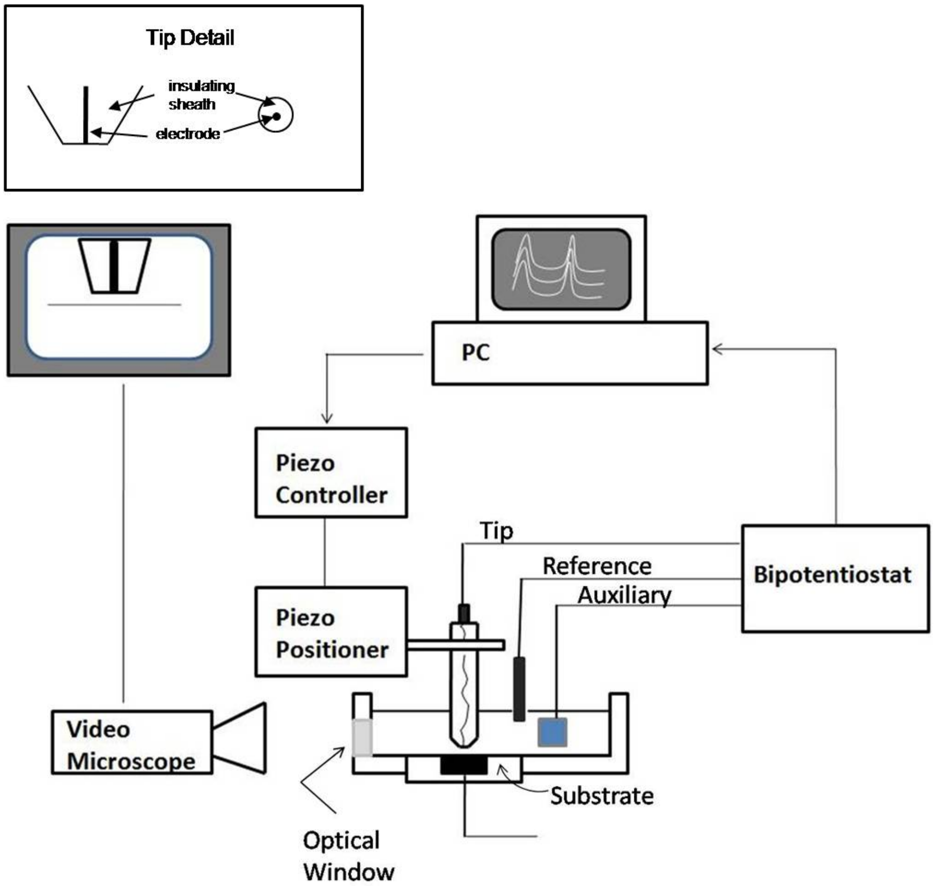

Figure 1-1. Schematic diagram of a SECM apparatus.

(A) diffusion-limited current in bulk solution

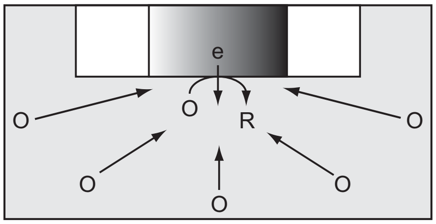

(B) negative feedback mode

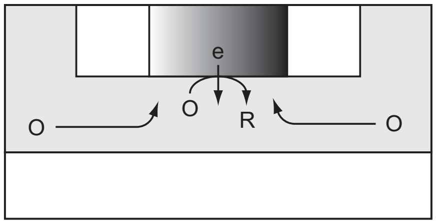

(C) positive feedback mode

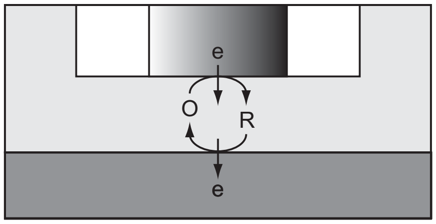

(D) SECM-induced transfer mode

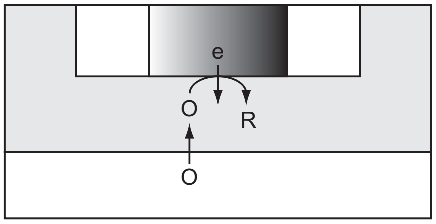

(E) SG/TC mode

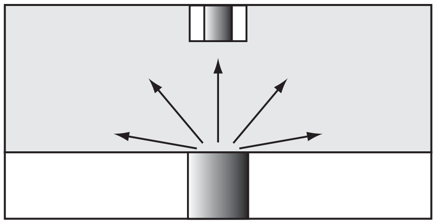

Figure 1-2a-e. Principles of SECM, showing (a) hemispherical diffusion to the disk-shaped tip positioned far from the substrate, (b) the negative feedback mode based on hindered diffusion by insulating substrate, (c) the positive feedback mode at a conductive substrate, (d) the SECM-induced transfer mode at the interface between two immiscible liquid phases, and (e) the substrate generation/tip collection mode.

approach curve, which can be used to determine the surface reactivity from the shape of the curve and the tip-substrate separation from the tip current. In the following, we introduce the main operational modes that have been used to various SECM studies.

1.1.1 Feedback mode

The feedback modes of SECM are based on negative and positive feedback effects, which are observed when an UME probe approaches within a short tip-substrate distance (usually approximately the tip diameter; $d < 2a$) to insulating and conductive substrates, respectively.[3, 4] As the tip is brought close to an insulating substrate, the tip current decreases monotonically, since diffusion of the redox mediator from bulk solution to the tip is hindered by the inert substrate (Figure 1-2b; negative feedback effect). At an insulating substrate that is much larger than the tip, the tip current decreases monotonically toward zero as the tip-substrate distance approaches zero (bottom curve in Figure 1-3). Therefore, the negative feedback mode can be used to determine the tip-substrate distance from the tip current and also to obtain the substrate topography in SECM imaging.

A positive feedback effect is observed when the probe approaches a conductive substrate, where the mediator is regenerated (Figure 1-2c). While diffusion of redox-active mediator molecule from the bulk solution to the tip is hindered more significantly at a shorter tip-substrate distance, efficient redox cycling based on planar mediator diffusion in the gap between the tip and the substrate amplifies the tip current as the gap becomes smaller. When the mediator regeneration on the substrate surface is limited by mediator diffusion in the tip-substrate gap, the largest tip response that corresponds to the top curve in Figure 1-3 is observed.

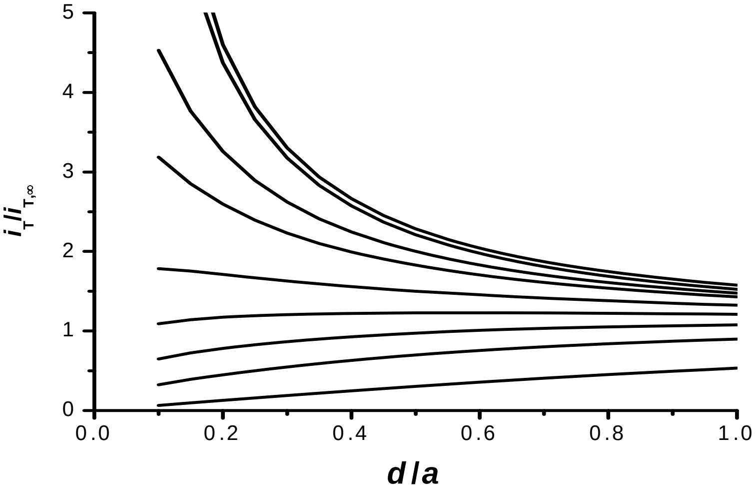

Figure 1-3. SECM approach curves as a function of the apparent heterogeneous rate constant for electrochemically irreversible electron transfer at the substrate, k_f (cm/s). The normalized rate constant, $k_f a/D$, is ∞ (positive feedback), 100, 10, 5, 2, 1, 0.5, 0.2, and 0 (negative feedback) from the top (ref 7).

Therefore, SECM allows discrimination of insulating and conductive surfaces. Importantly, the tip current at a given tip-substrate distance is smaller when the surface is less reactive (Figure 1-3), since the mediator regeneration reaction on the substrate surface is kinetically limited.[5] In this case, theoretical analysis of an approach curve allows the electron-transfer reaction rate to be determined.[6, 7]

1.1.2 SECM-induced transfer (SECMIT) mode

Molecular transport across an interface between two immiscible liquid phases can be studied using the SECMIT mode.[8] This principle was proposed in a SECM study of a lipid bilayer membrane by Matsue and coworkers[9] and then established later by Unwin and coworkers using unmodified or lipid monolayer-modified interfaces between liquid/liquid and air/liquid phases.[10, 11] In the SECMIT mode (Figure 1-2d), an UME probe is brought to the interface between two phases, where a redox-active molecule is partitioned at the equilibrium. The tip current can be enhanced even without mediator regeneration based on a redox reaction at the interface, because the bottom phase serves as a reservoir of the redox species. When the redox molecule is electrolyzed at the tip to be depleted locally, the tip-induced concentration gradient drives molecular flux across the interface, enhancing the tip current. The rate of interfacial transfer of the redox species can be determined from an approach curve.[10] Moreover, the diffusion coefficient and concentration of the transferred molecule at the opposite side of the interface can be determined from chronoamperometric measurements of the transient and steady-state tip currents at a known tip-interface distance without contact from the tip.[10]

1.1.3 Substrate-generation/tip-collection (SG/TC) mode

Another important operational mode of SECM is the SG/TC mode.[12] In this mode, the SECM probe is used to monitor a concentration gradient of a species generated at the substrate surface (Figure 1-2e). When a small probe is positioned at a tip-substrate distance that is much larger than the probe diameter, the tip current is given by Eq.1, allowing for determination of the local concentration of the substrate-generated species at the tip position. At a shorter tip-substrate distance, the tip response is based on the convolution of the feedback effect and the local concentration gradient, which complicates quantitative data analysis.[13] Most experiments based on SG/TC mode have been carried out by positioning a very small probe far from the substrate surface. Since this type of SG/TC mode does not reply on a feedback effect, probes such as potentiometric ion-selective microelectrodes[14] and biosensor probes[15] can also used.

1.2 SECM IMAGING

In most SECM imaging experiments,[16] the tip rather than the substrate is moved using motorized positioners such as piezoelectric motors and "inchworm" motors (Figure 1-1). The spatial resolution of the motors is high in comparison with the sizes of standard SECM probes (tip diameter 2-25 μm). The spatial resolution of SECM is mainly governed by the tip size, i.e., a smaller probe offers a higher spatial resolution. The shape of the tip also affects the spatial resolution, i.e., a disk-shaped tip provides a higher spatial resolution than tips with other geometry (e.g., cone, hemisphere, and ring). Besides the probe size and shape, the tip-substrate distance is another key issue in SECM imaging; the tip must be positioned and maintained in close proximity to the substrate to obtain a high-resolution image. A small tip outer diameter is necessary to approach the electrode near the surface. The ratio of the size of the insulating sheath to the radius of the metal core (i.e., RG) of an UME is always minimized to a value that is below 10. Meanwhile, knowledge of the tip-substrate distance is necessary to determine the surface reactivity from the tip current response in a SECM image; approach curve measurement is a more straightforward way to obtain this parameter.

1.2.1 Constant height imaging

Most SECM imaging experiments are carried out in constant height mode,[17] where a probe is moved only laterally in the *x* and *y* directions. This imaging mode is usually adequate for a flat surface or for SG/TC mode with a probe positioned far from the surface. The constant height mode, however, is problematic for high-resolution imaging of a surface with a high relief, which is the case of imaging a single cell on a solid surface.[18] With constant-height imaging of a rough surface, a change in the tip current is due to changes not only in the surface reactivity but also in the tip–substrate distance. Moreover, the spatial resolution is usually compromised by use of a relatively large tip. The tip size needs to be comparable to or larger than the cell height to image a large area of the surface by maintaining the tip–substrate distance within the working distance (usually about the tip diameter). Use of a smaller probe in constant-height mode suffers from a shorter working distance and even from tip crash.

1.2.2 Constant distance imaging: electrochemical approach

To overcome the limitations of constant-height imaging, a variety of approaches for constant distance imaging were developed. With this imaging mode, a distance-dependent signal is used as a feedback signal to maintain the probe at a constant distance from the substrate surface during the raster. The feedback signal is an electrochemical response of the probe or a signal based on a physical interaction between the tip and substrate.

The simplest approach to constant-distance imaging is a constant-current mode [19], where the tip current is used as a feedback signal. Constant-current imaging is straightforward when the substrate surface consists of only insulating or only conducting materials, due to the 1:1 correspondence between the tip current and the tip–substrate distance (top and bottom curves in **Error! Reference source not found.**). In these cases, the constant-distance image reflects the surface topography of the substrate. Constant-current imaging over mixed insulating and conducting materials is also possible using tip-position modulation technique [19, 20] or picking mode [21].

Another electrochemical approach is to use AC impedance of the SECM tip as a feedback signal.[22] This approach was originally developed to allow a probe to be positioned in the vicinity of the surface when distance control based on a current feedback effect is not applicable, e.g., for biosensor tips[15] and potentiometric ion-selective microelectrodes.[23, 24] With this mode, a high-frequency alternating potential is applied to measure the resistance between the tip and a counter electrode. While the distance dependence for a conductive substrate is complicated,[25, 26] the negative feedback behavior of the impedance response over an insulating substrate allows for constant distance imaging, yielding a topographic image based on the vertical tip displacement.[22] In contrast to the constant current mode, the impedance technique requires no redox-active molecule and also enables simultaneous measurement of the Faradic tip response. Impedance-based imaging has been used to map active spots on surfaces.[27-30]

1.2.3 Constant distance imaging: shear force-based approach

Constant distance imaging has also been demonstrated using a shear force-based mechanism, which was developed to enable the positioning of an optical fiber probe in near-field scanning optical microscopy.[31] Using this technique, a SECM probe is vibrated near the surface so that the tip–substrate distance is controlled by monitoring the damping of the oscillations due to shear forces between the tip and the sample surface. The distance-dependent feedback signal, which has a very short working distance (~ 20 nm in air), can be detected using an optical [32] or tuning-fork [33] technique. Schuhmann and co-workers were the first to demonstrate that such a vibration affects the tip current only slightly, making simultaneous measurements of approach curves based on the tip current and the vibration amplitude possible.[34] In their set-up, the damping of the amplitude upon approach of a laterally vibrating tip to the surface is detected optically, where a laser beam is focused on the tip to create a diffraction pattern that is monitored with a photodiode detector. The optical shear-force-based approach was successfully used for depositing three-dimensional polypyrrole structures [35], constant-distance imaging [36], and positioning an enzyme-filled capillary tip [36].

Due to the complicated instrumentation and operation required for the optical detection, a non-optical shear-force detection based on the tuning fork (and its analogous) technique has been also applied for SECM.[37] With this technique, a SECM tip is attached to the side of one of the prongs of a quartz crystal tuning fork. The mechanical resonance of the fork is excited with a piezoelectric tube so that the tuning fork and the tip are vibrated parallel to the sample surface. Since both prongs are also piezoelectrically coupled, the damping of the oscillations can be monitored as a change in the corresponding piezoelectric signal. Smyrl and co-workers introduced the tuning fork technique for constant-distance SECM imaging.[37, 38] The tip positioning technique was also used by others for imaging by scanning optical microscopy based on electrogenerated chemiluminescence at the nanoelectrode probe as a light source,[39] and combined scanning electrochemical/optical microscopy,[40] as well as for constant distance SECM imaging of enzyme-modified surfaces.[41, 42] Schuhmann and co-workers reported a similar approach using two piezoelectric plates attached to a SECM probe for tip excitation and oscillation detection, respectively[43] This approach was applied for constant distance imaging of a lithographically fabricated microband electrode array,[43] for monitoring dissolution of a calcium carbonate shell of *Mya arenaria* using a Ca^{2+}-selective micropipet electrode,[44] and for identifying amino groups in the wood sample labeled with glucose oxidase.[45] The usefulness of shear force-based positioning of nanometer-sized probes was also demonstrated via an improved spatial resolution in constant distance imaging with a 450-nm-diameter Pt electrode[46] as well as in metal deposition with 200–500-nm-diameter amperometric glass pipette electrodes.[47] It should be noted that the shear force-based approaches are sensitive to the distance between the substrate and insulating sheath of the SECM tip, rather than that between the substrate the active part of the tip, because of the imperfect tip–substrate alignment.[40] Therefore, the "true" tip–substrate distance is larger than the working distance of the shear force feedback, so positioning a larger probe using the shear force-feedback mode is more difficult.[42]

Finally, combined scanning electrochemical/atomic force microscopy is another important approach for distance control in SECM imaging.[48] In this technique, an UME is integrated into an AFM cantilever manually[49-52] or by using modern nanofabrication methods.[53-58] The technique is powerful enough to probe diffusional molecular flux even through an individual nanopore in artificial membranes.[59, 60]

REFERENCES

(1) Bard, A. J.; Fan, F.-R.; Pierce, D. T.; Unwin, P. R.; Wipf, D. O.; Zhou, F. *Science* **1991**, *254*, 68-74.

(2) Bard, A. J.; Fan, F.-R. F.; Kwak, J.; Lev, O. *Anal. Chem.* **1989**, *61*, 132–138.

(3) Bard, A. J.; Fan, F. R. F.; Kwak, J.; Lev, O. *Anal. Chem.* **1989**, *61*, 132-138.

(4) Kwak, J.; Bard, A. J. *Anal. Chem.* **1989**, *61*, 1221-1227.

(5) Bard, A. J.; Faulkner, L. R. *Electrochemical Methods: Fundamentals and Applications*, 2nd ed.; John Wiley & Sons: New York, 2001.

(6) Bard, A. J.; Mirkin, M. V.; Unwin, P. R.; Wipf, D. O. *J. Phys. Chem.* **1992**, *96*, 1861-1868.

(7) Wei, C.; Bard, A. J.; Mirkin, M. V. *J. Phys. Chem.* **1995**, *99*, 16033-16042.

(8) Barker, A. L.; Gonsalves, M.; Macpherson, J. V.; Slevin, C. J.; Unwin, P. R. *Anal. Chim. Acta* **1999**, *385*, 223–240.

(9) Yamada, H.; Matsue, T.; Uchida, I. *Biochem. Biophys. Res. Commun.* **1991**, *180*, 1330–1334.

(10) Barker, A. L.; Macpherson, J. V.; Slevin, C. J.; Unwin, P. R. *J. Phys. Chem. B* **1998**, *102*, 1586–1598.

(11) Barker, A. L.; Unwin, P. R. *J. Phys. Chem. B* **2001**, *105*, 12019-12031.

(12) Engstrom, R. C.; Pharr, C. M. *Anal. Chem.* **1989**, *61*, 1099A–1104A.

(13) Martin, R. D.; Unwin, P. R. *Analytical Chemistry* **1998**, *70*, 276-284.

(14) Horrocks, B. R.; Mirkin, M. V.; Pierce, D. T.; Bard, A. J.; Nagy, G.; Tóth, K. *Anal. Chem.* **1993**, *65*, 1213–1224.

(15) Horrocks, B. R.; Schmidtke, D.; Heller, A.; Bard, A. J. *Anal. Chem.* **1993**, *65*, 3605–3614.

(16) Fan, F.-R. F. In *Scanning Electrochemical Microscopy*; Bard, A. J., Mirkin, M. V., Eds.; Marcel Dekker: New York, 2001, pp 111–143.

(17) Kwak, J.; Bard, A. J. *Anal. Chem.* **1989**, *61*, 1794–1799.

(18) Bauermann, L. P.; Schuhmann, W.; Schulte, A. *Phys. Chem. Chem. Phys.* **2004**, *6*, 4003-4008.

(19) Wipf, D. O.; Bard, A. J.; Tallman, D. E. *Anal. Chem.* **1993**, *65*, 1373–1377.

(20) Wipf, D. O.; Bard, A. J. *Anal. Chem.* **1992**, *64*, 1362–1367.

(21) Borgwarth, K.; Ebling, D. G.; Heinze, J. *Ber. Bunsen-Ges. Phys. Chem.* **1994**, *98*, 1317-1321.

(22) Alpuche-Aviles, M. A.; Wipf, D. O. *Anal. Chem.* **2001**, *73*, 4873–4881.

(23) Wei, C.; Bard, A. J.; Nagy, G.; Tóth, K. *Anal. Chem.* **1995**, *67*, 1346–1356.

(24) Kashyap, R.; Gratzl, M. *Anal. Chem.* **1999**, *71*, 2814–2820.

(25) Baranski, A. S.; Diakowski, P. M. *J. Solid State Electrochem.* **2004**, *8*, 683-692.

(26) LeSuer, R. J.; Fan, F. R. F.; Bard, A. J. *Analytical Chemistry* **2004**, *76*, 6894-6901.

(27) Katemann, B. B.; Schulte, A.; Calvo, E. J.; Koudelka-Hep, M.; Schuhmann, W. *Electrochemistry Communications* **2002**, *4*, 134-138.

(28) Etienne, M.; Schulte, A.; Schuhmann, W. *Electrochemistry Communications* **2004**, *6*, 288-293.

(29) Gabrielli, C.; Huet, F.; Keddam, M.; Rousseau, P.; Vivier, V. *J. Phys. Chem. B* **2004**, *108*, 11620-11626.

(30) Gabrielli, C.; Ostermann, E.; Perrot, H.; Vivier, V.; Beitone, L.; Mace, C. *Electrochemistry Communications* **2005**, *7*, 962-968.

(31) Dunn, R. C. *Chem. Rev.* **1999**, *99*, 2891–2927.

(32) Betzig, E.; Finn, P. L.; Weiner, J. S. *Applied Physics Letters* **1992**, *60*, 2484-2486.

(33) Karrai, K.; Grober, R. D. *Applied Physics Letters* **1995**, *66*, 1842-1844.

(34) Ludwig, M.; Kranz, C.; Schuhmann, W.; Gaub, H. E. *Rev. Sci. Instrum.* **1995**, *66*, 2857–2860.

(35) Kranz, C.; Gaub, H. E.; Schuhmann, W. *Adv. Mater.* **1996**, *8*, 634–637.

(36) Hengstenberg, A.; Kranz, C.; Schuhmann, W. *Chem. Eur. J.* **2000**, *6*, 1547–1554.

(37) James, P. J.; Garfias-Mesias, L. F.; Moyer, P. J.; Smyrl, W. H. *J. Electrochem. Soc.* **1998**, *145*, L64–L66.

(38) Büchler, M.; Kelley, S. C.; Smyrl, W. H. *Electrochem. Solid-State Lett.* **2000**, *3*, 35–38.

(39) Zu, Y.; Ding, Z.; Zhou, J.; Lee, Y.; Bard, A. J. *Anal. Chem.* **2001**, *73*, 2153–2156.

(40) Lee, Y.; Ding, Z.; Bard, A. J. *Anal. Chem.* **2002**, *74*, 3634–3643.

(41) Oyamatsu, D.; Hirano, Y.; Kanaya, N.; Mae, Y.; Nishizawa, M.; Matsue, T. *Bioelectrochem. Bioenerg.* **2003**, *60*, 115-121.

(42) Yamada, H.; Fukumoto, H.; Yokoyama, T.; Koike, T. *Analytical Chemistry* **2005**, *77*, 1785-1790.

(43) Katemann, B. B.; Schulte, A.; Schuhmann, W. *Chemistry-a European Journal* **2003**, *9*, 2025–2033.

(44) Etienne, M.; Schulte, A.; Mann, S.; Jordan, G.; Dietzel, L. D.; Schuhmann, W. *Analytical Chemistry* **2004**, *76*, 3682-3688.

(45) Garay, M. F.; Ufheil, J.; Borgwarth, K.; Heinze, J. *Physical Chemistry Chemical Physics* **2004**, *6*, 4028-4033.

(46) Katemann, B. B.; Schulte, A.; Schuhmann, W. *Electroanalysis* **2004**, *16*, 60-65.

(47) Turyan, I.; Etienne, M.; Mandler, D.; Schuhmann, W. *Electroanalysis* **2005**, *17*, 538-542.

(48) Gardner, C. E.; Macpherson, J. V. *Anal. Chem.* **2002**, *74*, 576A-584A.

(49) Macpherson, J. V.; Unwin, P. R. *Anal. Chem.* **2000**, *72*, 276–285.

(50) Jones, C. E.; Macpherson, J. V.; Barber, Z. H.; Somekh, R. E.; Unwin, P. R. *Electrochemistry Communications* **1999**, *1*, 55-60.

(51) Macpherson, J. V.; Unwin, P. R. *Anal. Chem.* **2001**, *73*, 550–557.

(52) Abbou, J.; Demaille, C.; Druet, M.; Moiroux, J. *Analytical Chemistry* **2002**, *74*, 6355-6363.

(53) Kranz, C.; Friedbacher, G.; Mizaikoff, B.; Lugstein, A.; Smoliner, J.; Bertagnolli, E. *Anal. Chem.* **2001**, *73*, 2491–2500.

(54) Lugstein, A.; Bertagnolli, E.; Kranz, C.; Kueng, A.; Mizaikoff, B. *Applied Physics Letters* **2002**, *81*, 349-351.

(55) Lugstein, A.; Bertagnolli, E.; Kranz, C.; Mizaikoff, B. *Surf. Interface Anal.* **2002**, *33*, 146-150.

(56) Fasching, R. J.; Tao, Y.; Prinz, F. B. *Sensors And Actuators B-Chemical* **2005**, *108*, 964-972.

(57) Dobson, P. S.; Weaver, J. M. R.; Holder, M. N.; Unwin, P. R.; Macpherson, J. V. *Anal. Chem.* **2005**, *77*, 424-434.

(58) Gullo, M. R.; Frederix, P. L. T. M.; Akiyama, T.; Engel, A.; deRooij, N. F.; Staufer, U. *Anal. Chem.* **2006**, *78*, 5436-5442.

(59) Macpherson, J. V.; Jones, C. E.; Barker, A. L.; Unwin, P. R. *Anal. Chem.* **2002**, *74*, 1841–1848.

(60) Kueng, A.; Kranz, C.; Lugstein, A.; Bertagnolli, E.; Mizaikoff, B. *Angewandte Chemie-International Edition* **2005**, *44*, 3419-3422.

2. INTRODUCTION TO ONE-DIMENSIONAL NANOSTRUCTURES

One-dimensional (1D) nanostructures are wires, rods, belts, and tubes whose lateral dimensions fall anywhere in the range of 1 to 100 nm.[1] Over the past 20 years, 1D nanostructures such as carbon nanotubes (CNTs), metal and semiconducting nanowires, nanbands have gained growing interests owing to their unique electronic, thermal, optical, mechanical, and chemical properties superior to their bulk counterparts.[1-5]

Conductive 1D nanostructures are attractive electrode materials for applications such as molecular electronics,[6] sensors,[7, 8] catalysis,[9] and energy storage and conversion.[10] In fact, nanometer-sized electrodes with a high aspect ratio have been studied for their high charge-carrying capacity at the electrode/electrolyte solution interface.[11-13] However, 1D nanostructures and most of the applications derived from these materials are still in the early stage of development. Hence, it is very important to characterize electrochemical property of 1D nanostructures before these nanostructured electrode materials could be utilized to their full potential. Moreover, individual nanostructure might differ from each other, for example, CNT can be either metallic or semiconducting depending on structure.[2] This raises challenges in characterization of individual behaviors of 1D nanostructures with mixed properties at the small dimension. While traditional electrochemical measurements lack the ability to provide spatially resolved information of 1D nanostructures, SECM, on the other hand, is superb in allowing spatially resolved electrochemical measurements but it has not been applied to the studies of individual 1D nanostructures. Here in the following chapters I introduce my work in utilizing SECM for the first time to study individual 1D nanostructures.

REFERENCES

(1) Xia, Y. N.; Yang, P. D.; Sun, Y. G.; Wu, Y. Y.; Mayers, B.; Gates, B.; Yin, Y. D.; Kim, F.; Yan, Y. Q. *Adv. Mater.* **2003**, *15*, 353-389.

(2) Baughman, R. H.; Zakhidov, A. A.; de Heer, W. A. *Science* **2002**, *297*, 787-792.

(3) Ouyang, M.; Huang, J. L.; Lieber, C. M. *Acc. Chem. Res.* **2002**, *35*, 1018-1025.

(4) Law, M.; Goldberger, J.; Yang, P. *Annual Review of Materials Research* **2004**, *34*, 83-122.

(5) Huang, X.-J.; Choi, Y.-K. *Sensors and Actuators B: Chemical* **2007**, *122*, 659-671.

(6) Avouris, P. *Accounts Of Chemical Research* **2002**, *35*, 1026–1034.

(7) Wang, J. *Electroanalysis* **2005**, *17*, 7–14.

(8) Kolmakov, A.; Moskovits, M. *Annu. Rev. Mater. Sci.* **2004**, *34*, 151–180.

(9) Girishkumar, G.; Vinodgopal, K.; Kamat, P. V. *J. Phys. Chem. B* **2004**, *108*, 19960–19966.

(10) Che, G.; Lakshmi, B. B.; Fisher, E. R.; Martin, C. R. *Nature* **1998**, *393*, 346–349.

(11) Wehmeyer, K. R.; Deakin, M. R.; Wightman, R. M. *Anal. Chem.* **1985**, *57*, 1913–1916.

(12) Bond, A. M.; Henderson, T. L. E.; Thormann, W. *J. Phys. Chem.* **1986**, *90*, 2911–2917.

(13) Leiva, E. P. M.; Sanchez, C. G.; Velez, P.; Schmickler, W. *Phys. Rev. B* **2006**, *74*, 035422.

3.0 LOCAL FEEDBACK MODE OF SCANNING ELECTROCHEMICAL MICROSCOPY FOR ELECTROCHEMICAL CHARACTERIZATION OF ONE-DIMENSIONAL NANOSTRUCTURE: THEORY AND EXPERIMENT WITH NANOBAND ELECTRODE AS MODEL SUBSTRATE

This work has been published as Hui Xiong, Darrick A. Gross, Jidong Guo, and Shigeru Amemiya, *Anal. Chem.,* 2006, 78, 1946-1957.

3.1 ABSTRACT

Local feedback mode is introduced as a novel operation mode of scanning electrochemical microscopy (SECM) for electrochemical characterization of a single one-dimensional (1D) nanostructure, *e.g.*, a wire, rod, band, and tube with 1–100 nm width and micrometer to centimeter length. To demonstrate the principle, SECM feedback effects under diffusion limitation were studied theoretically and experimentally with a disk probe brought near a semi-infinitely long band electrode as a geometrical model for a conductive 1D nanostructure. As the band becomes narrower than the disk diameter, the feedback mechanism for tip current enhancement is predicted to change from standard positive feedback mode, to positive local-

feedback mode, and then to negative local-feedback mode. The negative local-feedback effect is the only feedback effect that allows observation of a 1D nanostructure without serious limitations due to small lateral dimension, available tip size, or finite electron transfer rate. In line-scan and approach-curve experiments, an unbiased Pt band electrode with 100-nm width and 2.6-cm length was detectable in negative local feedback mode, even using a 25-µm-diameter disk Pt electrode. Using a 2-µm-diameter probe, both well-defined and defected sites were observed in SECM imaging based on local electrochemical activity of the nanoband electrode. Non-contact and spatially-resolved measurement is an advantage of this novel SECM approach over standard electrochemical approaches using electrodes based on 1D nanostructure.

3.2 INTRODUCTION

There has been an increasing interest in electrochemistry for nanoscience and nanotechnology,[1] for instance, electrochemical measurement[2] and theory[3] at nanometer scale and electrochemical synthesis and characterization of nanomaterials.[4–6] Scanning electrochemical microscopy (SECM)[7,8] offers significant advantages for electrochemical studies of nanosystems. In standard SECM experiments, an amperometric response of an ultramicroelectrode (UME) positioned in a vicinity of a substrate surface is studied to probe heterogeneous reactions at the surface or homogeneous reactions in the gap between the tip and the substrate. Spatially-resolved nanoscale measurement is possible using a nanoelectrode as a SECM probe.[9–16] Fast steady-state mass transport in the nanogap is advantageous for kinetic studies of fast heterogeneous[17] and homogeneous[18] reactions. Moreover, SECM allows non-contact electrochemical characterization of nanostructured substrates such as an array of protein nanopores[19] and an array of monolayer-protected metallic nanoparticles.[20]

Here we introduce a "local" feedback effect as a basis of a novel operation mode for SECM. This operation mode is useful for electrochemical studies of one-dimensional (1D) nanostructures such as a wire, rod, band, and tube with the width of 1 to 100 nm and the length of micrometers to centimeters. Besides carbon nanotube,[21] a variety of 1D nanostructures based on inorganic[22] and organic[23] materials have been synthesized or fabricated over the last fifteen years. Many of these nanostructures with unique physical and chemical properties are attractive electrode materials for molecular electronics,[24] sensors,[25,26] catalysis,[27] and energy storage and conversion.[28] Electrochemical characterization of the nanomaterials, however, is challenging because of the small dimension. Although electrodes based on bulk and single 1D nanostructures such as carbon nanotubes can be prepared by traditional manual or chemical methods,[28–30] modern nanofabrication techniques,[31,32] or modification of electrode surface with the materials,[33,34] influence of these fabrication procedures on the structure and reactivity of the nanomaterial surface is not known. In addition, the geometry and size of the active surface at individual nanostructure are difficult to control or determine, limiting quantitative understanding of electrochemical data.

SECM operated in local feedback mode enables noncontact and spatially resolved electrochemical characterization of a single 1D nanostructure even using a micrometer-sized probe. Consider a SECM experiment in which a redox-active mediator is electrolyzed at a disk UME (process 1 in Figure 3-1) and is regenerated at a conductive 1D nanostructure, for instance, at a band-shaped conductor embedded in an insulating material (process 2). When the tip is far from the substrate, a steady-state limiting current is obtained. When the tip–substrate distance, d,

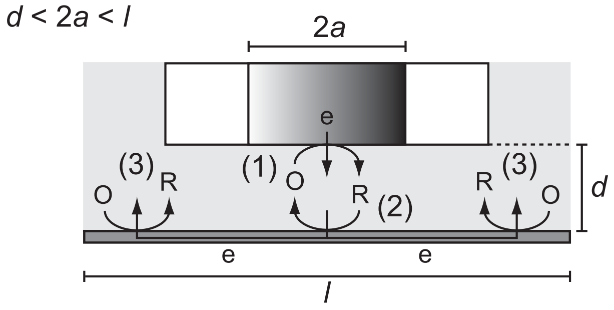

(i) positive feedback effect (2a < w)

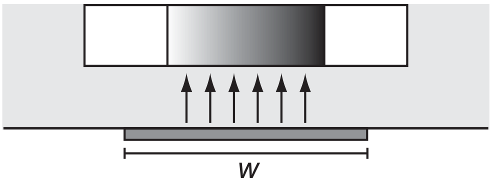

(ii) negative feedback effect (w = 0)

(iii) positive local-feedback effect ($d \leq w < 2a$)

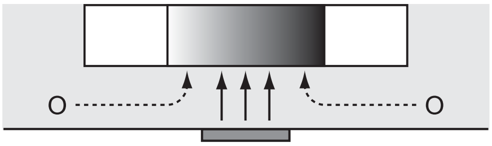

(iv) negative local-feedback effect ($w << d < 2a$)

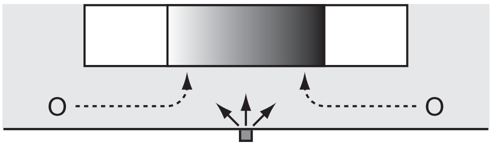

Figure 3-1. Scheme of a SECM feedback experiment with a disk UME above a band electrode. Only major diffusion modes in each feedback mode (i-iv) are shown; the solid arrows indicate planar or hemicylindrical diffusion of regenerated mediator molecules from the band surface to the tip, and the dotted arrows represent hindered diffusion of mediator molecules from the bulk solution to the tip.

becomes smaller than the disk diameter, 2*a*, a feedback effect of the mediator regeneration on the tip current is observed.[35] In this feedback experiment, the band length, *l*, is much larger than the disk diameter so that electron transport between the nanoband electrode and the bulk solution is mediated directly at the exterior electrode/solution interface (process 3), eliminating any need for a counter electrode connected externally to the nanoband electrode.[36] Therefore, when the band width, *w*, is larger than the disk diameter ($w > 2a$), an efficient redox cycling based on planar mediator diffusion in the gap amplifies the tip current as the gap becomes narrower (positive feedback effect).[35] Without a conductive band ($w = 0$), the tip current is suppressed by hindered mediator diffusion from the bulk solution to the tip, resulting in a decrease in the tip current against a decrease in the gap width (negative feedback effect).[35]

A local feedback effect is observed in the intermediate case, where the finite band width is smaller than the disk diameter ($w < 2a$). In this case, the gap under the tip is depleted of the mediator, because of the hindered diffusion above the insulating sheath of the nanoband. Mediator regeneration, however, still occurs locally on the narrow band surface to enhance the tip current. The local feedback effect can be positive or negative, depending on the diffusion mode of the regenerated mediator. A positive local feedback effect is observed when the band width is comparable to or larger than the gap width ($d \leq w < 2a$). In the relatively narrow gap, mass transport of the regenerated mediator molecules to the tip surface is spatially restricted to planar diffusion above the band surface, resulting in an increase in the tip current at a shorter tip–substrate distance, as observed with the standard positive feedback effect. When the band is much narrower than the gap and, subsequently, the tip diameter ($w << d < 2a$), the tip current is still enhanced by a negative local feedback effect. In the relatively wide gap, mass transport of the regenerated mediator molecules is based on hemicylindrical diffusion. Importantly, the mediator flux based on the hemicylindrical diffusion depends only on the logarithm of the band width and is proportional to the effective band length so that the effective length rather than the width mainly determines the total mediator flux.[37] The effective band length under the SECM probe is comparable to the disk diameter and is one-third of the perimeter of the disk edge so that the total mediator flux from the narrow band surface is significant in comparison with the total mediator flux at the tip in the bulk solution, which originates mainly from the mediator electrolysis at the disk edge; the so-called edge effect. Moreover, the regenerated mediator is detected with high collection efficiency at the tip surface, which is much larger than the effective band surface. Therefore, mediator flux from a conductive 1D nanostructure with micrometer length significantly enhances the current response of a micrometer-sized probe positioned at a micrometer tip–substrate distance.

Here we report on theoretical and experimental studies of SECM feedback effects with nanoband electrodes as a geometrical model for conductive 1D nanostructures. Although manually[38–40] and lithographically[41,42] fabricated nanoband electrodes have been extensively studied, there are only several SECM studies of band electrodes,[16,43–46] where no local feedback effect was considered. In this contribution, a SECM diffusion problem with a semi-infinitely long band electrode under a disk UME probe is numerically solved in three-dimensional coordinates to demonstrate that the feedback mechanism at a short tip–substrate distance changes from positive feedback mode, to positive local feedback mode, and then to negative local feedback mode as the finite band width decreases. An approximated equation for tip current enhancement in negative local feedback mode is derived to evaluate how the tip current is affected by the lateral size and geometry, and redox activity of 1D nanostructures. A manually fabricated Pt band electrode with 100 nm width and 2.6 cm length is studied using 2-, 10-, and

25-μm-diameter disk Pt UMEs in line scan, approach curve, and imaging experiments to demonstrate the positive and negative local feedback effects.

3.3 THEORY

3.3.1 Model

A SECM diffusion problem at a band substrate electrode was defined in Cartesian coordinates. Actual simulations were carried out in the whole domain for line scan experiments and in a quarter of it (Figure 3-2) for chronoamperometry and approach curve experiments. The origin of the coordinate axes was set at the center of a disk UME probe. A band electrode is faced in parallel to the probe surface such that the band center is just under the origin. The x and y coordinates are in directions that are parallel to the longer and shorter axes of the band electrode, respectively, while the z coordinate is vertical to the electrode surfaces. Both disk and band electrodes are surrounded by a thick insulating sheath (RG = r_g/a = 10, where r_g is the outer radius of the insulating layer). The band electrode is assumed to be semi-infinitely long and unbiased. These assumptions are equivalent to the conditions that (1) the potential of the band electrode is determined by the bulk solution composition such that the mediator regeneration on the substrate surface is diffusion-limited[36] and (2) the simulation results are independent of the band length. The first condition of diffusion limitation is defined as the corresponding boundary condition on the band surface. The second condition is satisfied with the finite band length of l = 19a, which is limited by the simulation space.

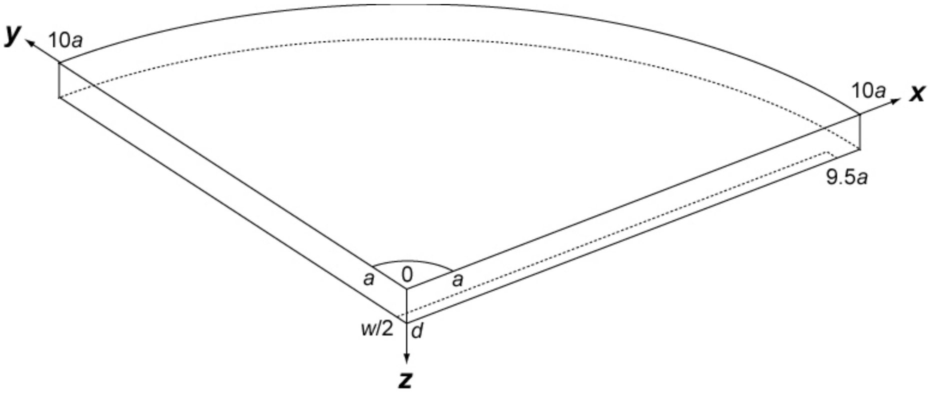

Figure 3-2. Geometry of SECM diffusion problems with a band electrode defined in Cartesian coordinates.

Initially, the solution phase contains only one redox-active mediator, O. Diffusion-limited electrolysis of the mediator at a disk SECM probe in the bulk solution, *i.e.*, O + *n*e → R, results in a steady-state limiting current, $i_{\mathrm{T},\infty}$, which is given by

$$i_{\mathrm{T},\infty} = 4nFDc_0a \qquad (1)$$

where F is faraday constant, D and c_0 are the diffusion coefficient and concentration of the redox mediator in the bulk solution. Mediator diffusion in the solution phase is defined by

$$\frac{\partial c}{\partial t} = D\left(\frac{\partial^2 c}{\partial x^2} + \frac{\partial^2 c}{\partial y^2} + \frac{\partial^2 c}{\partial z^2}\right) \qquad (2)$$

where c is the local concentration of the mediator, O, at (x, y, z). The diffusion coefficients of O and R are assumed to be the mean value so that mathematical treatment is restricted to the concentration of O. Effect of the electrical double layer at a nanoband electrode on the mediator transport is not considered here for simplicity.[47] The mediator, O, is regenerated from R on the band electrode surface at the diffusion-limited rate, where the boundary condition is

$$c = c_0 \qquad |x| \leq 9.5a,\ |y| \leq w/2, \text{ and } z = d \qquad (3)$$

The other boundary conditions are:

disk probe surface

$$c = 0 \qquad x^2 + y^2 \leq a^2, \text{ and } z = 0 \qquad (4)$$

insulation region around the disk electrode

$$\left[\frac{\partial c}{\partial z}\right]_{z=0} = 0 \qquad a^2 < x^2 + y^2 < 100a^2, \text{ and } z = 0 \qquad (5)$$

insulation region around the band electrode

$$\left[\frac{\partial c}{\partial z}\right]_{z=d} = 0 \qquad |x| > 9.5a \text{ or } |y| > w/2,\ x^2 + y^2 < 100a^2, \text{ and } z = d \tag{6}$$

simulation space limit

$$c = c_0 \qquad x^2 + y^2 = 100a^2, \text{ and } 0 \leq z \leq d \tag{7}$$

Equation 7 implies that the simulation space is limited to the gap between the tip and substrate so that the mediator concentration is equal to the bulk value beyond the limits. While this standard approximation was used in almost all published SECM simulations and leads to ~2 % error for RG = 10,[48] the same approximation was used here to check the validity of our simulation results by comparing them with the previous results. The currents at the disk and band electrodes, i_T and i_S, respectively, are given by integrating the flux over the electrode surfaces

$$i_\text{T} = 2\pi nFDc_0 \int_0^a x \left[\frac{\partial c}{\partial z}\right]_{y,z=0} dx \tag{8}$$

$$i_\text{S} = nFDc_0 \oint \left[\frac{\partial c}{\partial z}\right]_{z=0} dS \tag{9}$$

This 3D SECM diffusion problem was solved using the commercial program FEMLAB version 3.1i (COMSOL, Inc., Burlington, MA), which applies the finite element method. For SECM chronoamperometry, the time-dependent problem was solved at a fixed vertical distance between the centers of the disk and band electrodes. For approach curves, both tip and substrate currents were calculated at a variety of the center–center distances under the steady state by setting the left-hand side of eq 2 to zero. Steady-state tip current was calculated also for line scans, where the band electrode rather than the disk probe was moved laterally to the y-direction on the insulating surface. Computations were done on a personal computer equipped with a Pentium 4 3.0 GHz processor unit and 4.0 GB RAM with Windows XP Professional or a workstation equipped with a Xeon 3.0 GHz processor unit and 5.0 GB RAM with Linux.

3.3.2 Chronoamperometry

Numerical simulations were carried out for diffusion-limited chronoamperometric responses at a disk UME positioned at a fixed distance (d/a = 0.4 in Figure 3-3) from band electrodes with different widths. Although an infinitely-long band electrode in the bulk solution does not provide a true steady-state current at long times,[49] mediator diffusion in the SECM configuration is spatially restricted by the probe so that the tip and substrate currents reach steady state values.[50] Chronoamperometric tip currents calculated for large conductive and insulating substrates agree well, within a few percent errors, with those reported previously.[50] All simulated responses at a short time regime ($a/\sqrt{Dt} > 6$ at $d/a = 0.4$) agree with the response at a disk UME with RG = 10 in the bulk solution,[51] where the diffusion layer at the UME tip is too thin to interact with the substrates. In a longer time regime, each chronoamperometric response approaches to a different steady-state value. When the band width is larger than the tip diameter, the chronoamperometric response is similar to that at a conductive substrate. With a narrower band, the time needed for a steady state is longer and gives a smaller steady-state current. Importantly, the tip current with the narrowest band electrode that could be simulated using FEMLAB ($w/2a$ = 0.003) is much larger than that with an insulating substrate, enabling SECM-based detection of the band surface embedded in the insulating substrate.

The dependence of the tip current on the band width can be explained by collection efficiencies at the band and probe electrodes. When mediator molecules are electrolyzed at a disk UME positioned just above a band electrode, the product molecules diffuse to and react on the band surface to locally regenerate the mediator molecules. With a narrower band electrode, more product molecules can escape through the gap laterally to the y-direction so that less product

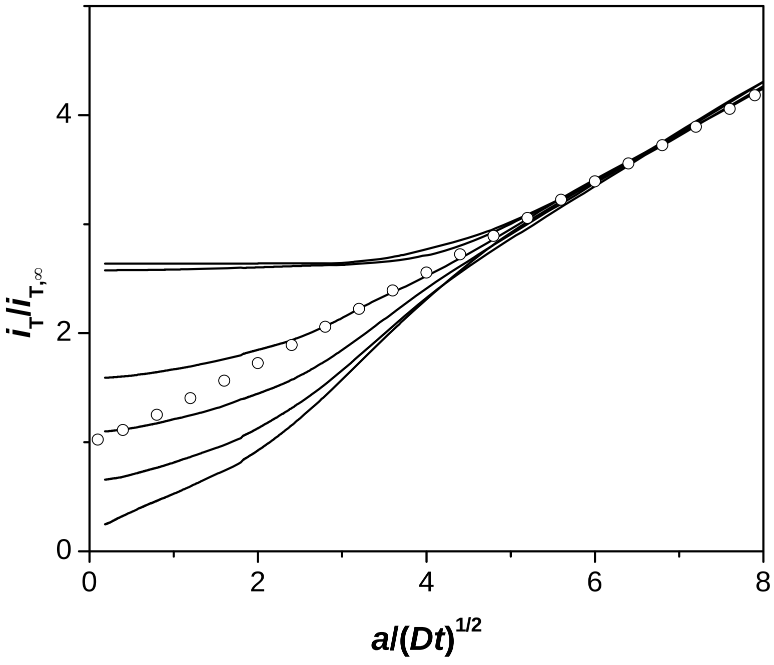

Figure 3-3. Simulated diffusion-limited chronoamperometric responses at a disk UME probe positioned above band substrate electrodes with different widths. The lines are for $w/2a$ = 10 (a conductive substrate), 1, 0.3, 0.1, 0.003, and 0 (an insulating substrate) from the top. The circles represent a chronoamperometric response at a disk UME with RG = 10 in the bulk solution.[51]

molecules react on the band surface. The lower collection efficiency at a narrower band electrode results in a smaller tip current. A narrow band electrode, however, regenerates a significant amount of mediator molecules, which is collected with high efficiency at the disk UME tip with the surface area that is much larger than that of the band electrode. Therefore, the tip current with a narrow band electrode is significantly larger than that with an insulating substrate.

3.3.3 Approach Curve

Diffusion-limited approach curves at the steady state were obtained with band substrates with different widths (Figure 3-4). The approach curves for conductive and insulating substrates ($w/2a$ = 10 and 0, respectively) agree with those reported previously.[52,53] The largest errors of a few percents were observed with an insulating substrate in the distance range of $d/a > 1$. The current response at a tip–substrate distance is smaller with a narrower band electrode, because of the lower collection efficiency. A feedback effect is observed within the tip−substrate distance that is comparable to the disk diameter, indicating that a nanoband substrate can be detected by positioning a disk UME at the tip−substrate distance of micrometers rather than nanometers. This result is in contrast to the case of a band-shaped SECM probe, where a feedback effect is observed within the distance that is several times of the band width.[46]

The shape of the approach curves strongly depends on the band width and the tip–substrate distance. Each characteristic approach-curve behavior corresponds to a different feedback effect. The approach curve with a band electrode with the width that is larger than the tip diameter ($2a < w$) overlaps with the approach curve with a conductive substrate (positive

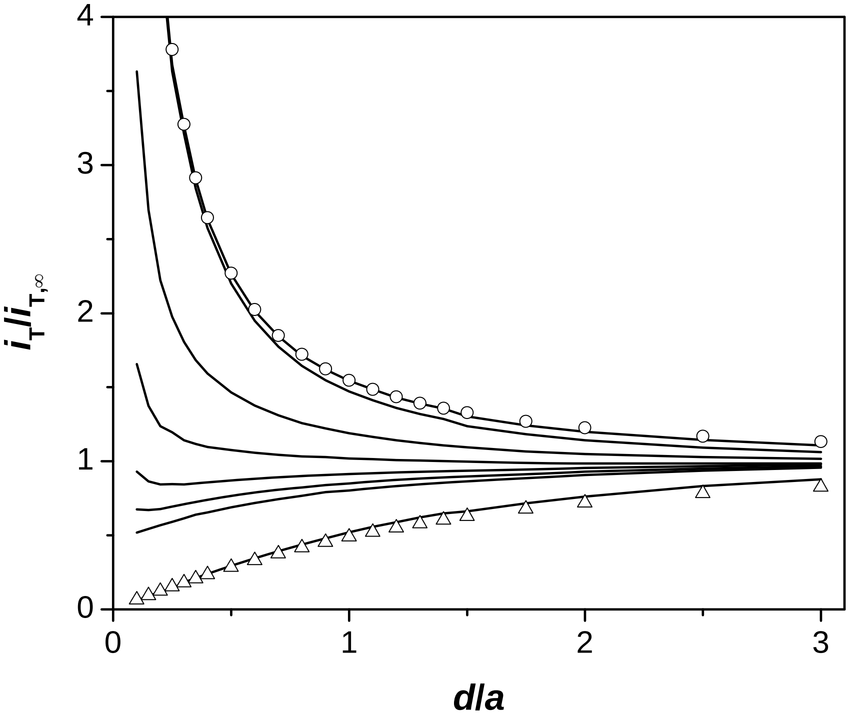

Figure 3-4. Simulated approach curves with a disk UME probe above band substrate electrodes with different widths. The solid lines are for $w/2a$ = 10 (a conductive substrate), 1, 0.3, 0.1, 0.03, 0.01, 0.003, and 0 (an insulating substrate). The circles and triangles represent theoretical approach curves with conductive and insulating substrates, respectively.

feedback effect). When the band width is smaller than the disk diameter and is comparable to or larger than the tip–substrate distance ($d \leq w < 2a$, *e.g.*, $w/2a = 0.3$ and 0.1 in Figure 3-4), the tip current increases as the tip–substrate distance decreases (positive local feedback effect), while the tip current is smaller than that with a positive feedback effect. With the band that is much narrower than the gap ($w << d$, *e.g.*, $w/2a = 0.003$ in Figure 3-4), the tip current decreases as the tip–substrate distance decreases (negative local feedback effect), where the tip current is larger than that with a negative feedback effect. With some narrow bands (*e.g.*, $w/2a = 0.03$ and 0.01 in Figure 3-4), both positive and negative local-feedback effects are observed in short and long distance ranges, respectively, resulting in a shallow minimum. Although such an approach curve with a shallow minimum is also known in the presence of a coupled homogeneous chemical reaction[54,55] and a lateral transport on the substrate surface,[56,57] the origin of this minimum with a band electrode is a transition between the two local-feedback mechanisms.

3.3.4 Positive and Negative Local-Feedback Mechanisms

Steady-state concentration profiles of mediator molecules in the gap were calculated to understand the local feedback mechanisms (Figure 3-5). In both positive and negative local-feedback modes, the gap under the tip is depleted of the mediator, because of the hindered mediator diffusion. The local diffusion mode of the regenerated mediator molecules, however, depends on the band width relative to the tip–substrate distance, resulting in the different local-feedback mechanisms.

A positive local-feedback effect is observed, when the gap width is comparable to or smaller than the band width. In the narrow gap, the local diffusion of regenerated mediator is spatially restricted to planar diffusion above the band surface at the steady state (Figure 3-5). As

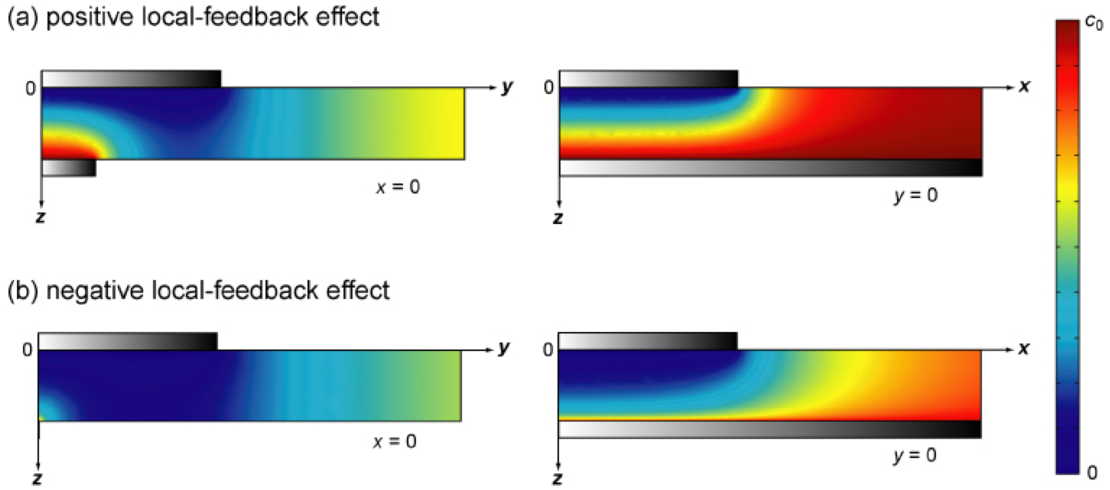

Figure 3-5. Simulated concentration profiles of the redox mediator in the gap between the tip and the band electrode with the width of (a) 0.3*a* and (b) 0.003*a*. The left and right graphs show the cross sections of the concentration profiles at $x = 0$ and $y = 0$, respectively. The tip–substrate distance is 0.4*a*.

the tip–substrate distance decreases, the planar diffusion layer becomes thinner, which increases the mediator flux from the band surface to the tip, enhancing the tip current. The tip current enhancement is smaller than that with a conductive substrate, because the mediator regeneration is localized on the band surface. It should be noted that the positive local-feedback mechanism is apparently consistent with current amplification in a line scan experiment conducted by Heinze and co-workers,[43] where the normalized tip current at a 25 μm-diameter disk probe increased to 1.3 above a 500 nm-wide Ag band electrode ($w/2a = 0.02$) at the tip−substrate distance of 1–2 μm ($d/a = 0.08$–0.16). The experimental tip current, however, is larger than the theoretical one expected with the reported band width even at a shorter tip−substrate distance, suggesting that the effective band width is larger than the reported value. Moreover, the tip current based on a positive local feedback effect is sensitive to the band width so that approach curve experiments allows more reliable determination of the band width than line scan experiments, because the tip–substrate distance can be also determined from an approach curve.

A negative local-feedback effect is observed, when the gap width is much larger than the band width. In the wide gap, the local mediator diffusion from the band surface becomes hemi-cylindrical at the steady state (Figure 3-5b). A change in the tip–substrate distance does not strongly affect the concentration profile of the regenerated mediator, which depends on the logarithm of the distance from the band surface.[58] Therefore, a total flux of the regenerated mediator to the tip in the negative local-feedback mode increases only slightly at a shorter tip–substrate distance. The approach curve appears to be a negative one, because the hindered mediator diffusion significantly contributes to the tip current, while the tip current is larger than that with an insulating substrate.

3.3.5 How Narrow Band Can Be Detected?

In the negative local-feedback mode, the tip current enhancement corresponds to the current based on mediator regeneration on the band surface. Since the numerical simulations are limited to the minimum normalized band width of 0.003, an analytical equation for the substrate current, i_S, was obtained approximately to evaluate the minimum band width that is detectable in the negative local-feedback mode. In the wide gap, the local mediator diffusion from the band surface is hemi-cylindrical at the steady state (Figure 3-5b). Therefore, the substrate current approximates to the long-time diffusion-limited chronoamperometric current at the band electrode in the bulk solution[59]

$$i_S = \frac{2\pi nFDc_0 l_{\mathrm{eff}}}{\ln(4Dt\alpha / w^2)} \tag{10}$$

where t is time after the potential step, = 5.02 at $Dt/w^2 > 10$, and l_{eff} is the effective length of the band surface for the mediator regeneration. In contrast to the time-dependent current in the bulk solution, spatially-restricted mediator diffusion in the SECM configuration results in a steady-state current, where thickness of the hemi-cylindrical diffusion layer at the band electrode is limited by the gap width, *i.e.*, $\sqrt{2Dt} \sim d$. At a short tip–substrate distance, an effective band length is approximated to the disk diameter, *i.e.*, $l_{\mathrm{eff}} \sim 2a$. With these approximations, combination of eq 10 with eq 1 gives the normalized substrate current, $i_S/i_{T,\infty}$ as

$$\frac{i_S}{i_{T,\infty}} = \frac{\pi}{\ln(2\alpha d^2 / w^2)} \tag{11}$$

The normalized substrate current based on eq 11 agrees with the simulated one within 5 % error for the two narrowest band electrodes ($w/2a$ = 0.01 and 0.003) in the distance range of d/a = 0.25–2 (data not shown).

A narrow band electrode on the insulating substrate can be detected, when the tip current with the band electrode is significantly larger than that with the insulating surface. The difference in the normalized tip currents approximates to the normalized substrate current given by eq 11. In standard SECM experiments, a 10 % change in the normalized tip current can be easily measured. Since the tip–substrate distance is smaller than the tip diameter in a feedback experiment, the band surface can be detected when $i_S/i_{T,\infty} > 0.1$ at $2a > d$. With these conditions, eq 11 gives

$$\frac{w}{2a} > \sqrt{\frac{2\alpha}{\exp(10\pi)}} = 4.8 \times 10^{-7} \tag{12}$$

The diameter of a disk SECM probe must be smaller than 25–50 μm for steady-state experiments without a convection effect so that eq 12 predicts that conductive bands with the width of 0.12–0.24 Å or larger can be detected. This result predicts that a negative local-feedback effect is not practically limited by the band width.

3.3.6 Effects of Lateral Geometry and Electron Transfer Rate at 1D Nanostructure

The tip current enhancement in the negative local-feedback mode corresponds to the substrate current so that the approximated substrate current based on eq 11 was further analyzed to address how the tip current is affected by the lateral geometry and electron transfer rate at a 1D nanostructure. In eq 11, the logarithmic dependence of the substrate current on the band width indicates that effect of the lateral geometry on the feedback response is not large but significant. For instance, a hemi-cylindrical electrode is a better geometrical model for a nanotube, where the long-time diffusion-limited current at a band electrode is equal to that of a hemi-cylindrical electrode with the radius, r, that is a quarter of the band width.[58] Also, Compton and co-workers demonstrated that chronoamperometric responses at elevated and recessed band electrodes are larger and smaller, respectively, than the response at the corresponding inlaid band electrode.[60] The height and depth of the band surface that affects the current responses is determined by the band width, which is much smaller than the probe size in the negative local-feedback mode. Therefore, the negative local-feedback effect is sensitive to the change in the local topography at the nanoband electrode that is much smaller than the tip size and the tip−substrate distance, because the substrate current depends on the topography.

The substrate current is controlled by mass transfer and electron transfer rates at the band electrode. The diffusional mass transfer is faster at a narrower band, where the tip current is more amenable to the finite electron transfer rate. With an approximation that the band surface is uniformly accessible in negative local-feedback mode, the apparent mass transfer coefficient at the band surface in negative local-feedback mode, m_{NLF}, is given using eq 10 with $\sqrt{2Dt} \sim d$ and $l_{\mathrm{eff}} \sim 2a$ as

$$m_{\mathrm{NLF}} = \frac{i_{\mathrm{S}}}{nFc_0 w l_{\mathrm{eff}}} = \frac{2\pi D}{w \ln(2\alpha d^2 / w^2)} \qquad (13)$$

The mass-transfer coefficients of a redox molecule with a typical diffusion coefficient of 7.5×10^{-6} cm^2/s were calculated for 1, 10, and 100 nm-wide band electrodes with a 25 μm-diameter probe at the tip–substrate distance of $0.3a$ and a (Table 3-1). The mass transfer rate in negative local-feedback mode is only slightly enhanced at a shorter distance, which is in contrast to the case of positive feedback mode (see below). The mass transfer coefficient at a 10 nm-wide band electrode is still comparable to the largest reliable standard rate constants reported in

Table 3-1. A comparison of mass transfer coefficients at nanoband electrodes in negative local-feedback and positive feedback modes.[a]

	m_{NLF}[b]		m_{PF}[c]	
	0.3a[d]	a[d]	0.3a[d]	a[d]
w / nm				
100	0.492	0.394	6.31	3.01
10	3.33	2.84	63.1	30.1
1	25.1	22.3	631	301

[a] Calculated for a redox mediator with the diffusion coefficient of 7.5 × 10^{-6} cm^2/s. [b] Calculated using eq 13 with a = 25 μm. [c] Calculated using eq 14 with a = w/2. [d] The tip–substrate distance.

literature (~5 cm/s).[3] Therefore, a negative local-feedback effect is not seriously limited by the finite electron transfer rate even with a very narrow 1D nanostructure.

3.3.7 Limitations of Positive Feedback Mode in 1D Nanostructure Detection

Although positive feedback mode has been a main operation mode for conductive substrates,[35] its application for conductive 1D nanostructures is limited by the available probe size and finite electron transfer rate, which are not serious limitations in negative local-feedback mode. Positive feedback mode requires a disk probe with the diameter that is smaller than the band width ($w > 2a$). The radius of the smallest disk SECM probe that was shown to give a reliable positive feedback effect is 300–400 nm.[61–63] Therefore, the smallest probes are still too large to observe a positive feedback effect with most 1D nanostructures, which have the width of 1–100 nm. A positive local-feedback effect is observable with relatively wide 1D nanostructures using the smallest probes, where the tip–substrate distance is comparable to or smaller than the band width. Since the closest tip–substrate distance is usually larger than 10 % of the tip radius, the detectable band width with the smallest probe is 30–40 nm or larger ($w \geq d > 0.1a$).

When a smaller disk electrode is used as a SECM probe, a positive feedback effect with such a small probe is limited by the finite electron transfer rate at the substrate surface. In positive feedback mode, the effective mass transfer coefficient at the local area of the conductive substrate under the tip, m_{PF}, is determined by the probe size and the tip–substrate distance as[64]

$$m_{\mathrm{PF}} = \frac{4D[0.68 + 0.78377a/d + 0.3315\exp(-1.0672a/d)]}{\pi a} \qquad (14)$$

Equation 14 was used to calculate the mass transfer coefficients with 1, 10, and 100 nm-wide bands at the tip–substrate distances of $0.3a$ and a, where the probe diameter was assumed to be equal to the band width (Table 3-1). The mass transfer is enhanced at a short tip–substrate distance in positive feedback mode. The mass transfer coefficients at a 100 nm-wide band electrode are already larger than the largest reliable standard rate constants (~5 cm /s).[3] Indeed, such a large rate constant was determined using a 2 μm-diameter probe in positive feedback mode.[65] The mass transfer at narrower bands is even faster, resulting in a kinetically limited tip current.

3.3.8 Line Scan

Diffusion-limited steady-state tip current in line scan experiments was obtained numerically. In this simulation, the probe position was fixed at a constant height from the substrate surface, while the band electrode was rastered laterally to the y-direction. In previous 3D simulations of line scans over band electrodes, only a relatively thick band with $w = 0.5a$ was considered.[45] Figure 3-6 shows simulated line scans with different band widths and tip−substrate distances. A narrow conductive band embedded in an insulating substrate can be easily detected in a line scan as an enhancement of the tip current. A current peak was observed when the tip center is positioned above the band center. The contrast, which is defined as the difference in the tip currents above the band center and the insulating surface, is enhanced with a wider band and at a shorter tip–substrate distance. While the spatial resolution that is represented by the width of the current peak can be improved with a smaller probe and at a shorter tip–substrate distance, the half peak width is in the range of $2a$–$3a$ in all simulated line scans. This result indicates that two nanostructures with the separation of more than $1a$–$1.5a$ are resolvable in a line scan.

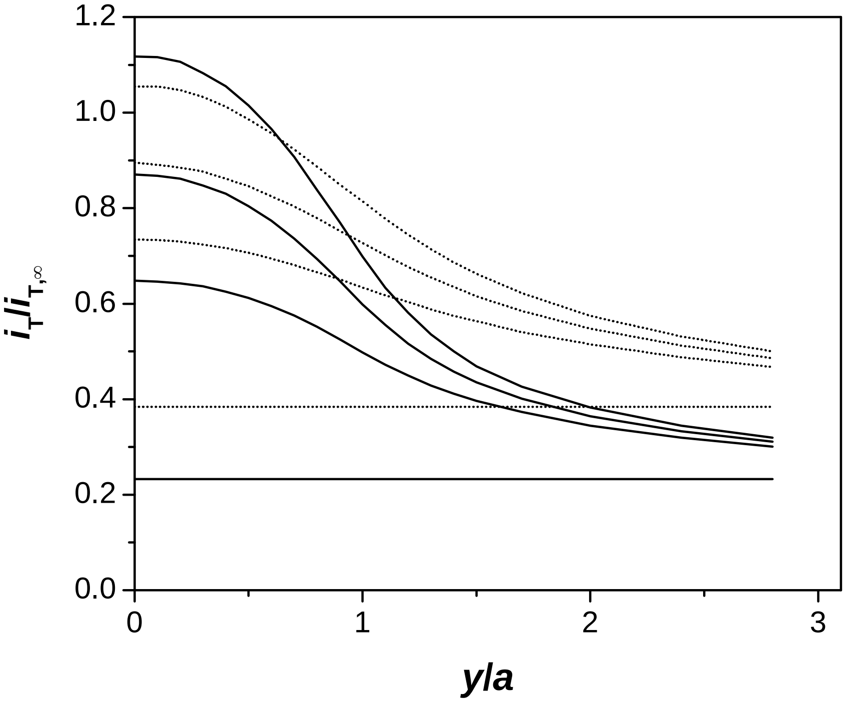

Figure 3-6. Simulated line scans over band substrate electrodes with different widths. The solid and dotted lines were obtained at d/a = 0.4 and 0.7, respectively. At each distance, the band widths are given by $w/2a$ = 0.1, 0.03, 0.003, and 0 (an insulating substrate) from the top.

3.4 EXPERIMENTAL SECTION

3.4.1 Chemicals

$Ru(NH_3)_6Cl_3$ (Strem Chemicals, Newburyport, MA) and ascorbic acid (Fisher Chemical, Fair Lawn, NJ) were used as redox-active molecules. 5 mM $Ru(NH_3)_6Cl_3$, 2 mM ascorbic acid, or both in 0.1 M KCl was used for all SECM experiments. All reagents were used as received. All aqueous solutions were prepared with 18.3 $M\Omega\cdot cm^{-1}$ deionized water (Nanopure, Barnstead, Dubuque, IA).

3.4.2 Electrode Fabrication and Electrochemical Measurement.

Pt nanoband electrodes were fabricated as reported by others.[49] A 5 nm-thick Cr adhesion layer and then a 100 nm-thick Pt film were deposited on a 2.5 cm × 2.5 cm glass substrate by sputtering (2400 6J Sputtering System, Perkin Elmer, Wellesley, MA). The Pt film thickness was determined by profilometer (Alpha Step 200, Tencor, San Jose, CA) to be 95–110 nm. A 1.5 cm × 2.5 cm glass slide was used to sandwich the Pt layer using Epon epoxy (EPON resin 828 and EPI-CURE 3140 Curing Agent, Miller-Stephenson Chemical, Danbury, CT) as sealant, leaving ca. 1 cm × 2.5 cm of the Pt surface uncovered at one end for an electrical contact. The "sandwich" was placed on a Teflon sheet in an oven at 65°C overnight to cure the epoxy. A Cu wire was attached to the exposed Pt film by Ag epoxy (H20E, Epoxy Technology, Billerica, MA). The connections and adjoining edges of the "sandwich" were sealed with Epon epoxy (except for the top edge that is at the opposite side of the contact) for good insulation. The top edge of the band electrode was polished successively with 400 and 600 grit sandpapers

(Buehler, Lake Bluff, IL). Then, the electrode was polished with suspension of 1μm-sized cerium oxide (Buehler) in water. After the polishing process, the nanoband electrode was sonicated in water for 15 minutes. The relatively long sonication time was necessary to remove the remaining Pt materials from the insulating surface, which cause a broad current peak in SECM line scan experiments. Cyclic voltammograms with the nanoband electrodes demonstrated that the redox reaction of $Ru(NH_3)_6^{3+}$ mediator is diffusion-limited and that the effective band length was 2.6 cm, which agrees with the physical length (see Supporting Information).

A 25-μm-diameter Pt disk probe (RG = r_g/a = 10) and a 10 μm-diameter Pt disk probe (RG = 10) were fabricated as described previously.[66] Two μm-diameter Pt disk probes (RG = 10) were obtained from CH Instruments (Austin, TX). The tip radius and RG value were checked by optical microscopy and also determined from approach curves[52,67] measured using a home-built SECM setup.[68] A two-electrode setup was employed with a 1 mm-diameter AgCl-coated Ag wire serving as a reference/counter electrode and a Pt disk electrode as a SECM probe. The nanoband electrode was unbiased. The electrochemical cell was mounted on an adjustable platform, where any substrate tilt was compensated so that the tip current in the line scans over the glass surface that is adjacent to the nanoband electrode becomes as constant as possible. Most SECM experiments were carried out using a commercial instrument with close-loop piezoelectric motors (CHI 910B, CH Instruments), while the approach curves with 25 and 1.8 μm-diameter probes were measured using CHI 900 (CH Instruments). The SECM instruments were placed on a vibration isolation platform (model 63-533, TMC, Peabody, MA).

3.5 RESULTS AND DISCUSSION

3.5.1 Demonstration of Negative Local Feedback Effect

SECM line scan and approach curve experiments were carried out with an unbiased Pt nanoband electrode (100 nm in width and 2.6 cm in length) using a 25 μm-diameter disk Pt probe to demonstrate a negative local feedback effect for the first time. Besides $Ru(NH_3)_6^{3+}$ as a reversible redox mediator, ascorbic acid was used as an irreversible redox molecule to determine the tip–substrate distance in a line scan. Since two-electron oxidation of ascorbic acid is followed by fast irreversible chemical reactions,[69] no reduction occurs on a conductive substrate, resulting in a negative feedback effect both at conductive and insulating substrates with the 25-μm-diameter probe (see Supporting Information).

When $Ru(NH_3)_6^{3+}$ was used as a redox mediator, a peak-shaped current response was observed in a line scan over the nanoband electrode (Figure 3-7a). The normalized peak current is smaller than 1, indicating a negative local-feedback effect. The current peak is not perfectly symmetric, because of the surface roughness confirmed in a line scan experiment with ascorbic acid. The larger tip current at the left-hand (epoxy) side of the nanoband electrode corresponds to a recessed surface. A flatter surface could not be obtained over the long scan distance needed for a micrometer-sized probe. The smooth line scan with ascorbic acid eliminates the possibility that the current peak observed with $Ru(NH_3)_6^{3+}$ is based on a negative feedback effect from a cavity on the insulating surface. With $w/2a = 0.004$, the diffusion-limited peak current with $Ru(NH_3)_6^{3+}$ corresponds to the normalized tip–substrate distance, d/a, of 0.40, which agrees with the distance estimated from the tip current with ascorbic acid at the same tip position. The change in the tip–substrate distance due to the surface roughness is so small (±0.02 in normalized distance) that the

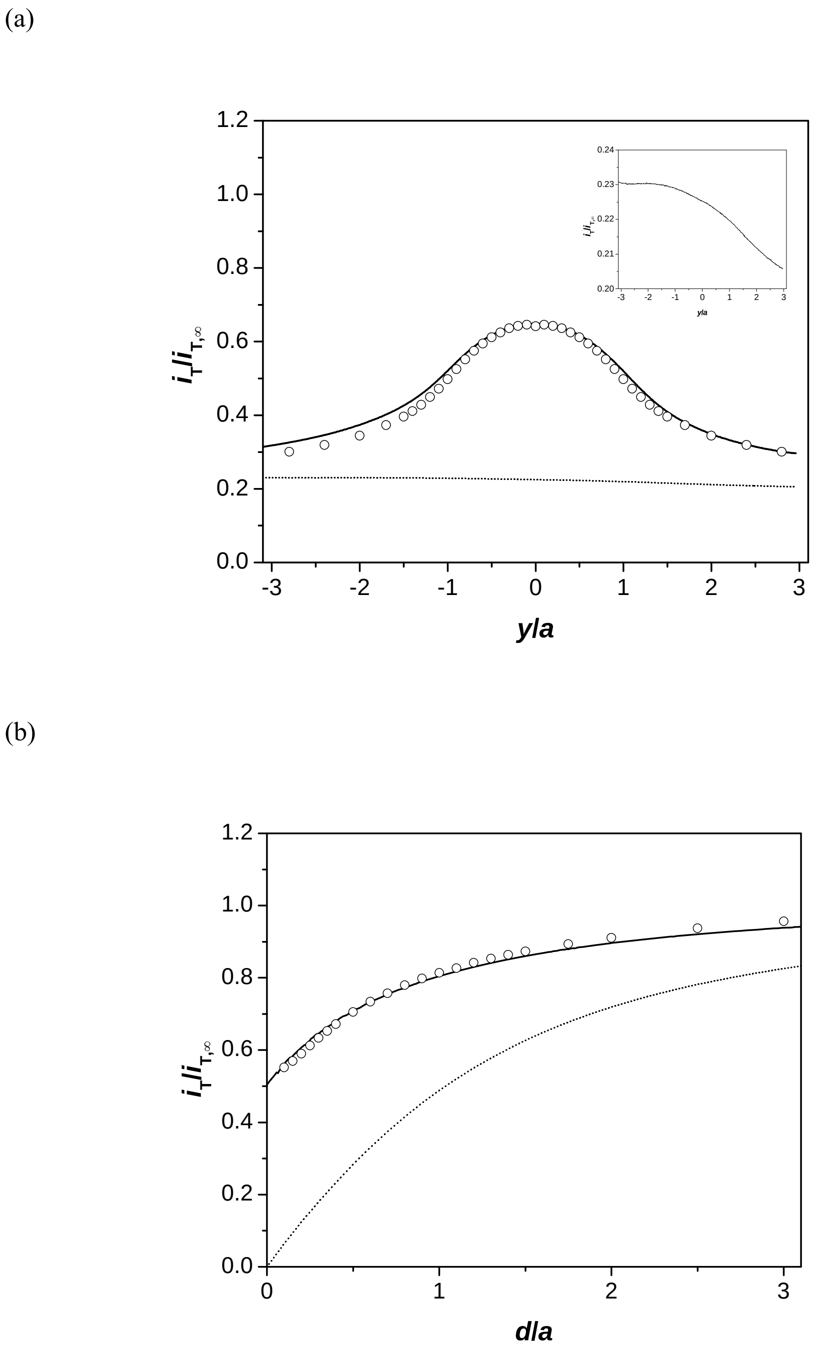

Figure 3-7. (a) Line scans over a 100 nm-wide and 2.6 cm-long Pt band electrode obtained using a 25 µm-diameter Pt disk probe with $Ru(NH_3)_6^{3+}$ (solid line) and ascorbic acid (dotted line) as a redox-active molecule in their mixed solution. The circles represent simulation results with *w*/2*a* = 0.004 at *d*/*a* = 0.40. The line scan with ascorbic acid is shown also in the inset. (b) An approach curve at the band electrode obtained using the 25 µm-diameter Pt disk probe with $Ru(NH_3)_6^{3+}$ (solid line). The circles represent simulation results with *w*/2*a* = 0.004. The dashed line is a theoretical approach curve with an insulating surface. The tip potential was set at −0.4 and 0.6 V for $Ru(NH_3)_6^{3+}$ and ascorbic acid, respectively, and the probe scan rate was 1.5 µm/s in both (a) and (b). The band electrode was unbiased.

line scan with $Ru(NH_3)_6^{3+}$ agrees with the theoretical one with $w/2a = 0.004$ at $d/a = 0.4$. The normalized band width corresponds to $w = 100$ nm, which is in the range of the Pt film thickness (95–110 nm) determined by profilimeter.

To further confirm the negative local-feedback effect, approach curves were measured with $Ru(NH_3)_6^{3+}$ at the tip position that gave a current peak in a line scan experiment (Figure 3-7b). As the tip is brought closer to the nanoband surface, the tip current decreases but does not approach to zero even at a very short tip–substrate distance, indicating tip current enhancement based on a negative local-feedback effect. The approach curve fits with simulation results also with $w/2a = 0.004$. The good fit confirms that the mediator regeneration on the band surface is diffusion limited. The band length is much larger than the probe diameter so that the potential of the unbiased band electrode should be sufficiently more positive than the standard potential of the $Ru(NH_3)_6^{3+/2+}$ couple, resulting in diffusion-limited mediator regeneration on the band surface.[36]

3.5.2 Positive and Negative Local Feedback Effects

The nanoband electrode was studied also using a 10-μm-diameter Pt disk probe to demonstrate both positive and negative local-feedback effects. The location of the nanoband electrode was determined in a line scan experiment with $Ru(NH_3)_6^{3+}$ as a mediator (Figure 3-8a). The peak-shaped response fits well with simulation results with $w/2a = 0.01$ at $d/a = 0.50$. The normalized band width corresponds to $w = 100$ nm. An approach curve with the 10 μm-diameter probe demonstrates that the feedback mechanism changes from negative local-feedback mode to positive local-feedback mode as the tip substrate distance decreases (Figure 3-8b). The decrease

(a)

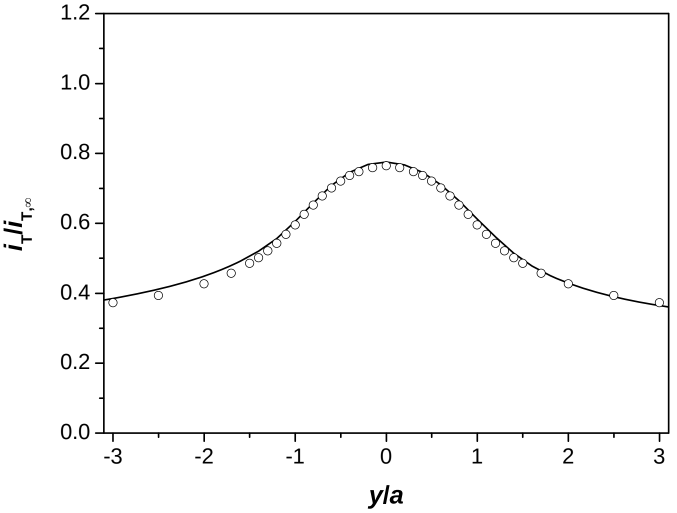

(b)

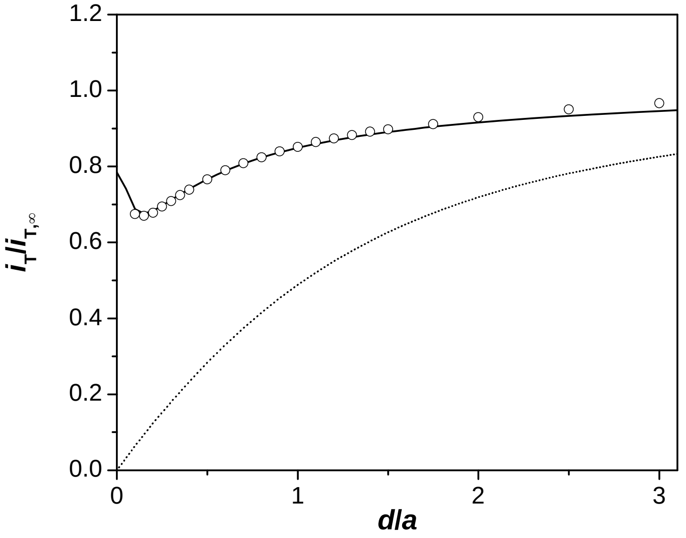

Figure 3-8. (a) A line scan over a 100 nm-wide and 2.6 cm-long Pt band electrode obtained using a 10 µm-diameter Pt disk probe with $Ru(NH_3)_6^{3+}$ as a redox mediator (solid line). The circles represent simulation results with $w/2a$ = 0.01 at d/a = 0.50. (b) An approach curve at the band electrode with $Ru(NH_3)_6^{3+}$. The circles represent simulation results with $w/2a$ = 0.01. The dashed line is a theoretical approach curve with an insulating surface. The tip potential was −0.4 V and the probe scan rate was 3.74 µm/s in both (a) and (b). The band electrode was unbiased.

in the tip current at $d/a > 0.2$ is due to a negative local-feedback effect. The tip current increases at a shorter distance region, which agrees with a positive local-feedback effect. The experimental curve fits with simulated results also with $w/2a = 0.01$. This approach curve is the first example with a shallow minimum based on a transition between positive and negative local-feedback modes. It should also be noted that, while previous SECM line scan experiments were carried out over a band electrode with such a width that should have given a positive local-feedback effect,[16,43] no approach curve was reported in the previous studies. The approach curve obtained using the 10 μm-diameter probe is the first clear demonstration of distance-dependent current amplification based on a positive local feedback effect.

Approach curves at the nanoband electrode were also measured using ~2-μm-diameter Pt disk probes (Figure 3-9). The tip current in the approach curves is comparable to $i_{T,\infty}$ even at a short tip–substrate distance, where a decrease in the tip current due to hindered diffusion is balanced by an increase in the tip current due to mediator regeneration on the band surface. An approach curve obtained with a 1.8-μm-diameter tip shows a slight positive local-feedback effect at $d/a < 0.3$ and fits with simulation results with $w/2a = 0.05$, yielding a band width of 90 nm. Most approach curves, however, fit with a theoretical one with $w/2a = 0.03$, which corresponds to the band with of 66 and 54 nm with $a = 1.1$ and 0.9 μm, respectively. The band widths are smaller than the Pt film thickness (95–110 nm). While an approach curve with a 2-μm-diameter probe is more sensitive to the band width than that with 10- and 25-μm-diameter probes, the apparently smaller feedback effect does not necessarily mean a physically narrower band surface. As discussed in the Theory Section, the feedback effect depends on mass transfer and electron transfer rates at the band electrodes. The smaller feedback effect is not likely due to electron transfer kinetics on the band surface, because the band length is much larger than the

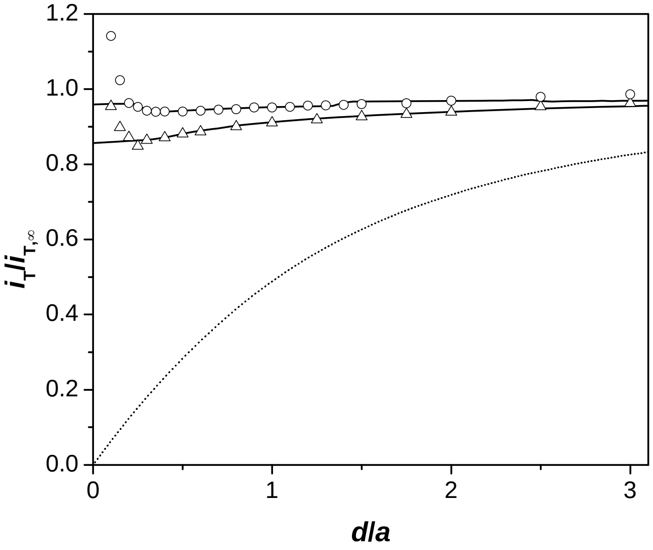

Figure 3-9. Approach curves with a 100 nm-wide and 2.6 cm-long Pt band electrode obtained using 1.8 and 2.2 μm-diameter Pt disk probes (upper and lower solid lines, respectively) with $Ru(NH_3)_6^{3+}$ as a redox mediator. The tip potential was set at −0.4 V and the probe scan rate was 1.1 μm/s. The band electrode was unbiased. The circles and triangles represent simulation results with $w/2a$ = 0.05 and 0.03, respectively. The dashed line is a theoretical approach curve with an insulating surface.

probe diameter.[36] It is more likely that mediator regeneration is suppressed on the band surface recessed from the surrounding insulating surface, which decreases the mass transfer rate.[60] The topographic information was not obtained reliably using ascorbic acid, where the tip current at a 2 µm-diameter probe decayed gradually during a line scan.

3.5.3 SECM Imaging of Local Electrochemical Activity at Nanoband Electrode

In addition to non-contact characterization, SECM enables spatially-resolved characterization of a single 1D nanostructure, which can not be done only using standard electrochemical approaches with an electrode based on the nanomaterial. To clearly demonstrate the advantage, a nanoband electrode was imaged using a 2 µm-diameter disk Pt probe (Figure 3-10a). The apparent band width in the image corresponds to the probe diameter, which determines the spatial resolution. The line scan at $x = 1.2$ µm fits with simulation results with $w/2a = 0.03$ at $d/a = 0.73$, where the tip–substrate distance was determined from the peak current using the simulated approach curve with the normalized band width. The image corresponding to the band surface becomes apparently narrower at the bottom of the image, which is due to a closer tip–substrate distance caused by the slightly tilted substrate. The tip current in the line scan at $x = 6.4$ µm is smaller than that at $x = 1.2$ µm (Figure 3-10b), confirming the shorter distance near the bottom of the image.

SECM imaging with a 2 µm-diameter probe also demonstrated a defect site on the nanoband electrode (Figure 3-11a), where the defect size is smaller than 10 and 25 µm-diameter probes. The normalized peak current of 0.73 at $x = -1.9$ µm (dotted line in Figure 3-11b) is smaller than the minimum normalized current of 0.85 calculated for a band electrode with $w/2a =$

(a)

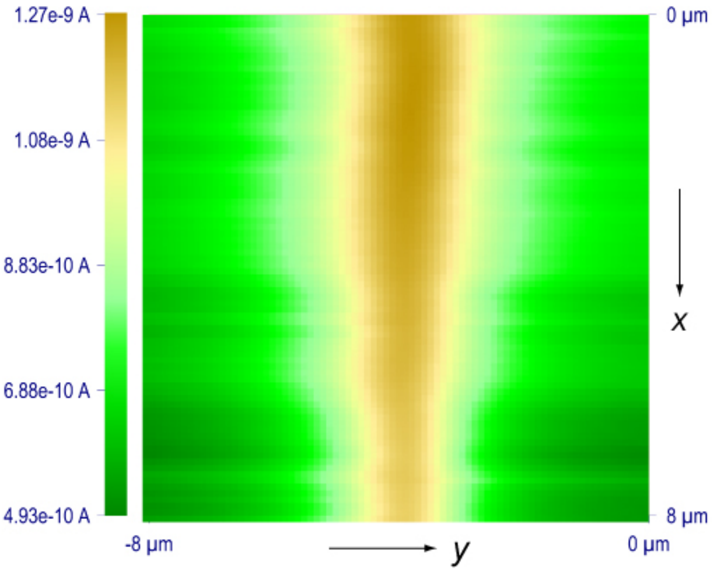

(b)

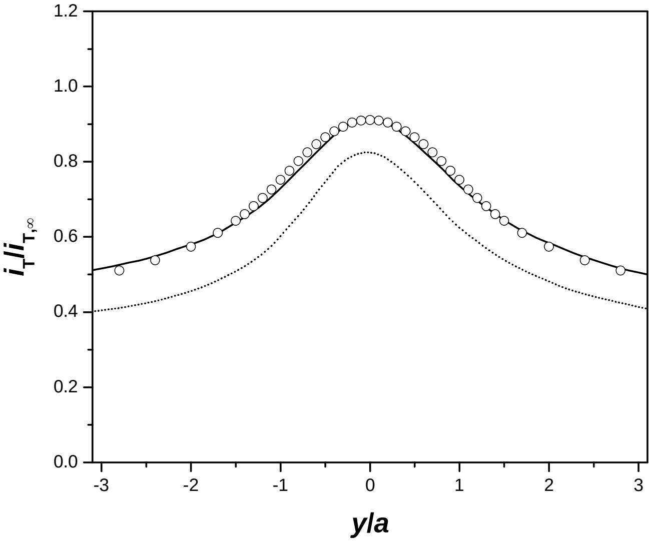

Figure 3-10. (a) An 8 µm × 8 µm image of a 100 nm-wide and 2.6 cm-long Pt band electrode obtained using a 1.8 µm-diameter probe with $Ru(NH_3)_6^{3+}$ as a redox mediator. The tip potential was −0.4 V and the probe scan rate was 1.1 µm/s. The band electrode was unbiased. (b) SECM line scans at x = 1.2 and 6.4 µm in the image (solid and dotted lines, respectively). The circles represent simulation results with $w/2a = 0.03$ at $d/a = 0.73$.

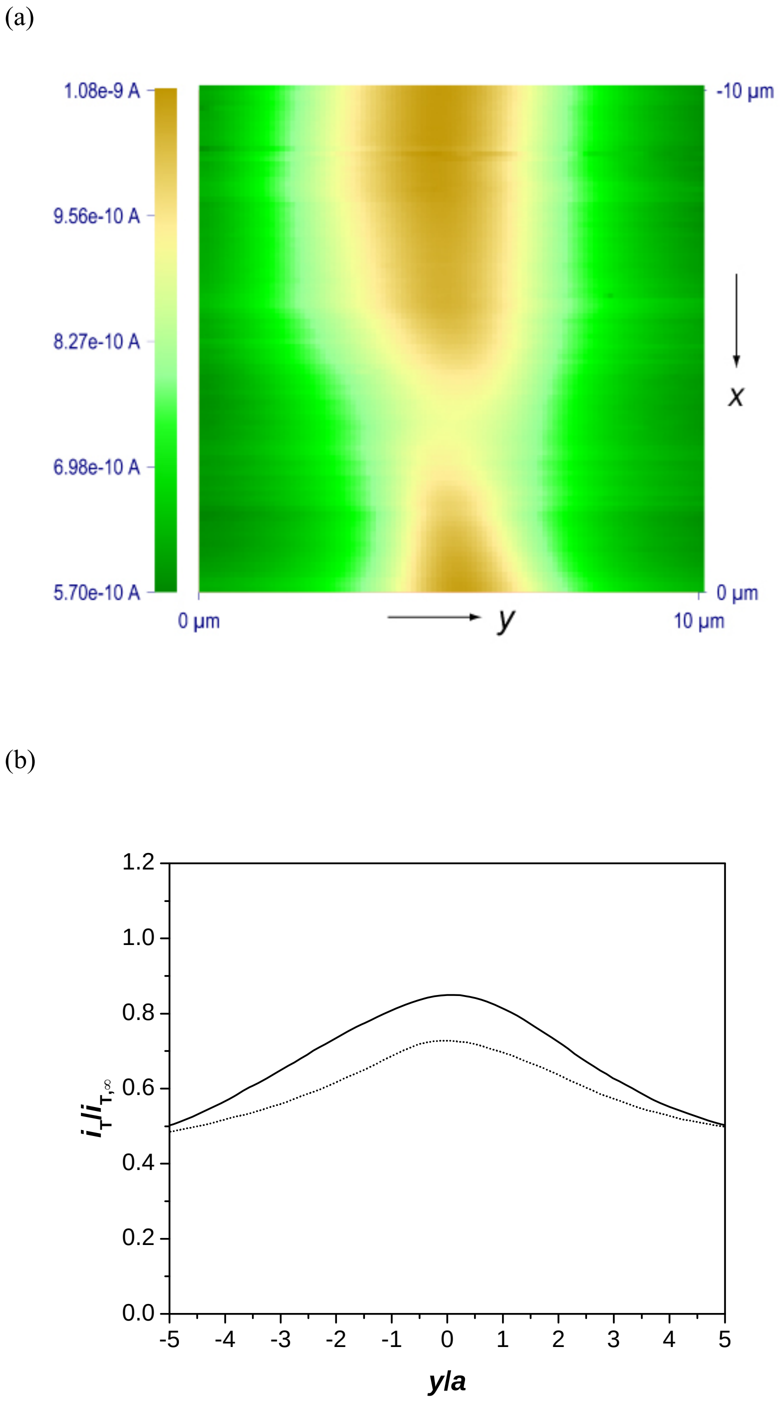

Figure 3-11. (a) A 10 µm × 10 µm image of a defect site on a 100 nm-wide and 2.6 cm-long Pt band electrode obtained using a 1.8 µm-diameter probe with $Ru(NH_3)_6^{3+}$ as a redox mediator. The tip potential was −0.4 V and the probe scan rate was 1.1 µm/s. The band electrode was unbiased. (b) SECM line scans at $x = -7.2$ and -1.9 µm in the image (solid and dotted lines, respectively).

0.03 at $d/a = 0.25$ (see triangles in Figure 3-9). Also, the normalized half-peak width of 4.3 at the defect site is larger than the theoretical range of 2–3 (see Line Scan in theory section), while the peak broadening is consistently observed in this image. The half peak width is also 4.3 at $x = -7.2$ µm, where the normalized peak current is 0.85 (solid line in Figure 3-11b). A possible origin of the broad peak is a gap between the nanoband and the insulating layer,[70,71] which can be a source of the mediator molecules. It, however, is more likely that the peak broadening is due to Pt nanochannels formed on the insulating surface during electrode polishing. When a nanoband electrode is polished, the channels are formed on the insulating surface and filled with the removed Pt materials. A significant negative local feedback effect is expected from the channels if they are connected to the main band or are longer than the probe diameter. Without long-time sonication of the nanoband electrodes (~15 minutes), a broad current peak was observed in line scans even using 10- and 25-µm-diameter probes.

3.6 CONCLUSIONS

Since the first introduction in 1989,[7] all SECM studies have been concerned about "two-dimensional" substrates with a surface area that is comparable to or larger than that of the probe. It was demonstrated that a disk-shaped conductive spot is detectable using SECM when the diameter of the target is at least 10–20 % of the disk probe diameter,[72] while such a small substrate must be externally biased for observing a feedback effect at the steady state. Here we demonstrated for the first time that an amperometric response of a micrometer-sized SECM probe can be significantly enhanced by a local feedback effect with an unbiased nanoband electrode as a geometrical model for a 1D nanostructure, where a lateral dimension normalized against the probe diameter, $w/2a$, can be as small as 4.8×10^{-7} in negative local-feedback mode. This result suggests that electron transfer reactions even at a single-walled carbon nanotube with a few nm diameter and micrometer length can be studied using a micrometer-sized SECM probe. SECM studies of carbon nanotubes to examine the theoretical prediction are currently underway in our laboratory.

The local feedback effects can be explained by the well-known diffusion mode at an electrode with a large aspect ratio such as band and cylindrical electrodes, which was not considered in previous SECM studies with this class of electrodes.[16,43–46] Among the feedback and local-feedback effects, only a negative local-feedback effect will be observable at a 1D nanostructure without serious limitations by the small lateral dimension, available tip size, or finite electron transfer rate at the substrate. Besides feedback modes, the other operation modes developed for a variety of 2D substrates such as substrate generation–tip collection mode[73] and SECM-induced transfer mode[74] will serve also as a basis of the corresponding local operation mode, enabling SECM studies of chemical reactivity, and ionic and molecular transport at a 1D nanostructure.

The negative local-feedback mode will significantly facilitate electrochemical characterization of 1D nanostructures, which have been recognized as an attractive electrode material for many applications. In contrast to the standard approaches using electrodes based on the nanomaterials, SECM enables non-contact and spatially-resolved measurement. Therefore, SECM will be useful also for characterization of a 1D nanostructure in the electrode format. The local electron-transfer rate at the nanomaterial can be determined under an external potential control by measuring the SECM tip current rather than the direct current response of the nanomaterial so that insulation of the 1D nanostructure and contact electrode is not necessary. At the same time, however, the geometry around the 1D nanostructure must be well defined not only at the length scale of the nanostructure width but also at that of the probe diameter for a quantitative SECM study. Significance of spatially-resolved electrochemical characterization of 1D nanostructures was demonstrated in a recent study, where a defect site of a single-walled carbon nanotube contacted with Au electrodes was labeled with metal by selective electrochemical deposition and identified using AFM.[75]

SUPPORTING INFORMATION

Nanoband electrodes were characterized using cyclic voltammetry (Figure S 3-1). The forward and reverse sweep voltammograms overlap and give slightly peak-shaped waves. The voltammograms fit well with a theoretical diffusion-limited voltammogram given by[76]

$$i = \frac{nFc_0Dl[0.97 - 0.11\exp\left\{-9.9/\ln(5(\xi+1)p^{-2})\right\}}{1+\exp(-\xi)} \tag{S1}$$

with

$$p = \left(\frac{nF\nu w^2}{RTD}\right)^{1/2} \tag{S2}$$

$$\xi = (\frac{nF}{RT})(E - E^{0'}) \tag{S3}$$

where v is the potential sweep rate and E0' is the formal potential. With $D = 8 \times 10^{-6}$ cm^2/s, w = 100 nm, and v = 0.010 V/s, the band length of 2.6 cm was obtained, which agree with the physical length, confirming that the redox reaction at the narrow band surface is diffusion-limited.

In line scan experiments with a 25-µm-diameter Pt disk probe (RG = 10), ascorbic acid was used as an irreversible redox molecule, which gives a negative feedback effect both at conductive and insulating substrates. The tip current based on oxidation of ascorbic acid at the

25-μm-diameter decreases as the tip is brought to a 2 mm-diameter Pt substrate (Figure S 3-2), resulting in an approach curve that fits with a theoretical curve with an insulating substrate. This result is not due to fouling of the Pt substrate surface by products of the oxidation reaction, where a positive feedback effect was observed using $Ru(NH_3)_6^{3+}$ as a reversible mediator. Similarly, positive and negative feedback effects were observed at the Pt substrate using a 10-μm-diameter Pt disk probe with the respective redox molecules.

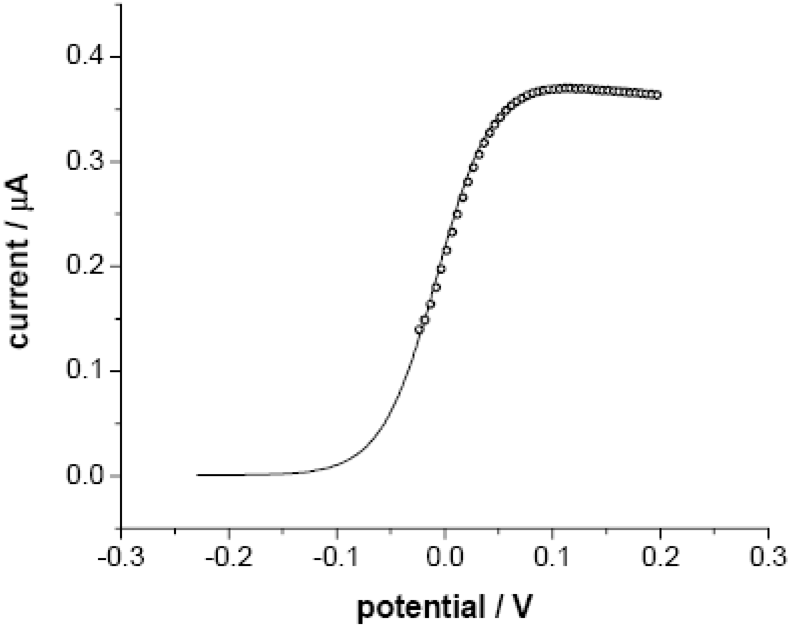

Figure S 3-1. Cyclic voltammograms at a nanoband electrode in 5 mM $Ru(NH_3)_6Cl_3$ with 0.1 MKCl. The solid line is an experimental response and the circles were obtained using eq S1.

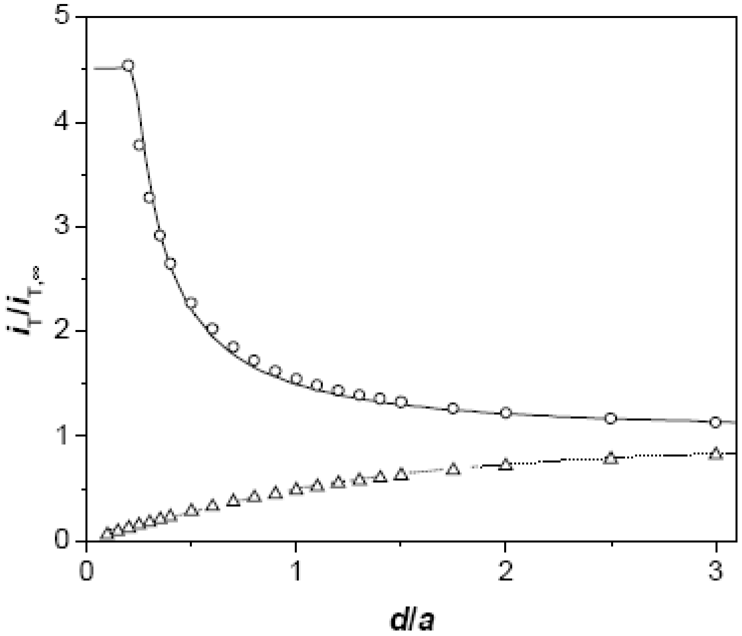

Figure S 3-2. SECM approach curves at a 2-mm-diameter Pt substrate obtained using a 25-μm-diameter Pt disk probe with $Ru(NH_3)_6^{3+}$ (solid line) and ascorbic acid (dotted line) as a redox active molecule in their mixed solution. The circles and triangles represent theoretical approach curves with a conductor and an insulator, respectively.

ACKNOWLEDGEMENTS

We thank the National Science Foundation (DBI-0242561) for financial support. This work was also supported by the Research Corporation and the University of Pittsburgh. The authors thank Prof. A. J. Bard, Department of Chemistry and Biochemistry, University of Texas at Austin, for his advice on nanoband electrode cleaning.

REFERENCES

(1) Bard, A. J. *Integrated Chemical Systems: A Chemical Approach to Nanotechnology*; John Wiley & Sons: New York, 1994.

(2) Watkins, J. J.; Zhang, B.; White, H. S. *J. Chem. Edu.* **2005**, *82*, 712–719.

(3) White, R. J.; White, H. S. *Anal. Chem.* **2005**, *77*, 214A–220A.

(4) Martin, C. R.; Mitchell, D. T. In *Electroanalytical Chemistry, Vol 21*, 1999; Vol. 21, pp 1–74.

(5) Templeton, A. C.; Wuelfing, M. P.; Murray, R. W. *Acc. Chem. Res.* **2000**, *33*, 27–36.

(6) Penner, R. M. *J. Phys. Chem. B* **2002**, *106*, 3339–3353.

(7) Bard, A. J.; Fan, F.-R. F.; Kwak, J.; Lev, O. *Anal. Chem.* **1989**, *61*, 132–138.

(8) Bard, A. J.; Mirkin, M. V., Eds. *Scanning Electrochemical Microscopy*; Marcel Dekker: New York, 2001.

(9) Mirkin, M. V.; Fan, F.-R. F.; Bard, A. J. *Science* **1992**, *257*, 364–366.

(10) Fan, F.-R. F.; Bard, A. J. *Science* **1995**, *267*, 871–874.

(11) Fan, F.-R. F.; Bard, A. J. *Proc. Natl. Acad. Soc.* **1999**, *96*, 14222–14227.

(12) Macpherson, J. V.; Jones, C. E.; Barker, A. L.; Unwin, P. R. *Anal. Chem.* **2002**, *74*, 1841–1848.

(13) Boldt, F.-M.; Heinze, J.; Diez, M.; Petersen, J.; Borsch, M. *Anal. Chem.* **2004**, *76*, 3473–3481.

(14) Lee, S.; Zhang, Y.; White, H. S.; Harrell, C. C.; Martin, C. R. *Anal. Chem.* **2004**, *76*, 6108–6115.

(15) Baltes, N.; Thouin, L.; Amatore, C.; Heinze, J. *Angew. Chem., Int. Ed. Engl.* **2004**, *43*, 1431–1435.

(16) Ufheil, J.; Heβ C.; Borgwarth, K.; Heinze, J. *Phys. Chem. Chem. Phys.* **2005**, *7*, 3185–3190.

(17) Sun, P.; Zhang, Z. Q.; Gao, Z.; Shao, Y. H. *Angew. Chem. Int. Ed. Engl.* **2002**, *41*, 3445–3448.

(18) Bi, S.; Liu, B.; Fan, F.-R. F.; Bard, A. J. *J. Am. Chem. Soc.* **2005**, *127*, 3690–3691.

(19) Guo, J.; Amemiya, S. *Anal. Chem.* **2005**, *77*, 2147–2156.

(20) Quinn, B. M.; Prieto, I.; Haram, S. K.; Bard, A. J. *J. Phys. Chem. B* **2001**, 7474-7476.

(21) A special issue on carbon nanotubes, *Acc. Chem. Res.* **2002**, *36*, 997.

(22) Xia, Y.; Yang, P.; Sun, Y.; Wu, Y.; Mayers, B.; Gates, B.; Yin, Y.; Kim, F.; Yan, H. *Adv. Mater.* **2003**, *15*, 353–389.

(23) Karlsson, M.; Davidson, M.; Karlsson, R.; Karlsson, A.; Bergenholtz, J.; Konkoli, Z.; Jesorka, A.; Lobovkina, T.; Hurtig, J.; Voinova, M.; Owar, O. *Annu. Rev. Phys. Chem.* **2004**, *55*, 613–649

(24) Avouris, P. *Acc. Chem. Res.* **2002**, *35*, 1026–1034.

(25) Kolmakov, A.; Moskovits, M. *Annu. Rev. Mater. Sci.* **2004**, *34*, 151–180.

(26) Wang, J. *Electroanalysis* **2005**, *17*, 7–14.

(27) Girishkumar, G.; Vinodgopal, K.; Kamat, P. V. *J. Phys. Chem. B* **2004**, *108*, 19960–19966.

(28) Che, G.; Lakshmi, B. B.; Fisher, E. R.; Martin, C. R. *Nature* **1998**, *393*, 346–349.

(29) Britto, P. J.; Santhanam, K. S. V.; Ajayan, P. M. *Bioelectrochem. Bioener.* **1996**, *41*, 121–125.

(30) Campbell, J. K.; Sun, L.; Crooks, R. M. *J. Am. Chem. Soc.* **1999**, *121*, 3779–3780.

(31) Day, T. M.; Macpherson, J. V.; Wilson, N. R. *J. Am. Chem. Soc.* **2004**, *126*, 16724–16725.

(32) Heller, I.; Kong, J.; Heering, H. A.; Williams, K. A.; Lemay, S. G.; Dekker, C. *Nano Lett.* **2005**, *5*, 137–142.

(33) Liu, C.-Y.; Bard, A. J.; Wudl, F.; Weitz, I.; Heath, J. R. *Electrochem. Soild-State Lett.* **1999**, *2*, 577–578.

(34) Luo, H.; Shi, Z.; Li, N.; Gu, Z.; Zhuang, Q. *Anal. Chem.* **2001**, *73*, 915–920.

(35) Kwak, J.; Bard, A. J. *Anal. Chem.* **1989**, *61*, 1221–1227.

(36) Wipf D. O.; Bard A. J. *J. Electrochem. Soc.* **1991**, *138*, 469–474.

(37) Delahay, P. *New Instrumental Methods in Electrochemistry*; Interscience: New York, 1954.

(38) Wehmeyer, K. R.; Deakin, M. R.; Wightman, R. M. *Anal. Chem.* **1985**, *57*, 1913–1916.

(39) Bond, A. M.; Henderson, T. L. E.; Thormann, W. *J. Phys. Chem.* **1986**, *90*, 2911–2917.

(40) Morris, R. B.; Franta, D. J.; White, H. S. *J. Phys. Chem.* **1987**, *91*, 3559–3564.

(41) Nagale, M. P.; Fritsch, I. *Anal. Chem.* **1998**, *70*, 2902–2907.

(42) Xu, Q. B.; Gates, B. D.; Whitesides, G. M. *J. Am. Chem. Soc.* **2004**, *126*, 1332–1333.

(43) Borgwarth, K.; Ricken, C.; Ebling, D. G.; Heinze, J. *Fresenius' J. Anal. Chem.* **1996**, *356*, 288–294.

(44) Strike, D. J.; Hengstenberg, A.; Quinto, M.; Kurzawa, C.; Koudelka-Hep, M.; Schuhmann, W. *Mikrochim. Acta* **1999**, *131*, 47–55.

(45) Sklyar, O.; Wittstock, G. *J. Phys. Chem. B* **2002**, *106*, 7499–7508.

(46) Combellas, C.; Fuchs, A.; Kanoufi, F. *Anal. Chem.* **2004**, *76*, 3612–3618.

(47) Norton, J. D.; White, H. S.; Feldberg, S. W. *J. Phys. Chem.* **1990**, *94*, 6772–6780.

(48) Mirkin, M. V. In *Scanning Electrochemical Microscopy*; Bard, A. J., Mirkin, M. V., Eds.; Marcel Dekker: New York, 2001, pp 145–199.

(49) Wightman, R. M.; Wipf, D. O. In *Electroanalytical Chemistry*; Bard, A. J., Ed.; Marcel Dekker: New York, 1989; Vol. 15, pp 267–351.

(50) Bard, A. J.; Denuault, G. H.; Friesner, R. A.; Dornblaser, B. C.; Tuckerman, L. S. *Anal. Chem.* **1991**, *63*, 1282–1288.

(51) Yuan, Y.; Wang, L.; Amemiya, S. *Anal. Chem.* **2004**, *76*, 5570–5578.

(52) Shao, Y.; Mirkin, M. V. *J. Phys. Chem. B* **1998**, *102*, 9915–9921.

(53) Amphlett, J. L.; Denuault, G. *J. Phys. Chem. B* **1998**, *102*, 9946–9951.

(54) Demaille, C.; Unwin, P. R.; Bard, A. J. *J. Phys. Chem.* **1996**, *100*, 14137–14143.

(55) Kanoufi, F.; Cannes, C.; Zu, Y. B.; Bard, A. J. *J. Phys. Chem. B* **2001**, *105*, 8951–8962.

(56) Zhang, J.; Unwin, P. R. *J. Am. Chem. Soc.* **2002**, *124*, 2379–2383.

(57) Liljeroth, P.; Vanmaekelbergh, D.; Ruiz, V.; Kontturi, K.; Jiang, H.; Kauppinen, E.; Quinn, B. M. *J. Am. Chem. Soc.* **2004**, *126*, 7126–7132.

(58) Deakin, M. R.; Wightman, R. M.; Amatore, C. A. *J. Electoanal. Chem.* **1986**, *215*, 49–61.

(59) Aoki, K.; Tokuda, K.; Matsuda, H. *J. Electoanal. Chem.* **1987**, *225*, 19–32.

(60) Alden, J. A.; Booth, J.; Compton, R. G.; Dryfe, R. A. W.; Sanders, G. H. W. *J. Electroanal. Chem.* **1995**, *389*, 45–54.

(61) Lee, C.; Miller, C. J.; Bard, A. J. *Anal. Chem.* **1991**, *63*, 78–83.

(62) Shao, Y.; Mirkin, M. V.; Fish, G.; Kokotov, S.; Palanker, D.; Lewis, A. *Anal. Chem.* **1997**, *69*, 1627–1634.

(63) Katemann, N. B.; Schuhmann, W. *Electroanalysis* **2002**, *14*, 22–28.

(64) Mirkin, M. V.; Bard, A. J. *Anal. Chem.* **1992**, *64*, 2293–2302.

(65) Mirkin, M. V.; Richards, T. C.; Bard, A. J. *J. Phys. Chem.* **1993**, *87*, 7672–7677.

(66) Fan, F.-R. F.; Demaille, C. In *Scanning electrochemical microscopy*; Bard, A. J., Mirkin, M. V., Eds.; Marcel Dekker: New York, 2001, pp 75–110.

(67) Amemiya, S.; Bard, A. J. *Anal. Chem.* **2000**, *72*, 4940–4948.

(68) Xiong, H.; Guo, J. D.; Kurihara, K.; Amemiya, S. *Electrochem. Commun.* **2004**, *6*, 615–620.

(69) Prieto, F.; Coles, B. A.; Compton, R. G. *J. Phys. Chem. B* **1998**, *102*, 7442–7447.

(70) Porat, Z.; Crooker, J. C.; Zhang, Y.; Le Mest, Y.; Murray, R. W. *Anal. Chem.* **1997**, *69*, 5073–5081.

(71) Caston, S. L.; McCarley, R. L. *J. Electoanal. Chem.* **2002**, *529*, 124–134.

(72) Bard, A. J.; Mirkin, M. V.; Unwin, P. R.; Wipf, D. O. *J. Phys. Chem.* **1992**, *96*, 1861–1868.

(73) Engstrom, R. C.; Small, B.; Kattan, L. *Anal. Chem.* **1992**, *64*, 241–244.

(74) Barker, A. L.; Macpherson, J. V.; Slevin, C. J.; Unwin, P. R. *J. Phys. Chem. B* **1998**, *102*, 1586–1598.

(75) Fan, Y.; Goldsmith B. R.; Collins P. G. *Nature Mater.* **2005**, *4*, 906–911.

(76) Aoki, K.; Tokuda, K. *J. Electoanal. Chem.* **1987**, *237*, 163-170.

4.0 PROBING HETEROGENEOUS ELECTRON TRANSFER AT AN UNBIASED CONDUCTOR BY SCANNING ELECTROCHEMICAL MICROSCOPY IN THE FEEDBACK MODE

This work has been published as Hui Xiong, Jidong Guo, and Shigeru Amemiya, *Anal. Chem.,* 2006, 79, 2735-2744.

4.1 ABSTRACT

The theory of the feedback mode of scanning electrochemical microscopy is extended for probing heterogeneous electron transfer at an unbiased conductor. A steady-state SECM diffusion problem with a pair of disk ultramicroelectrodes as a tip and a substrate is solved numerically. The potential of the unbiased substrate is such that the net current flow across the substrate/solution interface is zero. For a reversible substrate reaction, the potential and the corresponding tip current depend on SECM geometries with respective to the tip radius including not only the tip–substrate distance and the substrate radius but also the thickness of the insulating sheath surrounding the tip. A larger feedback current is obtained using a probe with a thinner insulating sheath, enabling identification of a smaller unbiased substrate with a radius that is approximately as small as the tip radius. An intrinsically slow reaction at an unbiased substrate

as driven by a SECM probe can be quasi-reversible. The standard rate constant of the substrate reaction can be determined from the feedback tip current when the SECM geometries are known. The numerical simulations are extended to an SECM line scan above an unbiased substrate to demonstrate a “dip” in the steady-state tip current above the substrate center. The theoretical predictions are confirmed experimentally for reversible and quasi-reversible reactions at an unbiased disk substrate using disk probes with different tip radii and outer radii.

4.2 INTRODUCTION

Scanning electrochemical microscopy (SECM) is a powerful electroanalytical technique for probing interfacial reactions at a variety of substrates.[1-3] SECM is versatile partially because the substrates do not require an electrical connection to an external circuit,[4] which is in contrast to traditional electroanalytical techniques.[5] SECM measurement of unbiased substrates is advantageous when the substrates can not be conveniently connected to an external circuit or when the application of a potential causes an undesirable effect on the substrates. In particular, SECM feedback mode has been used in recent studies of charge transport at unbiased nanostructured systems such as metal nanoparticle arrays/films,[6-13] carbon nanotube network,[14] individual nanobands,[15] an array of protein nanopores,[16] and nanometer-thick polymer films.[17-20]

A heterogeneous electron transfer process at an unbiased conductor can be studied by SECM in the feedback mode, where the process is driven and monitored using an ultramicroelectrode (UME) probe. Consider a disk UME positioned within a short distance (usually within about the tip diameter) of a disk-shaped conductive substrate (Figure 4-1). The UME tip is biased for electrolysis of a redox-active mediator, O, in the electrolyte solution (O +

*n*e$^-$ → R; process 1 in Figure 4-1). The tip-generated species, R, diffuses to and reacts at the surface of the conductive substrate directly under the tip (process 2). The mediator regeneration process at the substrate can be monitored as enhancement of the tip current. Steady-state mediator regeneration at an unbiased substrate is coupled with electron transport in the substrate and mediator electrolysis at the exterior surface of the substrate (process 3), resulting in a mixed potential of the substrate.

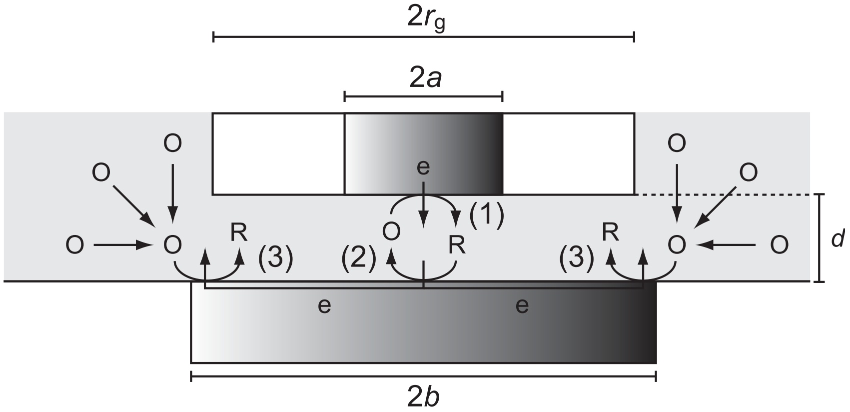

Figure 4-1. Scheme of a SECM feedback experiment with a disk UME probe positioned above a disk substrate electrode at open circuit potential.

A semiquantitative model for unbiased disk substrates predicts that mediator diffusion limits an intrinsically fast mediator regeneration at a sufficiently large or small substrate.[21] When the area of an unbiased substrate is at least 1000 times larger than the tip area, a sufficiently large exterior surface of the substrate is exposed to the bulk solution so that the substrate potential is set by the bulk concentration of the mediator to drive the mediator regeneration to the diffusion limit. Therefore, as the tip is brought to the substrate surface, the tip current that is controlled by mediator diffusion between the tip and the substrate increases monotonically, yielding an approach curve (a plot of the tip current versus the tip–substrate distance) based on pure positive feedback. On the other hand, when the tip size is comparable to the substrate size, no mediator regeneration is expected at the steady state.[21] In this case, the tip current is limited by mediator diffusion from the bulk solution to the tip. In fact, a pair of disk Pt UMEs with the same diameter were used as a substrate and a probe to demonstrate an approach curve based on pure negative feedback, where the tip current decreases monotonically to zero at shorter tip–substrate distances.[22] During the tip approach, the open circuit potential of the unbiased substrate varies with the tip–substrate distance such that no mediator regeneration occurs on the substrate surface.[23]

SECM feedback can be controlled also by electron transfer at an unbiased substrate. Mediator electrolysis at the exterior surface of the substrate controls the feedback current when the substrate area is larger than the tip area by a factor of less than 1000.[21] At an unbiased disk substrate of intermediate size, a smaller feedback current is obtained using a disk probe with a larger diameter.[24] Moreover, the feedback current can be controlled by kinetics of mediator regeneration at the substrate.[21] A smaller feedback current is expected for an intrinsically slower reaction at an unbiased substrate. Recently, the theory for biased substrates[25] was used to determine electron-transfer rates at unbiased substrates from a kinetically limited tip current.[26-28] The assumption of irreversible kinetics in the analyses, however, is not valid for an unbiased substrate where both regeneration and electrolysis of a mediator occur. In addition, the open circuit potential of an unbiased substrate varies with the tip–substrate distance to give a distance-dependent reaction rate, which is in contrast to a constant reaction rate with a biased substrate at a fixed potential.

Here we report on numerical simulations of SECM feedback effects at unbiased substrates with high conductivity. A steady-state SECM diffusion problem is solved numerically for a disk probe positioned above an unbiased disk substrate, where the substrate potential is such that the net current flow across the substrate/solution interface is zero. Effects of the substrate size and heterogeneous electron transfer kinetics on the mixed potential of the substrate and the tip current are studied theoretically and experimentally. The SECM feedback is found to depend also on the thickness of the insulating layer surrounding the metal disk probe, which hinders mediator diffusion from the bulk solution to the substrate. The numerical simulations are extended to an SECM line scan above an unbiased disk substrate to demonstrate that the tip current is less enhanced above the substrate center than above the substrate edge, resulting in a current "dip."

4.3 THEORY

4.3.1 Model

An SECM diffusion problem with a pair of disk-shaped UMEs as a probe and a substrate is defined in a cylindrical coordinate (Figure 4-2). The origin of the coordinate axes is set at the center of the disk UME probe. The *r* and *z* coordinates are in directions that are parallel and normal to the disk probe surface, respectively. The disk substrate electrode is faced in parallel to the probe surface such that the substrate center is directly under the probe center. Disk radii of the probe and substrate electrodes are given by *a* and *b*, respectively. An insulating sheath with

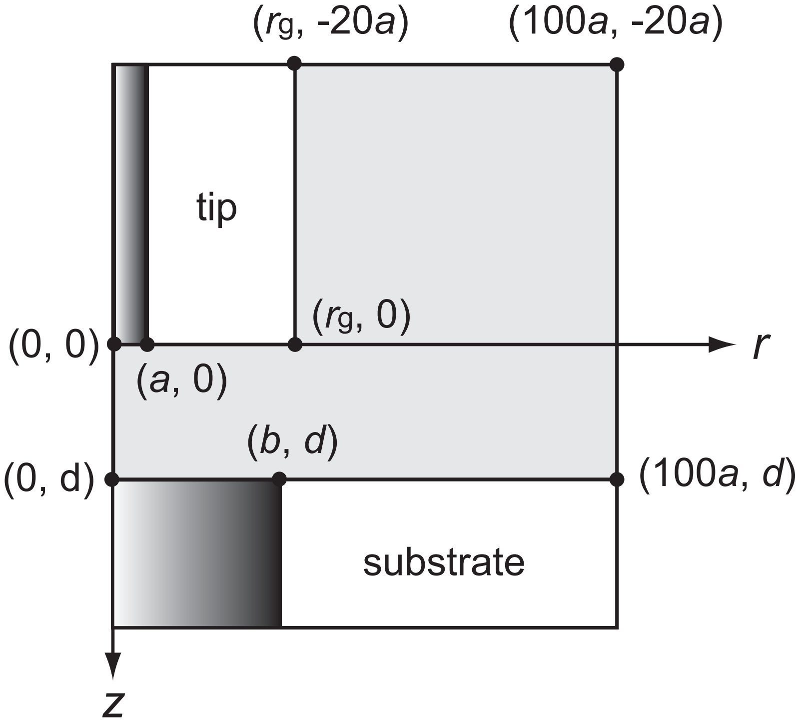

Figure 4-2. Geometry of the SECM diffusion problem in a cylindrical coordinate.

the outer radius of r_g surrounds the tip. The outer substrate radius corresponds to $100a$ and limits the simulation space in the r-direction. The simulation space behind the tip is defined by the value of $20a$, which is large enough to accurately simulate back diffusion of a mediator at a probe with RG < 10.[29]

Initially, the solution phase contains only one redox-active mediator, O, which is reduced to R at the tip (O + ne → R). Steady-state diffusion of O in the solution phase can be expressed as

$$\frac{\partial c(r,z)}{\partial t} = D\left[\frac{\partial^2 c(r,z)}{\partial r^2} + \frac{1}{r}\frac{\partial c(r,z)}{\partial r} + \frac{\partial^2 c(r,z)}{\partial z^2}\right] = 0 \qquad (1)$$

where $c(r,z)$ is the steady-state local concentration of the mediator. The initial condition is given by

$$c(r,z) = c_0 \qquad t = 0 \qquad \text{(in the electrolyte solution)} \qquad (2)$$

The diffusion coefficients of O and R are assumed to be the mean value so that mathematical treatment is restricted to the concentration of O.

The disk SECM probe is biased such that mediator electrolysis at the tip is diffusion-limited in the bulk solution. When the tip is positioned far from the substrate, a steady-state limiting current, $i_{\mathrm{T},\infty}$, is obtained as

$$i_{\mathrm{T},\infty} = 4xnFDc_0a \qquad (3)$$

where x is a function of RG (= r_g/a),[30] F is the Faraday constant, and D and c_0 are the diffusion coefficient and concentration of the redox mediator in the bulk solution.

The substrate is assumed to be conductive enough to maintain a uniform potential within the phase. A steady-state current across the unbiased substrate/solution interface, i_{S}, is zero as given by

$$i_{\mathrm{S}} = 2\pi nFD\int_0^b r\left[\frac{\partial c(r,d)}{\partial z}\right]dr = 0 \tag{4}$$

The substrate surface boundary condition depends on electrochemical reversibility of the substrate reaction. For a reversible reaction, the boundary condition is given by

$$E = E^{0'} - \frac{RT}{nF}\ln\frac{c_0 - c(r,d)}{c(r,d)} \tag{5}$$

where E is the open circuit potential of the unbiased substrate, and $E^{0'}$ is the formal potential. When the substrate reaction is kinetically limited, only one-step, one-electron transfer processes ($n = 1$) are considered

$$\mathrm{O} + \mathrm{e} \underset{k_{\mathrm{b,s}}}{\overset{k_{\mathrm{f,s}}}{\rightleftharpoons}} \mathrm{R} \tag{6}$$

where $k_{\mathrm{f,s}}$ and $k_{\mathrm{b,s}}$ are the first-order heterogeneous rate constants. The rate constants are given by the Butler-Volmer relations[31]

$$k_{\mathrm{f,s}} = k^0 \exp[-\alpha F(E - E^{0'})/RT] \tag{7}$$

$$k_{\mathrm{b,s}} = k^0 \exp[(1-\alpha)F(E - E^{0'})/RT] \tag{8}$$

where k^0 is the standard rate constant, and is the transfer coefficient. The corresponding substrate surface boundary condition is given by

$$D\left[\frac{\partial c(r,z)}{\partial z}\right]_{z=d} = -k_{\mathrm{f,s}}c(r,d) + k_{\mathrm{b,s}}[c_0 - c(r,d)] \qquad (0 < r < b, z = d) \tag{9}$$

A dimensionless rate constant, K, for the substrate reaction is defined by

$$K = \frac{k^0 a}{D} \tag{10}$$

The other boundary conditions are given by

$$c(r,0) = 0 \qquad 0 < r < a \qquad \text{(tip surface)} \tag{11}$$

$$\left[\frac{\partial c(r,z)}{\partial z}\right]_{z=0} = 0 \qquad a < r < r_{\mathrm{g}} \qquad \text{(insulator)} \tag{12}$$

$$\left[\frac{\partial c(r,z)}{\partial r}\right]_{r=r_g} = 0 \qquad -20a < z < 0 \qquad \text{(insulator)} \tag{13}$$

$$c(r,z) = c_0 \qquad r_{\mathrm{g}} < r < 100a,\ z = -20a \text{ and}$$

$$r = 100a,\ -20a < z < d \ \text{(simulation space limits)} \tag{14}$$

$$\left[\frac{\partial c(r,z)}{\partial r}\right]_{r=0} = 0 \qquad 0 < z < d \qquad \text{(axis of symmetry)} \tag{15}$$

The SECM diffusion problem was solved in a dimensionless form by COMSOL Multiphysics® version 3.2 (COMSOL, Inc., Burlington, MA), which applies the finite element method (see Supporting Information). An open circuit potential of the substrate was chosen such that the substrate current is less than 1% of $i_{\mathrm{T},\infty}$ to satisfy eq 4. The corresponding tip current, i_{T}, is given by

$$i_{\mathrm{T}} = 2\pi nFD\int_0^a r\left[\frac{\partial c(r,0)}{\partial z}\right]dr \tag{16}$$

Plots of the tip current and substrate potential versus the tip−substrate distance give current and potential approach curves, respectively. Calculation at each distance took 1–10 s on a workstation equipped with a Xeon 3.0 GHz processor unit and 5.0 GB RAM with Linux.

4.3.2 Finite Substrate Effect for Reversible Reaction

For a reversible reaction at an unbiased finite substrate, the feedback is controlled by mediator electrolysis at the limited exterior surface of the substrate (process 3 in Figure 4-1). Both current and potential approach curves depend on two dimensionless parameters, *b*/*a* and RG. The relative size of the substrate, *b*/*a*, determines the area of the exterior substrate surface that is exposed to the bulk solution for the mediator electrolysis. The relative thickness of the insulating sheath, RG, determines diffusional accessibility of the exterior surface to the mediator in the bulk solution.

Current and potential approach curves at unbiased disk substrates with different radii were calculated for a SECM probe with a standard RG of 10. At a small substrate with $b/a < 2$, the current approach curve coincides with a negative approach curve as obtained at an insulating substrate (Figure 4-3a). In this case, an open circuit potential of the substrate is so negative that no mediator regeneration occurs (Figure 4-3b), resulting in pure negative feedback. In previous SECM studies, disk-shaped tip and substrate electrodes with the same radius was considered to demonstrate pure negative feedback at an unbiased substrate.[22, 23] At a large substrate with $b/a \geq 30$, the current approach curve is very similar to a curve based on pure positive feedback. The potential of the large substrate is positive enough to drive the mediator regeneration to the diffusion limit. The range of *b*/*a* that results in pure positive feedback agrees with a semi-quantitative estimation.[21] For an intermediate substrate radius of $2 < b/a < 30$, the tip current is enhanced more with a larger substrate, where a larger exterior surface of the substrate with more positive potential is available for mediator electrolysis. Interestingly, the current approach curve changes dramatically when the substrate radius is comparable to the thickness of the insulating sheath around the tip ($b/a \sim \mathrm{RG} = 10$). At a substrate with $b/a = \mathrm{RG}$, the tip current increases

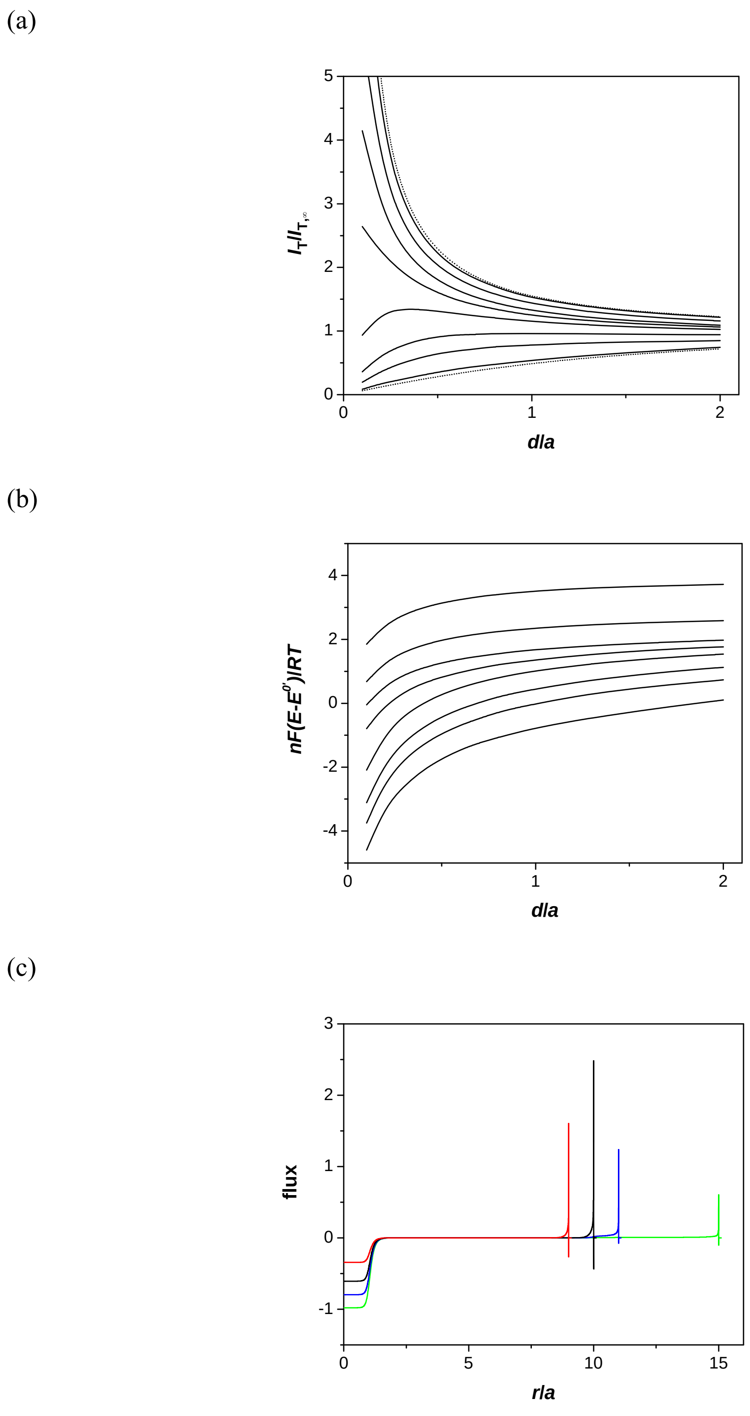

Figure 4-3. Effect of the substrate radius on (a) current and (b) potential approach curves with a disk UME probe with RG = 10. The solid lines are for b/a = 30, 15, 11, 10, 9, 7, 5, and 2 from the top. The upper and lower dotted lines in (a) represent theoretical approach curves with conductive and insulating substrates, respectively.[29] (c) Distribution of interfacial mediator flux at the surface of unbiased substrates with b/a = 9 (red), 10 (black), 11 (blue), and 15 (green) under a disk probe with RG = 10. The flux at the substrate surface is given in the dimensionless form as $0.25[\partial C(R,Z)/\partial Z]_{Z=L}$ (see Supporting Information for definitions of dimensionless parameters).

monotonically as the tip–substrate distance decreases. When the substrate is slightly smaller than the outer diameter of the tip (*b*/*a* = 9), the tip current is suppressed significantly at short tip−substrate distances.

The dependence of the feedback current on the substrate size can be explained by considering localized distribution of interfacial mediator flux on the substrate surface (Figure 4-3c). At a short tip–substrate distance of d/a = 0.5, the flux based on mediator regeneration is localized on the substrate surface directly under the tip. This result indicates that the substrates with *b*/*a* = 9–15 are large enough to collect most tip-generated species. In fact, collection efficiency is close to unity at a biased substrate that is a few times larger than the tip, resulting in pure positive feedback.[32] In contrast to the biased substrate, however, pure positive feedback is not obtained at the unbiased substrates with the intermediate sizes, where mediator regeneration is coupled with mediator electrolysis at the exterior surface of the substrates. Importantly, the flux based on the mediator electrolysis is localized at the substrate edge. The edge of a larger substrate is more accessible to the mediator in the bulk solution, enhancing the mediator regeneration and subsequently the tip current. Moreover, mediator diffusion from the bulk solution to the substrate edge is significantly hindered by the insulating sheath of the tip, when the substrate radius is comparable to or smaller than the tip outer radius. Thus, a large RG effect on the tip current is observed for RG ~ *b*/*a*.

4.3.3 RG Effect on the Detectable Substrate Size

The RG effect at an unbiased substrate, which has not been considered in any previous SECM study,[21, 23, 33] was further confirmed by simulating approach curves for probes with different outer diameters (Figure 4-4a). With *b*/*a* = 10, current approach curves change from negative to positive as RG changes from 50 to 1.1. This RG effect on the tip current at an unbiased conductive substrate is much larger than the well-known RG effect at an insulating substrate,[34] where the tip current varies with RG, but only decreases monotonically as the tip is brought closer to an insulating substrate.

A smaller unbiased substrate on an insulating plane can be resolved using a probe with a thinner insulating sheath, which gives a larger feedback current. When a probe with a small RG of 1.1 is brought into the proximity of an unbiased substrate with $b/a \geq 1.1$, the tip current is significantly larger than that at an insulating substrate (Figure 4-4b). The substrate size of b/a = 1.1 is half of the smallest size of an unbiased substrate that can be detected using a probe with RG = 10 (Figure 4-3a). The *b*/*a* values of 1.1–2.0, however, are approximately 10 times larger than the corresponding values of 0.1–0.2 for the smallest biased substrate that is detectable in the feedback mode. This result is due to the need for an exterior surface of an unbiased substrate, where mediator electrolysis occurs to balance mediator regeneration under the tip. It should also be noted that, even using the probe with a small RG of 1.1, pure positive feedback is obtained at a large unbiased substrate with $b/a > 30$, which is much larger than the corresponding biased substrate ($b/a > \sim 1$).[35] The range of $b/a > 30$ as required for a probe with RG of 1.1–10 is consistent with the semi-quantitative estimation,[21] which is a good approximation when the substrate radius is sufficiently larger than the tip outer radius.

(a)

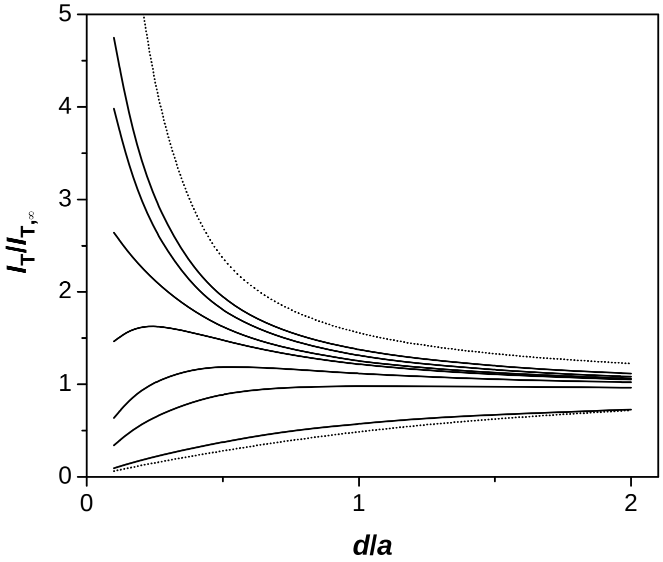

(b)

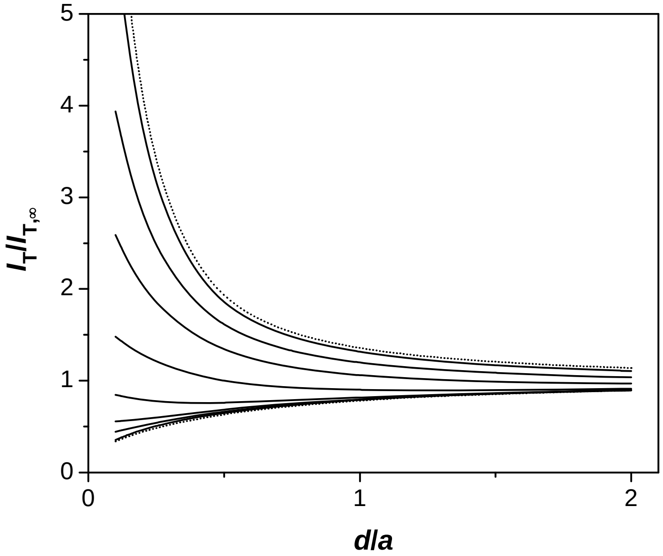

Figure 4-4. A RG effect on current approach curves with unbiased disk substrates as simulated for disk UME probes: (a) *b*/*a* = 10 and RG = 1.1, 6, 9, 10, 10.5, 12, 15, 50 from the top, and (b) RG = 1.1 and *b*/*a* = 30, 10, 5, 2.5, 1.5, 1.2, 1.1, and 1.0 from the top. The upper and lower dotted lines represent theoretical approach curves with conductive and insulating substrates, respectively.[29] The corresponding potential approach curves are shown in Supporting Information.

4.3.4 Kinetically Limited Approach Curves

The tip current and substrate potential also depend on the kinetics of heterogeneous electron transfer at an unbiased substrate. Compared with biased substrates, theoretical treatment of kinetic effects at unbiased substrates is more complicated. First, quasi-reversible kinetics must be considered at an unbiased substrate, where both mediator electrolysis and regeneration occur at the steady state to maintain the charge balance in the substrate. Thus, an approximation of irreversible kinetics[25] is not valid for an unbiased finite substrate. Second, the corresponding rate constants must be given as a function of the substrate potential, which varies with the SECM geometries with respect to the tip radius including the tip–substrate distance, substrate radius, and tip outer diameter. Each rate constant is defined by two kinetic parameters, k^0 and α, and the overpotential, $E - E^{0'}$, on the basis of the Butler-Volmer model (see eqs 7 and 8).

At a large substrate with $b = 30a$, a current approach curve for a substrate reaction with $K > 10$ is based on pure positive feedback ($\alpha = 0.5$ in Figure 4-5a). A current approach curve for smaller K is more negative because of a kinetic limitation. With $K < 2.5 \times 10^{-4}$, a current approach curve is similar to a negative one as observed at an insulating substrate, indicating that the substrate reaction is intrinsically too slow to regenerate the mediator. The substrate potential is significantly more positive than $E^{0'}$ at the large substrate and becomes more positive for a slower reaction at short tip–substrate distances (Figure 4-5b). Due to the large overpotential at the large substrate, the transfer coefficient also affects the tip current and substrate potential substantially (see Supporting Information). Thus, the determination of K (or α) at a large substrate requires prior knowledge of α (or *K*). Alternatively, a pair of approach curves obtained in solutions containing species O or R will allow the determination of both parameters.

Current and potential approach curves at a smaller substrate ($b/a = 9$) are sensitive to *K* but not to *α* (see Supporting Information). A range of *K* for a kinetic limitation with the smaller substrate is very similar to that at the larger substrate. For both substrates, the largest *K* value that results in a quasi-reversible substrate reaction is equal to 10, corresponding to $k^0 = 0.1–1.0$ cm/s for standard values of $a = 1–10$ μm and $D = 1.0 \times 10^{-5}$ cm^2/s (see eq 10). Either tip current or substrate potential at the small substrate is not sensitive to α, because of smaller overpotentials. Therefore, *K* can be estimated directly from an approach curve at a small substrate, where α can not be addressed.

4.3.5 RG Effect on Line Scan

A steady-state tip current in a line scan above an unbiased disk substrate was obtained numerically for reversible substrate reactions. The diffusion problem was solved in a three-dimensional coordinate as reported elsewhere.[15] Interestingly, tip current is more enhanced above the substrate edge than above the center, resulting in a line scan with a current dip. For instance, such a current dip is shown in a line scan above an unbiased substrate with $b/a = 5$ as obtained using a probe with RG = 10 (solid line in Figure 4-6a). A larger tip current is obtained above the substrate edge, where the mediator in the bulk solution is more accessible to the substrate through the opposite side of the edge (Figure 4-6b). When the probe is positioned directly above the substrate center, mediator diffusion from the bulk solution to the whole substrate edge is uniformly hindered by the insulating sheath, resulting in the current dip. In fact,

(a)

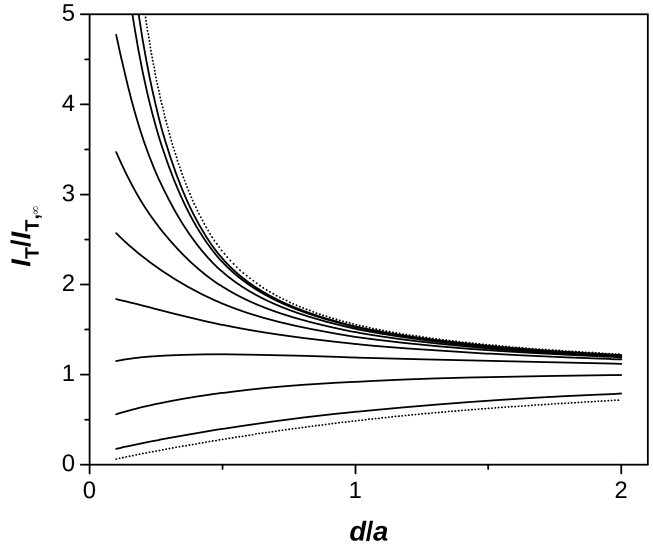

(b)

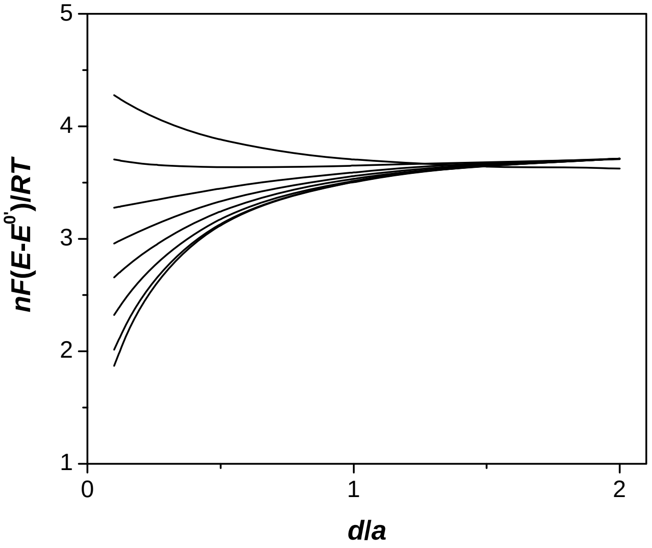

Figure 4-5. Effect of the intrinsic rate of the substrate reaction on (a) current and (b) potential approach curves with an unbiased disk substrate with b/a = 30 under a disk UME probe with RG = 10. The solid lines are for K = 10, 1, 0.25, 0.1, 0.05, 0.025, 0.01, 0.0025, and 0.00025 from (a) the top and (b) the bottom. The upper and lower dotted lines in (a) represent theoretical approach curves with conductive and insulating substrates, respectively.[29]

a current dip above the substrate center is much smaller for a probe with RG = 4 (dotted line in Figure 4-6a).

A similar current dip above the substrate center was reported previously in SECM images using a pair of 25-µm-diameter Pt disk electrodes both as a probe and an unbiased substrate.[22] Line scans in the images, however, were asymmetric with respect to the substrate center; the tip current above the edge before probe's passing the center was larger than that above the opposite side of the edge after passing the center. The asymmetric line scan with a current dip was ascribed to a transient current response. In our numerical simulations, symmetric line scans with a current dip were obtained at the steady state. Unfortunately, numerical simulations of a transient tip current at an unbiased substrate are difficult, because the mixed potential of the substrate also varies with time. Therefore, we will demonstrate experimentally that a current dip is still observed in the steady-state line scan at slow scan rates, where the non-steady-state asymmetric response is not observed.

(a)

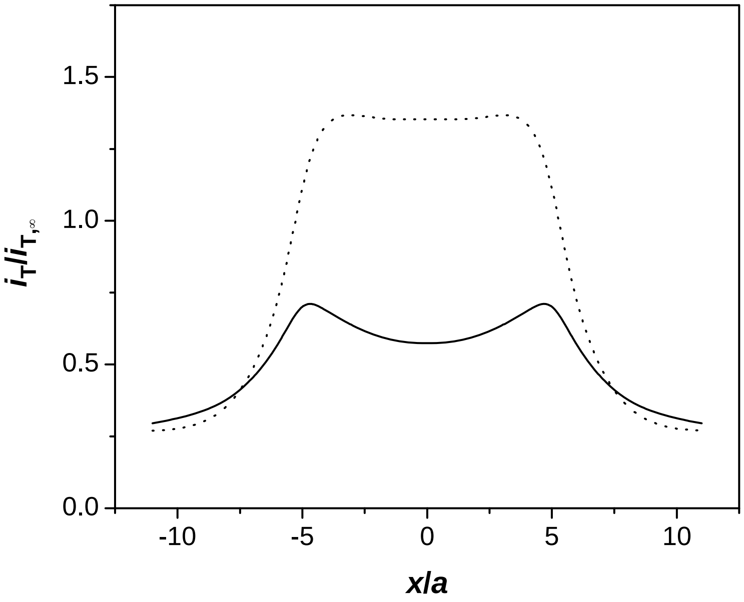

(b)

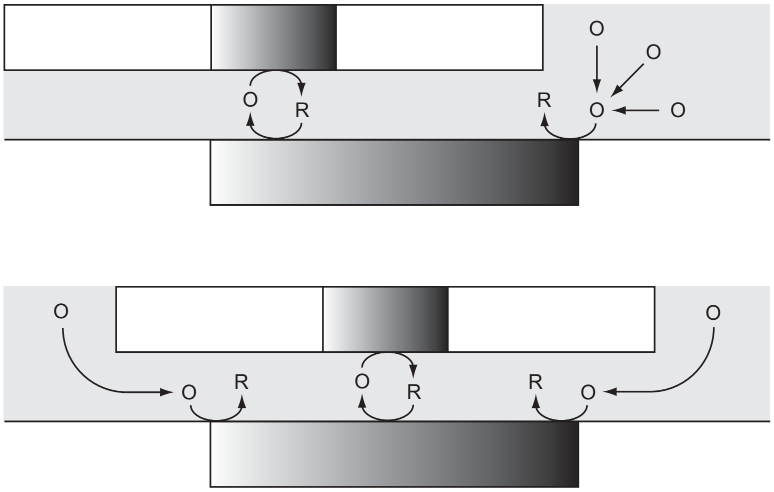

Figure 4-6. (a) Tip currents in line scans over an unbiased disk substrate with $b/a = 5$ as simulated for a disk probe with RG = 10 (solid line) and 4 (dotted line) at $d/a = 0.5$. (b) Scheme of mediator diffusion from the bulk solution to the substrate edge when the tip is positioned above the edge (top) and the center (bottom) of the substrate.

4.4 EXPERIMENTAL SECTION

4.4.1 Chemicals

Tris(1,10-phenanthroline)cobalt (II), $Co(phen)_3^{2+}$, and 1,1'-ferrocenedimethanol (Strem Chemicals, Newburyport, MA) were used as redox mediators. $Co(phen)_3^{2+}$ was obtained from stoichiometric amounts of $CoCl_2·6H_2O$ (Fisher Chemical, Fair Lawn, NJ) and 1,10-phenanthroline (Aldrich, Milwaukee, WI) in 0.1 M KCl. The mediator solutions were prepared under nitrogen in a glove bag (Aldrich) to avoid oxidation of the mediator by oxygen.[36] All reagents were used as received. All aqueous solutions were prepared with 18.3 MΩ·cm deionized water (Nanopure, Barnstead, Dubuque, IA).

4.4.2 Electrode Fabrication and Characterization

A ~33 μm-diameter carbon fiber disk substrate electrode, and 6, 10, and 25 μm-diameter Pt disk probes were fabricated as described previously.[37, 38] The Pt wires were obtained from Goodfellow (Devon, PA). The carbon fiber was purchased from World Precision Instruments (Sarasota, FL). The diameter of the inlaid carbon fiber electrode was determined from a limiting current of a steady-state voltammogram using eq 3 with $x = 1$. The voltammogram was also used to determine $E^{0'}$. The tip radius and insulating sheath thickness of the Pt probes were determined from current approach curves at an insulating Teflon substrate[29, 39] measured using a home-built

SECM setup[40] and were also checked by optical microscopy. For probes with RG ~ *b*/*a*, the RG values could be determined more accurately using the carbon fiber substrate at open circuit potential than using the insulating substrate (see Results and Discussion).

4.4.3 SECM Measurements

Approach curve and imaging experiments were performed using a commercial SECM instrument with close-loop piezoelectric motors, CHI 910B (CH Instruments, Austin, TX). The SECM instrument was placed on a vibration isolation platform (model 63-533, TMC, Peabody, MA). A two-electrode setup was employed with a 1 mm-diameter AgCl-coated Ag wire serving as a reference/counter electrode and a Pt disk electrode as a SECM probe. The open circuit potential of the carbon fiber substrate was measured with respect to another Ag/AgCl reference electrode using a 16-channel potentiometer (Lawson Labs Inc., Malvern, PA). The tip current and the open circuit potential of the substrate were measured simultaneously during tip approach to obtain current and potential approach curves, respectively. For approach curve measurements, a probe was positioned directly above the substrate as shown in Figure 2, where the largest tip current was obtained by setting the substrate potential for diffusion-limited mediator regeneration.[23] SECM measurements with $Co(phen)_3^{2+}$ were carried out in the globe bag filled with nitrogen.

4.5 RESULTS AND DISCUSSION

4.5.1 Finite Substrate Effect

Effects of the substrate size on the tip current and substrate potential were examined using 1,1'-ferrocenedimethanol as a reversible mediator. A ~33 um-diameter carbon fiber electrode was used as a model conductive substrate without the external control of the potential. Current approach curves were obtained using 6-, 10-, and 25-μm-diameter disk Pt probes with RG = 7.5, 8.0, and 10, respectively (Figure 4-7a). Simultaneous measurements of an open circuit potential of the substrate (Figure 4-7b) did not affect the tip current. For a Pt probe with a smaller diameter, the tip current is enhanced more, indicating more efficient mediator regeneration at the substrate surface directly under the tip. With a smaller probe, a larger exterior surface of the substrate is available for oxidation of the ferrocene mediator so that the substrate potential is more negative. The more negative substrate potential results in more efficient reduction of the tip-generated ferrocenium at the substrate, giving the larger tip current.

The current and potential approach curves were analyzed to quantify the feedback effect at the unbiased conductive substrate. The current approach curves fit well with theoretical curves for a reversible substrate reaction (Figure 4-7a). The reversible behavior is consistent with a large standard rate constant of ferrocene derivatives at carbon electrodes, e.g., k0 = 0.19 cm/s for ferrocenemethanol at a glassy carbon electrode.41 The geometrical parameters of b/a and RG in the best fits are consistent with those determined by optical microscopy. The current approach curve obtained with the 25 μm-diameter probe also fits with a theoretical curve for an insulating

(a)

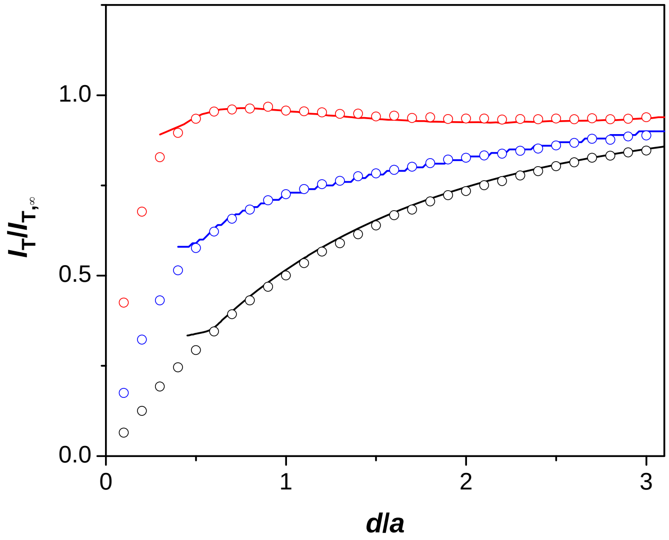

(b)

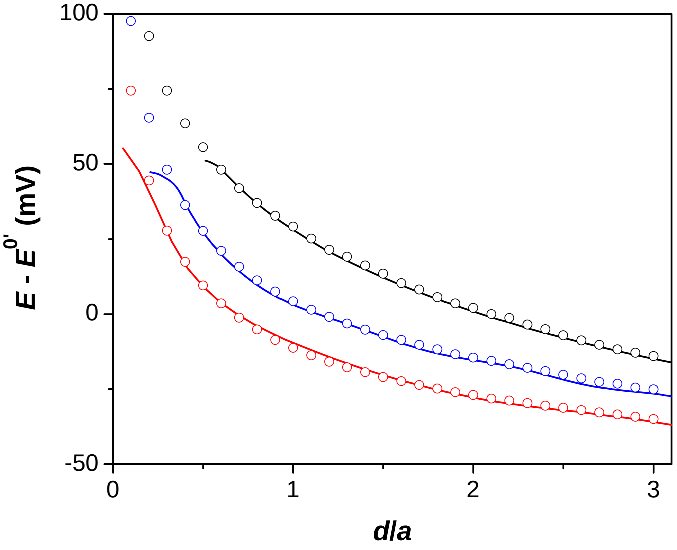

Figure 4-7. (a) Current and (b) potential approach curves at an unbiased disk carbon fiber substrate as obtained using disk Pt probes with 1 mM 1,1'-ferrocenedimethanol in 0.1 M KCl. The circles and solid lines represent the experimental and theoretical curves, respectively. (*a*, *b/a*, RG) = (12.5 µm, 1.29, 10.0), (5.0 µm, 3.65, 8.0), and (3.0 µm, 5.61, 7.5) were used for the data in red, blue, and black. The tip potential: 0.4 V versus Ag/AgCl. The probe scan rate: 1.5 µm/s for *a* = 12.5 µm, and 0.6 µm/s for *a* = 5.0 and 3.0 µm.

substrate, indicating that the unbiased substrate is too small in comparison with the probe diameter to regenerate the mediator. The geometrical parameters can be used to obtain theoretical potential approach curves that fit well with the experimental curves (Figure 4-7b). This result indicates that the measurement of the substrate potential is not necessary for analysis of the current approach curve. Therefore, theoretical analysis is also possible with an unbiased substrate that can not be connected to an external circuit for potential measurement.

4.5.2 RG Effect

The quantitative theory of SECM feedback at an unbiased substrate predicts that both tip current and substrate potential depend on the tip outer radius, especially when the radius is comparable to the substrate radius (Figure 4-3a). The insulating sheath around the tip hinders mediator diffusion from the bulk solution to the substrate edge, where mediator electrolysis occurs to maintain the steady-state mediator regeneration under the tip (Figure 4-3c). The RG effect was studied experimentally using a 10 μm-diameter disk Pt probe with a thin insulating sheath. With 1,1'-ferrocenedimethanol as a reversible mediator, the tip current increased monotonically as the tip was brought to the unbiased carbon fiber substrate (red solid line in Figure 4-8a). This result is in contrast to the negative approach curve obtained using the 10 μm-diameter probe with RG = 8 (blue solid line in Figure 4-7a), confirming that a probe with smaller RG gives a larger feedback current at an unbiased substrate. The substrate potential is more negative for the probe with smaller RG (Figure 4-8b), resulting in a larger feedback current based on more facilitated reduction of the tip-generated ferrocenium.

(a)

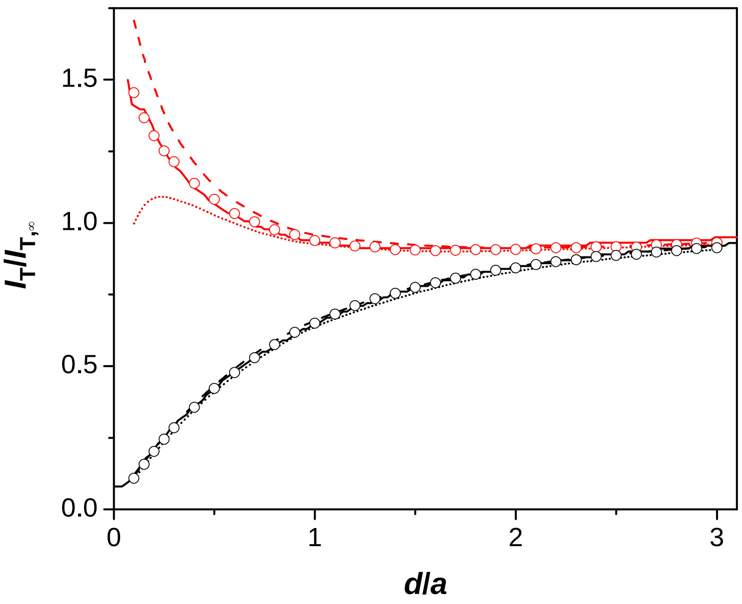

(b)

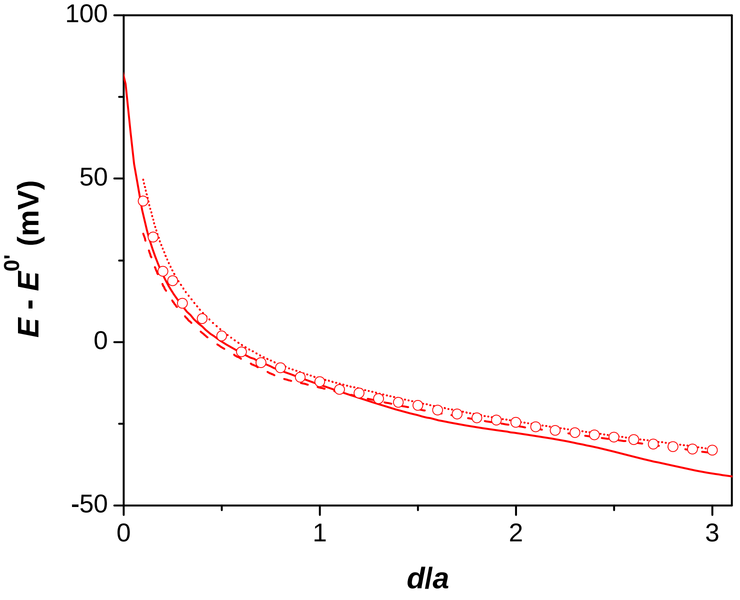

Figure 4-8. (a) Current approach curves at a 34 μm-diameter disk carbon fiber electrode at open circuit potential (red) and at a Teflon substrate (black) as obtained using a 10 μm-diameter Pt disk probe with RG = 3.3. (b) The corresponding potential approach curve at the carbon fiber substrate. The solid lines represent the experimental curves. The circles, dashed line, and dotted line represent theoretical curves with RG = 3.3, 3.1, and 3.5, respectively. The approach curves were measured with 1 mM 1,1'-ferrocenedimethanol in 0.1 M KCl. The tip potential: 0.4 V versus Ag/AgCl. The probe scan rate: 0.6 μm/s.

The positive current approach curve obtained using the 10 μm-diameter probe with small RG fits well with a theoretical curve for a reversible substrate reaction (Figure 4-8a), yielding RG = 3.3. Theoretical curves with a slightly smaller or larger RG value of 3.1 or 3.5, respectively, do not fit with the experimental curve. The theoretical tip current is highly sensitive to RG in this case, because the substrate diameter of 34 μm is comparable to the tip outer diameter of 33 μm. On the other hand, the effect of the tip outer diameter on the corresponding potential approach curves is small (Figure 4-8b) because the substrate potential depends on the logarithm of the mediator concentration at the substrate surface for a reversible reaction (see eq 5).

The RG effect at an unbiased substrate is much more significant than the well-known RG effect at an insulating substrate.[29, 34, 42] A negative current approach curve at a Teflon substrate as obtained using the probe with RG = 3.3 (black solid line in Figure 4-8a) fits with any of the theoretical curves with RG = 3.1–3.5 at an insulating substrate, which nearly superimpose each other. It should also be noted that the current approach curve obtained using the 10 μm-diameter probe with RG = 3.3 is more positive than that obtained with the 6 μm-diameter probe with RG = 7.5 (Figure 4-7a) because the outer diameter of the former probe is smaller than that of the latter. The RG effect, however, is also significant in the current approach curve with the 6 μm-diameter probe, where the maximum current at d/a = 0.8 can not be reproduced theoretically with an RG of 7 or 8.

4.5.3 Quasi-Reversible Kinetics at an Unbiased Substrate

The kinetics of heterogeneous electron transfer at an unbiased substrate affects the tip current and substrate potential. A current approach curve with $\mathrm{Co(phen)_3^{2+}}$ at the unbiased carbon fiber substrate (red solid line in Figure 4-9a) is more negative than that with 1,1'-

ferrocenedimethanol (black solid line). The latter curve fits well with a theoretical curve for a reversible substrate reaction with *b*/*a* = 3.2 and RG = 2.0, where a 10 μm-diameter probe with a small RG was used to obtain a large feedback current. The current approach curve with $Co(phen)_3^{2+}$ fits well with a theoretical curve for a quasi-reversible substrate reaction with the same *b*/*a* and RG values, yielding K = 0.52 with α = 0.5. The theoretical curve does not depend on α substantially because the open circuit potential of the substrate during the tip approach is close to the formal potential (Figure 4-9b). The dimensionless rate constant of 0.13 is equivalent to $k^0 = 3.7 \times 10^{-3}$ cm/s with $a = 5.0$ μm and $D = 3.6 \times 10^{-6}$ cm^2/s for $Co(phen)_3^{2+}$ as determined by chronoamperometry[43] (see eq 10). The kinetic parameters agree with k0 = 4.0 × 10−3 cm/s and α = 0.4 as obtained from a quasi-reversible voltammogram at the carbon fiber substrate (data not shown). This good agreement confirms that a standard rate constant of electron transfer at an unbiased substrate can be determined by SECM when the SECM geometries are such that the substrate potential remains around the formal potential during the tip approach. The standard rate constant is intermediate between 8×10^{-2} cm/s at a laser-activated glassy carbon electrode and 2×10^{-5} cm/s at a highly ordered pyrolytic graphite electrode.[44]

With $Co(phen)_3^{2+}$ as a quasi-reversible mediator, the overpotential at the small substrate is nearly constant during the approach curve measurement ($E - E^{0'} \sim -0.025$ V in Figure 4-9b). Therefore, the electron transfer rate at the unbiased substrate is practically independent of the tip–substrate distance. This situation is similar to that of a biased substrate at a constant potential. Well-developed theory for biased substrates,[25, 35]

(a)

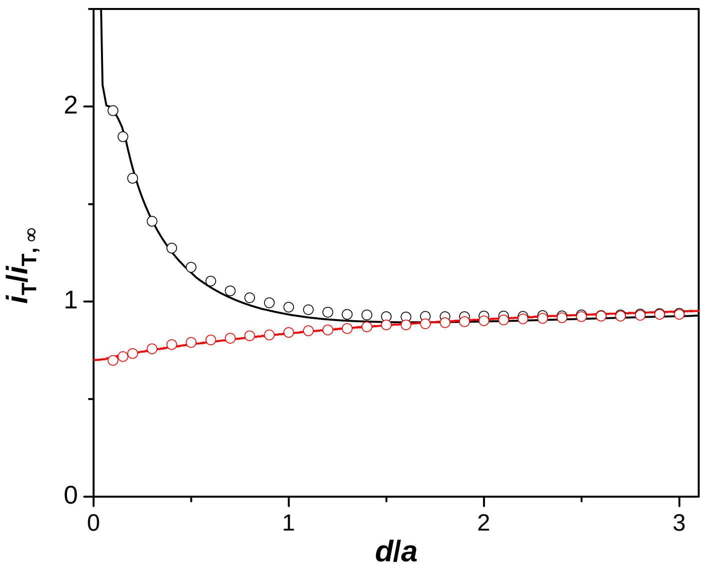

(b)

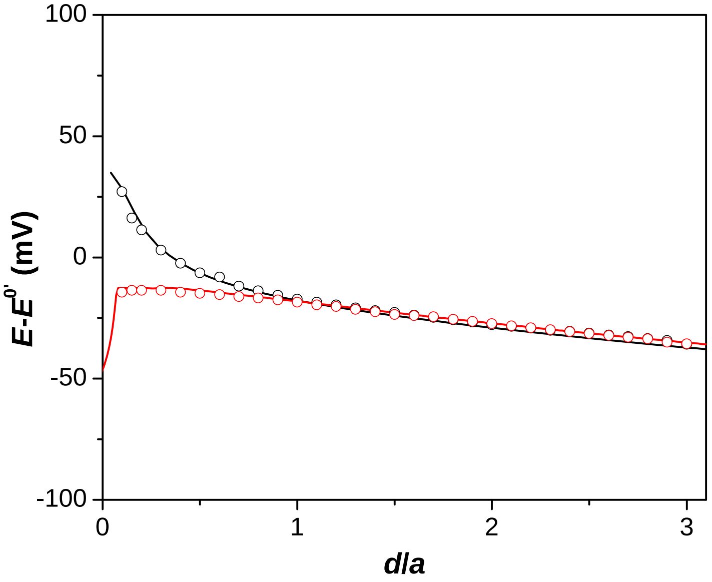

Figure 4-9. (a) Current and (b) potential approach curves with 1 mM 1,1'-ferrocenedimethanol (black) and 2 mM Co(phen)$_3^{2+}$ (red) in 0.1 M KCl with the 34 µm-diameter disk carbon fiber substrate at open circuit potential as obtained using a 10 µm-diameter Pt disk probe with RG = 2.0. The circles and solid lines represent the experimental and theoretical approach curves, respectively. The theory curve for 1,1'-ferrocenedimethanol is based on a reversible substrate reaction. The theory curve for Co(phen)$_3^{2+}$ was obtained for K = 0.52 with α = 0.5. The tip potential: 0.4 and 0.3 V versus Ag/AgCl for 1,1'-ferrocenedimethanol and Co(phen)$_3^{2+}$, respectively. The probe scan rate: 0.6 µm/s.

however, is not applicable to an unbiased substrate, where the feedback current depends on the substrate size and tip outer radius. Furthermore, the negative approach curve for the slow substrate reaction resembles that of a reversible reaction with a small substrate radius and/or a thick insulating sheath of a tip. For a quasi-reversible process at an unbiased substrate, numerical simulations with knowledge of the *b*/*a* and RG values are required for determination of kinetic parameters from a current approach curve.

4.5.4 SECM Imaging

The numerical simulations of line scan above an unbiased disk substrate predict that the tip current is smaller above the center of the substrate than above the edges (Figure 4-6a). Such a current dip was observed in a SECM image of the disk carbon fiber electrode at open circuit potential (Figure 4-10a), where a 10 μm-diameter disk Pt electrode with RG = 8 was scanned at 30 μm/s. The tip current in the image was recorded only when the probe was moved from the left-hand side of the substrate to the right-hand side. Despite the symmetric substrate and tip geometries, the current response in the image is not symmetric with respect to the substrate center. As the probe was scanned across the substrate from the left-hand side to the right-hand side, the tip current was enhanced more above the left edge than above the right edge. Similar asymmetric images were reported previously, where a pair of disk UMEs with the same diameter were used as a tip and an unbiased substrate.[22] In the previous report, the asymmetric line scans with a current dip above the substrate center were ascribed to a transient response because the asymmetry was enhanced as the probe scan rate increased from 5 μm/s to 200 μm/s.

(a)

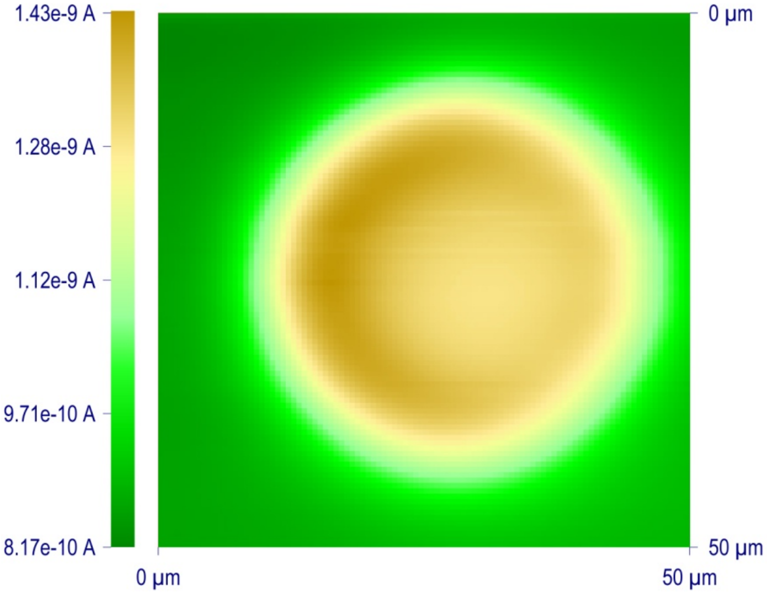

(b)

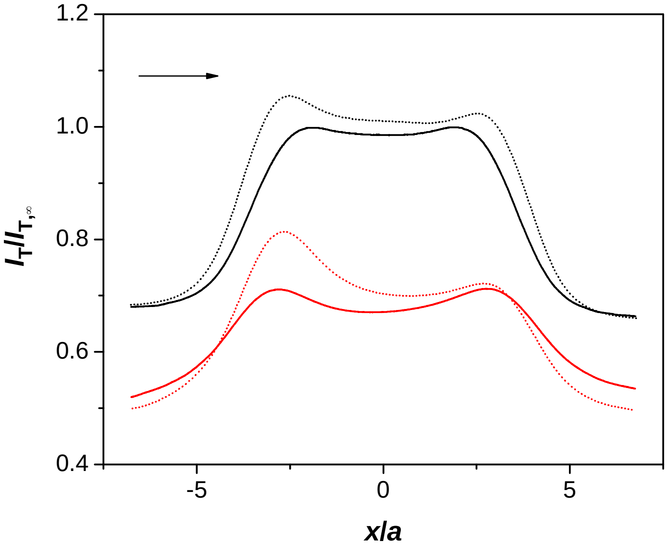

Figure 4-10. (a) SECM images of a ~33 µm-diameter carbon fiber disk electrode at open circuit potential as obtained using a 10 µm-diameter Pt disk probe with RG = 8 with 1 mM 1,1'-ferrocenedimethanol in 0.1 M KCl. The probe scan rate: 30 µm/s. (b) SECM line scans over the unbiased substrate at the scan rate of 0.05 (solid line) and 5 (dotted line) µm/s as obtained using 10 µm-diameter Pt disk probes with RG = 8 (red) and 2 (black). The arrow indicates the scan direction. The tip potential: 0.4 V versus Ag/AgCl. The lateral tip position, *x*, is arbitrary.

As predicted theoretically, however, the current dip above the substrate center was still observed, even at a very slow scan rate of 0.05 μm/s (solid lines in Figure 4-10b). In contrast to the line scan at the rate of 5 μm/s (dotted lines in Figure 4-10b), the symmetric line scan at the slow scan rate confirms the steady state. The larger current response above the substrate edge is due to higher accessibility of the substrate edge to the mediator in the bulk solution when the tip is positioned above the other side of the substrate edge (Figure 4-6b). A current dip above the substrate center is smaller with the 10 μm-diameter probe with RG = 2 (Figure 4-10b). When a probe with smaller RG is positioned above the substrate center, mediator diffusion from the bulk solution to the substrate edge is less hindered by the insulating sheath of the tip.

The current dip is not due to slower mediator generation at the substrate center than at the edge. As the tip is brought to the substrate center at slow scan rates, the approach curves with 1,1'-ferrocenedimethanol fit with theoretical curves for a reversible substrate reaction (Figures 7–9). Importantly, not only the tip but also the substrate must be small enough to achieve a steady state without convection effect at an unbiased substrate. Mediator electrolysis at an unbiased substrate results in a concentration gradient of the mediator from the substrate edge to the bulk solution, where the thickness of the diffusion layer is determined by the substrate size rather than by the tip size.

4.6 CONCLUSIONS

SECM feedback at an unbiased substrate was quantified theoretically for the case of a pair of disk UMEs as the tip and the substrate. At the unbiased substrate, both tip current and substrate potential depend on SECM geometries with respect to the tip radius including the tip–substrate distance, substrate radius, and thickness of the insulating sheath of the tip. A larger feedback effect is obtained using a probe with a thinner insulating sheath, enabling detection of a smaller active spot. The feedback current at an unbiased substrate, however, is much smaller than that at a biased substrate with the same size. Therefore, a probe with a smaller outer diameter[40, 45] will be useful for SECM studies of unbiased conductors.

A slower rate of heterogeneous electron transfer at an unbiased substrate results in a smaller feedback current. This trend is qualitatively similar to that of biased substrates. The SECM theory for biased substrates,[25, 35] however, is not applicable for unbiased substrates, where the feedback effect strongly depends on the SECM geometries. Numerical simulations of an approach curve with the geometrical parameters allow the determination of a standard rate constant of electron transfer at an unbiased substrate when the transfer coefficient is known or when the substrate is small enough that the substrate potential remains close to the formal potential during the tip approach.

The theoretical approach reported here will be useful also for other SECM systems. The substrate radius and tip outer radius would also affect the tip current that is controlled by lateral electron transport through an unbiased substrate with finite conductivity.[10, 20] The theory will be extendable also to SECM feedback based on ion transfer at an externally unbiased interface between two liquid phases.[16, 29, 33]

SUPPORTING INFORMATION

COMSOL Multiphysics Simulation in the Dimensionless Form. The SECM diffusion problem was solved in a dimensionless form using COMSOL Multiphysics. Dimensionless parameters are defined by:

$$R = r/a \tag{S1}$$

$$Z = z/a \tag{S2}$$

$$\mathrm{RG} = r\mathrm{g}/a \tag{S3}$$

$$L = d/a \tag{S4}$$

$$C(R,Z) = c(r,z)/c_0 \tag{S5}$$

$$\tau = 4Dt/a^2 \tag{S6}$$

Steady-state diffusion of O in the solution phase can be expressed in the dimensionless form as

$$\frac{\partial C(R,Z)}{\partial \tau} = 0.25[\frac{\partial^2 C(R,Z)}{\partial R^2} + \frac{1}{R}\frac{\partial C(R,Z)}{\partial R} + \frac{\partial^2 C(R,Z)}{\partial Z^2}] = 0 \tag{S7}$$

The value of 0.25 in eq S7 was used as a dimensionless diffusion coefficient in the simulation. The substrate boundary condition for a reversible reaction is given by

$$E = E^{0'} - \frac{RT}{nF}\ln\frac{1 - C(R,L)}{C(R,L)} \tag{S8}$$

In the simulation, a value of *C(R,L)* was given as the boundary condition. The substrate potential was calculated using eq S8 to obtain a potential approach curve. For a quasi-reversible substrate reaction, the surface boundary condition is given by

$$0.25[\frac{\partial C(R,Z)}{\partial Z}]_{Z=L} = \frac{0.25K(1+\theta)}{\theta^{\alpha}}(\frac{\theta}{\theta+1}) - C(R,L) \qquad \text{(S9)}$$

with

$$\theta = \exp[\frac{F}{RT}(E - E^{0'})] \qquad \text{(S10)}$$

Eq S9 is equivalent to the expression of the flux boundary condition in COMSOL Multiphysics. The other boundary conditions and the initial condition are also given in the dimensionless form. The resulting tip current is obtained in the dimensionless form with respect to the limiting current at a disk probe with infinite RG, yielding

$$I_T = \frac{i_T}{i_{T,\infty}(x=1)} = \frac{\pi}{2\int_0^{b/a} R[\frac{\partial C(R,L)}{\partial Z}]dR} \qquad \text{(S11)}$$

In addition, the substrate current is obtained in the dimensionless form as

$$I_S = \frac{i_S}{i_{T,\infty}(x=1)} = \frac{\pi}{2\int_0^{b/a} R[\frac{\partial C(R,L)}{\partial Z}]dR} \qquad \text{(S12)}$$

An example of the simulation result for a quasi-reversible substrate reaction is attached, where the SECM geometries are defined by L= 0.6, b/a = 9, and RG =10. With K = 0.52 and α = 0.5, a dimensionless substrate potential, θ, of 0.48 was chosen so that $I_S < 0.01$.

RG Effect on Potential Approach Curves. Potential approach curves that correspond to the current approach curves in Figure 4a and b are shown in Figure S 4-1 a and b, respectively.

Effect of Transfer Coefficient on Approach Curves with a Large Substrate. Current and potential approach curves with a large substrate (b/a =30) were calculated to examine their α

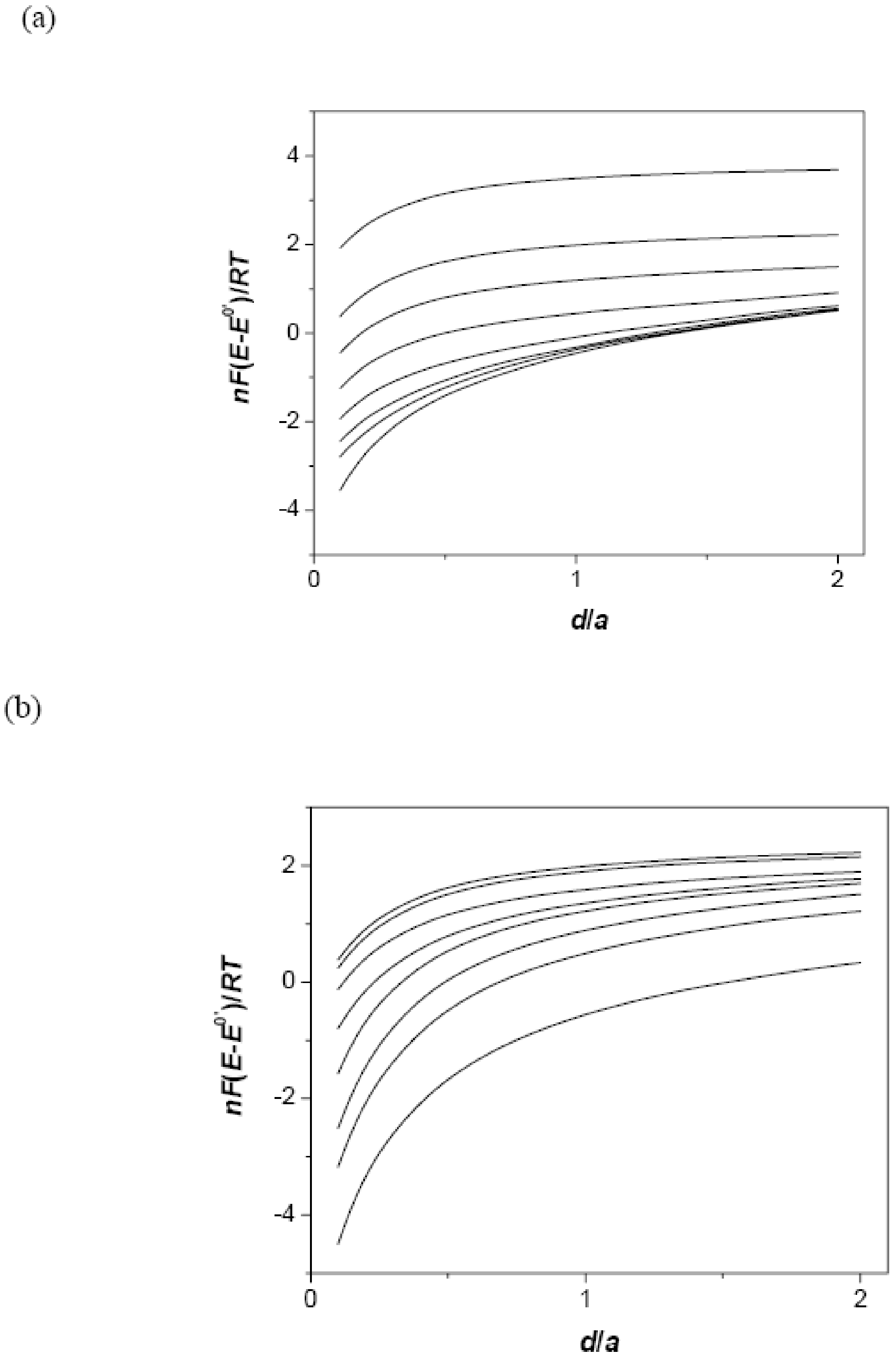

Figure S 4-1. Simulated potential approach curves with (a) *b*/*a* = 10 and RG = 1.1, 6, 9, 10, 10.5, 12, 15, 50 from the top, and (b) RG = 1.1 and *b*/*a* = 30, 10, 5, 2.5, 1.5, 1.2, 1.1, and 1.0 from the top.

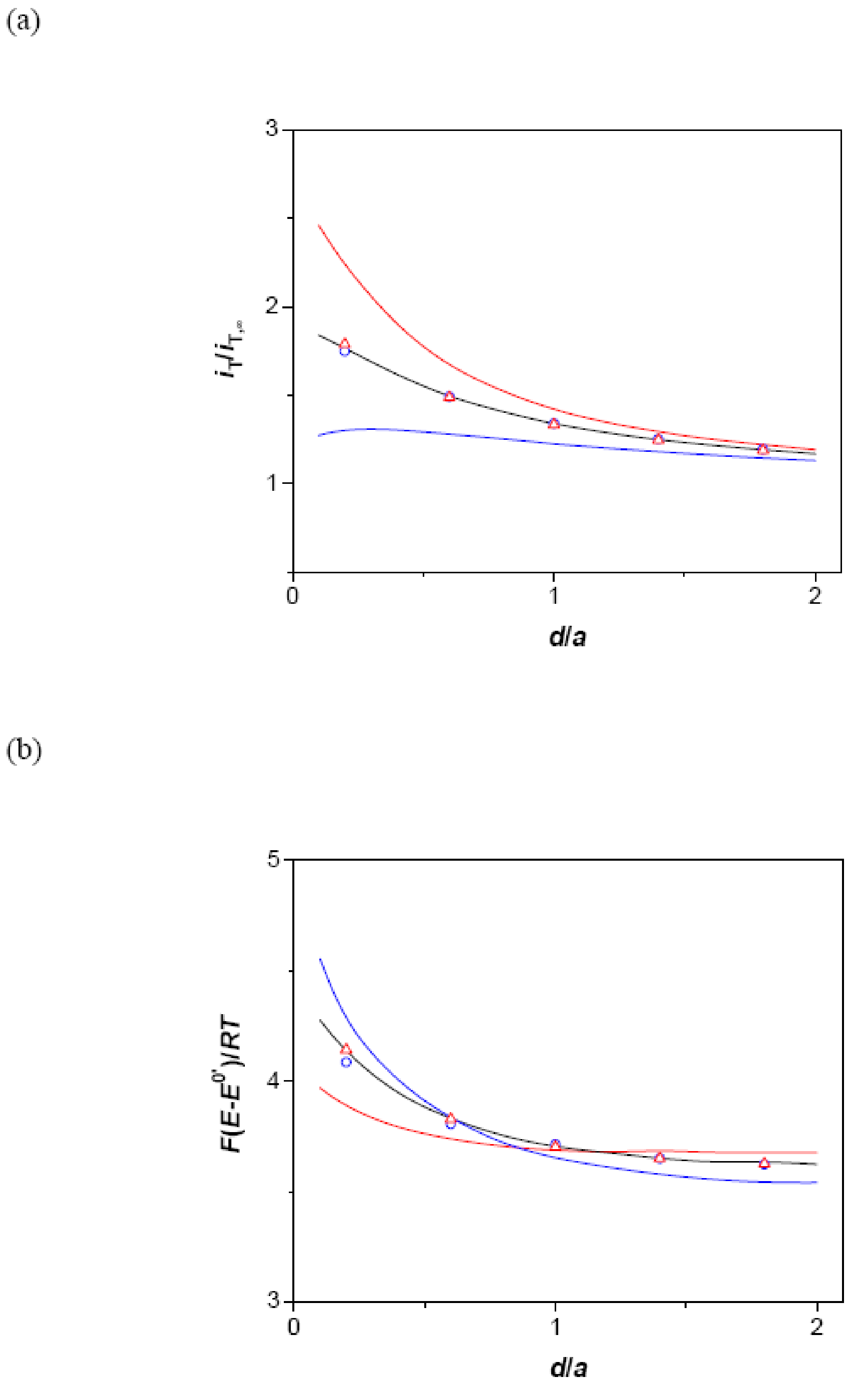

Figure S 4-2. Effect of the transfer coefficient on (a) current and (b) potential approach curves with an unbiased disk substrate with b/a = 30 as simulated for a disk UME probe with RG = 10. The blue, black, and red lines represent theoretical curves for K = 0.1 with α = 0.7, 0.5, and 0.3, respectively. The blue and red open circles represent theoretical curves with (K, α) = (0.7, 0.2) and (0.3, 0.05), respectively.

blue, black, and red lines represent theoretical curves for K = 0.1 with α = 0.7, 0.5, and 0.3, respectively. The blue and red open circles represent theoretical curves with (K, α) = (0.7, 0.2) and (0.3, 0.05), respectively.

dependence. With a given *K*, larger feedback current results from a smaller α (Figure S 4-2a), while the overpotential is smaller with a smaller α at short tip-substrate distances (Figure S 4-2b). Different sets of *K* and α give almost identical theoretical approach curves for both tip current and substrate potential so that both parameters can not be determined simultaneously from a single approach curve.

Kinetically Limited Approach Curves with a Small Substrate. Effects of *K* and *α* on current and potential approach curves were investigated theoretically with a small substrate ($b/a = 9$). The current response is kinetically limited for a substrate reaction with $K < 10$ and becomes smaller as *K* decreases (Figure S 4-3a). Pure negative feedback is obtained for $K < 2.5 \times 10^{-4}$. The overpotential at the small substrate, however, is so negative (Figure 4-7b) that either tip current or substrate potential is not sensitive to α (compare the red and blue lines for α = 0.3 and 0.7,respectively, in Figure S 4-3a and b).

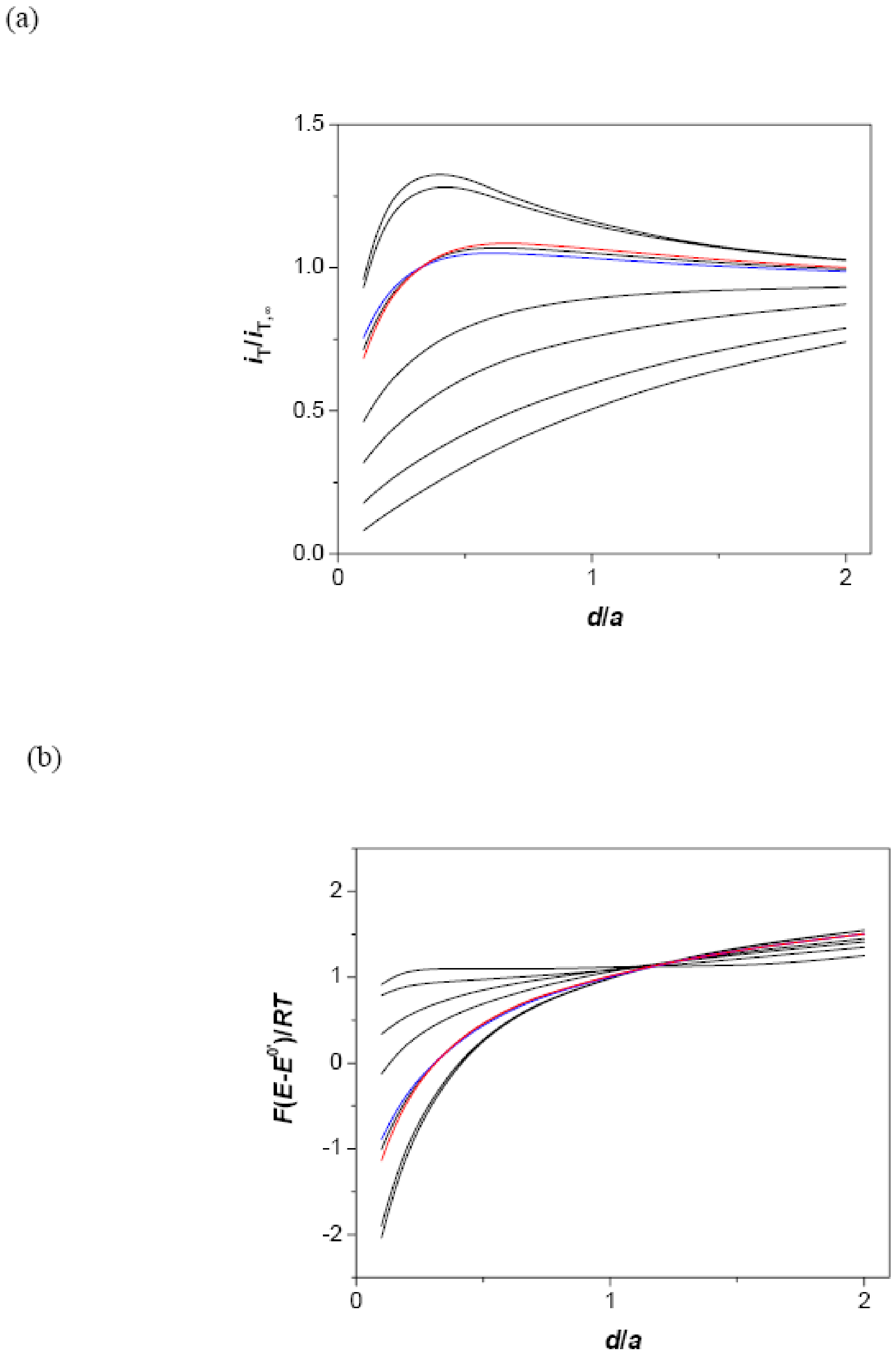

Figure S 4-3. Effect of the intrinsic rate of the substrate reaction on (a) current and (b) potential approach curves with an unbiased disk substrate with $b/a = 9$ as simulated for a disk UME probe with RG = 10. The black lines are for $K = 10$, 1, 0.25, 0.1, 0.05, 0.025, 0.01, 0.0025, and 0.00025 from (a) the top and (b) the bottom. The blue and red lines represent theoretical curves for $K = 0.1$ with $\alpha = 0.7$ and 0.3, respectively.

COMSOL Model Report

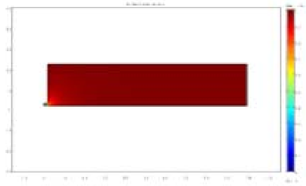

1. Table of Contents

2. Model Properties

Property	Value
Model name	
Author	
Company	
Department	
Reference	
URL	
Saved date	Sep 2, 2006 12:56:04 PM
Creation date	Oct 8, 2005 3:38:43 PM
COMSOL version	COMSOL 3.2.0.304

File name: /home/sim/claire/c fiber/ba34 rg2/K=0.52/alpha=0.5/1.fl

Application modes and modules used in this model:

- Geom1 (Axial symmetry (2D))
    - Diffusion (Chemical Engineering Module)

3. Constants

Name	Expression	Value	Description

theta	0.48	0.48	
alpha	0.5	0.5	
K	0.52	0.52	

4. Geometry

Number of geometries: 1

4.1. Geom1

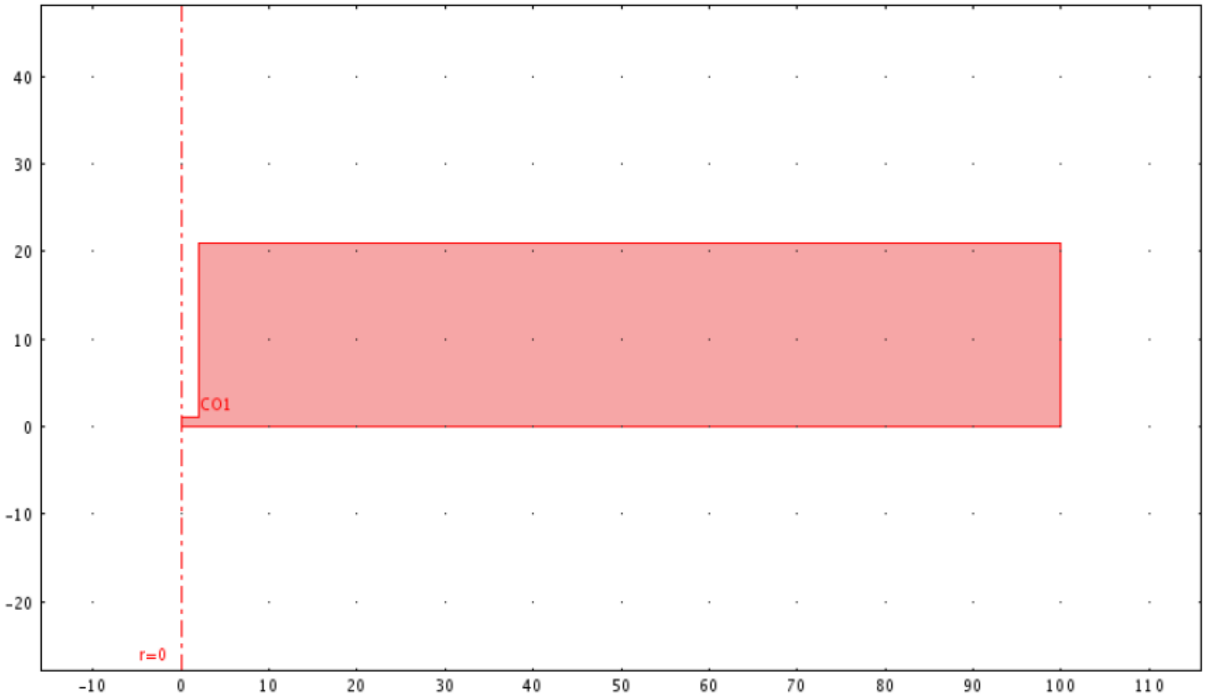

4.1.1. Point mode

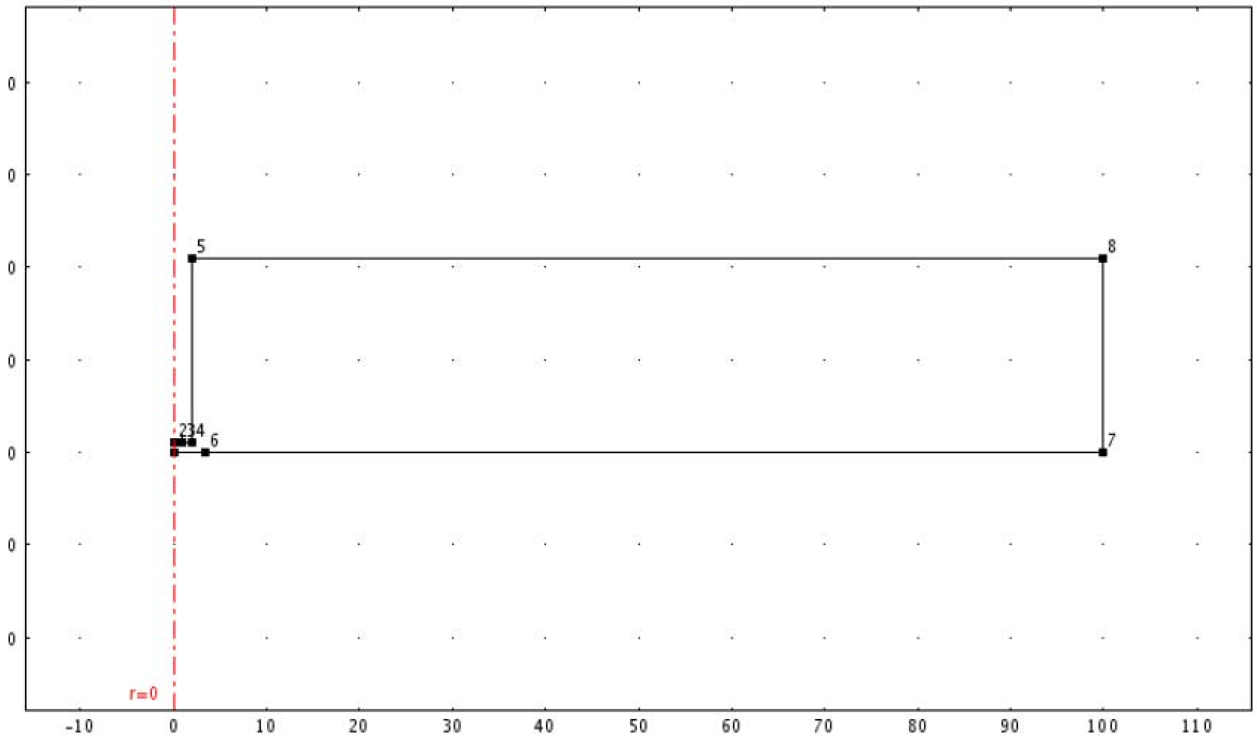

.2. Boundary mode

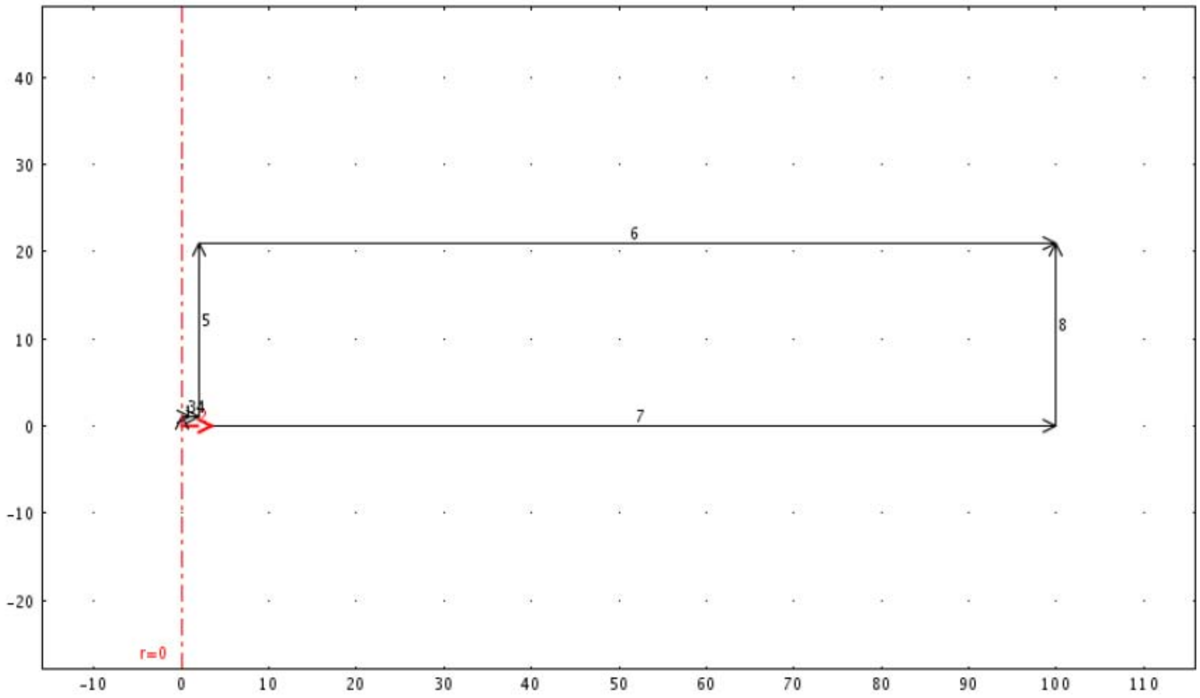

4.1.3. Subdomain mode

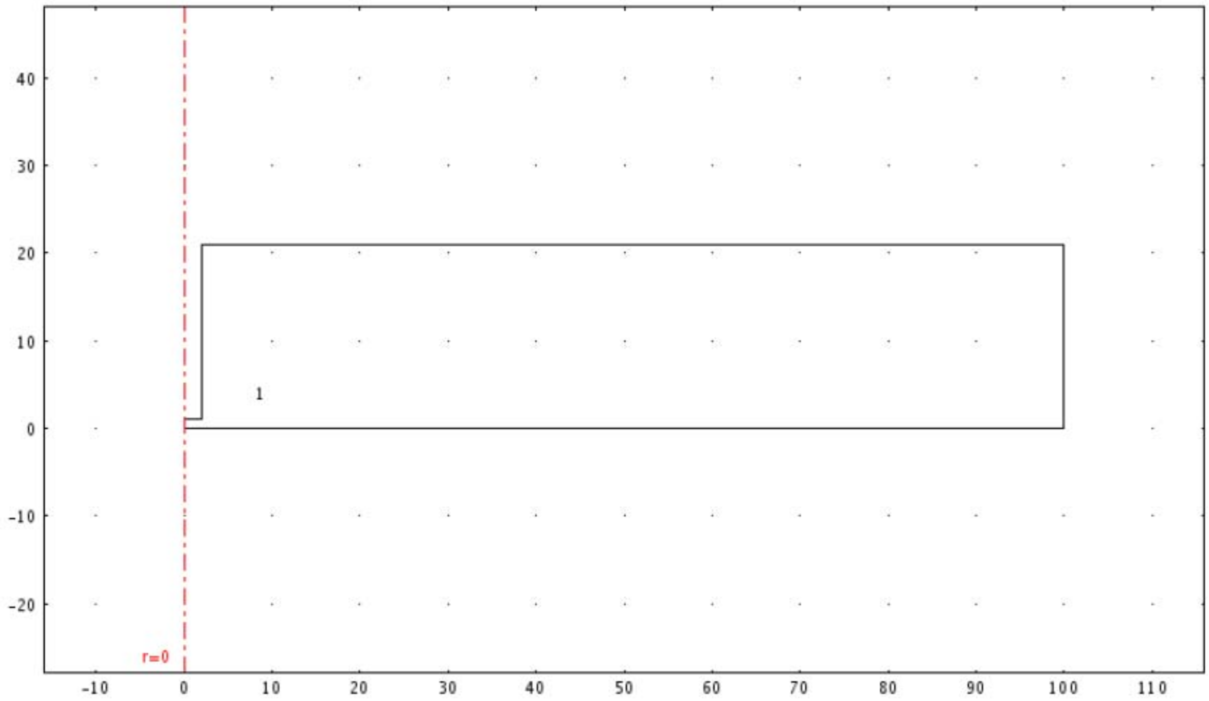

5. Geom1

Space dimensions: Axial symmetry (2D)

Independent variables: r, phi, z

5.1. Mesh

5.1.1. Mesh Parameters

Parameter	Value
Maximum element size	
Maximum element size scaling factor	1
Element growth rate	1.3
Mesh curvature factor	0.3
Mesh curvature cut off	0.001
Resolution of narrow regions	1
Resolution of geometry	10
x-direction scale factor	1.0
y-direction scale factor	1.0

Mesh geometry to level	Subdomain
Optimize quality	On

Subdomain	1
Maximum element size	
Element growth rate	

Boundary	2-3	1, 4-8
Maximum element size	0.01	
Element growth rate		
Mesh curvature factor		
Mesh curvature cut off		

Point	3, 6	1-2, 4-5, 7-8
Maximum element size	0.001	
Element growth rate		

5.1.2. Mesh Statistics

Number of degrees of freedom	63191
Number of boundary elements	1278
Number of elements	30956
Minimum element quality	0.7035

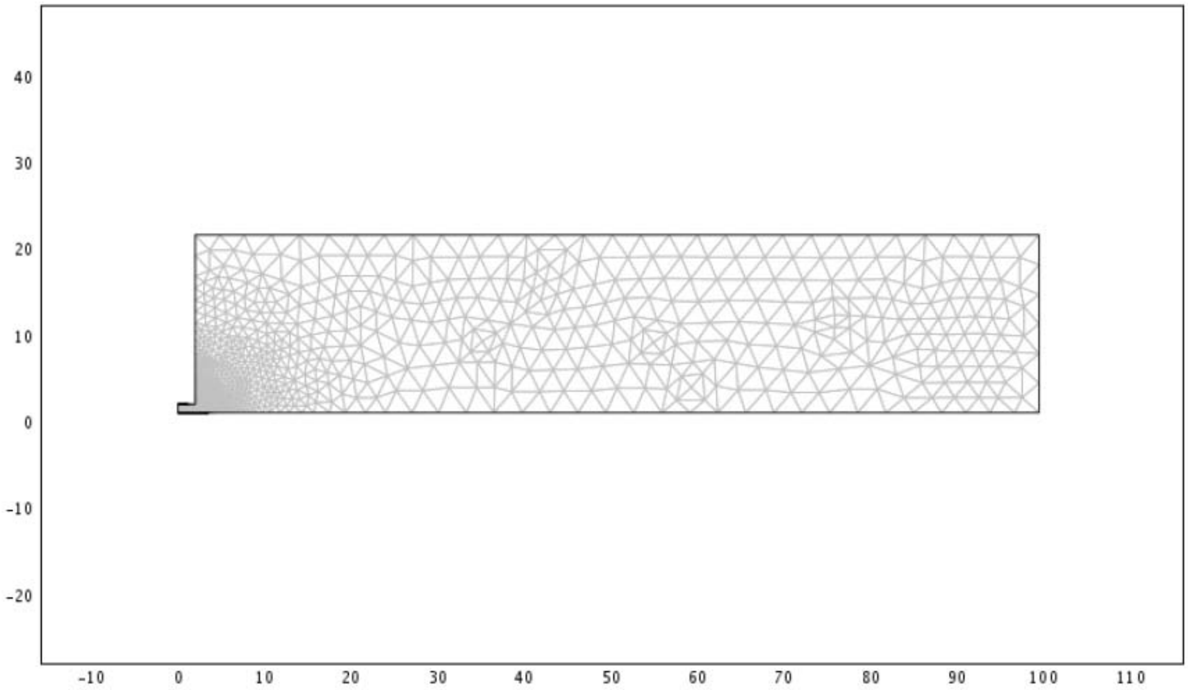

5.2. Application Mode: Diffusion (di)

Application mode type: Diffusion (Chemical Engineering Module)

Application mode name: di

5.2.1. Application Mode Properties

Property	Value
Default element type	Lagrange - Quadratic
Analysis type	Transient
Equilibrium assumption	Off
Frame	Frame (rz)
Weak constraints	Off

5.2.2. Variables

Dependent variables: c

Shape functions: shlag(2,'c')

Interior boundaries not active

5.2.3. Boundary Settings

Boundary		1, 4-5	2
Type		Insulation/Symmetry	Flux
Mass transfer coefficient (kc)		0	**0.25*K*(1+theta)/(theta^alpha)**
Bulk concentration (cb)		0	**1/(1+theta)**
Concentration (c0)		0	**0.135**

Boundary	3	6, 8	7
Type	Concentration	Concentration	Insulation/Symmetry
Mass transfer coefficient (kc)	0	0	0
Bulk concentration (cb)	0	0	0
Concentration (c0)	0	**1**	**1**

5.2.4. Subdomain Settings

Subdomain		1
Diffusion coefficient (D)		**0.25**

Subdomain initial value		1
Concentration, c (c)		1

6. Solver Settings

Solve using a script: off

Analysis type	Transient
Auto select solver	On
Solver	Stationary nonlinear
Solution form	General
Symmetric	Off
Adaption	Off

6.1. Direct (UMFPACK)

Solver type: Linear system solver

Parameter	**Value**
Pivot threshold	0.1
Memory allocation factor	0.7

6.2. Nonlinear

Parameter	**Value**
Relative tolerance	1.0E-6
Maximum number of iterations	25
Manual tuning of damping parameters	Off

Highly nonlinear problem	Off
Initial damping factor	1.0
Minimum damping factor	1.0E-4
Restriction for step size update	10.0

6.3. Advanced

Parameter	**Value**
Constraint handling method	Elimination
Null-space function	Automatic
Assembly block size	5000
Use Hermitian transpose of constraint matrix	On
Use complex functions with real input	Off
Stop if error due to undefined operation	On
Type of scaling	Automatic
Manual scaling	
Row equilibration	On
Manual control of reassembly	Off
Load constant	On
Constraint constant	On
Mass constant	On
Damping (mass) constant	On
Jacobian constant	On
Constraint Jacobian constant	On

7. Postprocessing

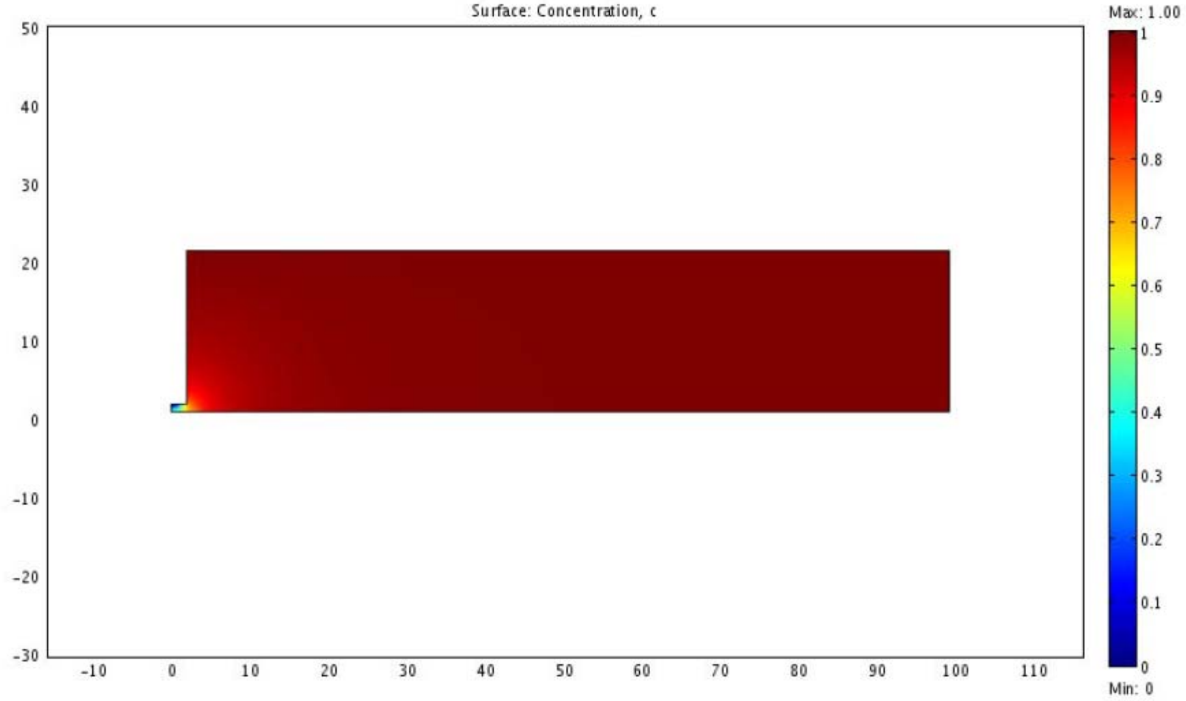

8. Variables

8.1. Boundary

Name	Description	Expression
ndflux_c_di	Normal diffusive flux, c	nr_di * dflux_c_r_di+nz_di * dflux_c_z_di

8.2. Subdomain

Name	Description	Expression
grad_c_r_di	Concentration gradient, c, r component	cr
dflux_c_r_di	Diffusive flux, c, r component	-(Drr_c_di * cr+Drz_c_di * cz)
grad_c_z_di	Concentration gradient, c, z component	cz
dflux_c_z_di	Diffusive flux, c, z component	-(Dzr_c_di * cr+Dzz_c_di * cz)
grad_c_di	Concentration gradient, c	sqrt(grad_c_r_di^2+grad_c_z_di^2)
dflux_c_di	Diffusive flux, c	sqrt(dflux_c_r_di^2+dflux_c_z_di^2)

ACKNOWLEDGEMENTS

We thank the National Science Foundation (DBI0242561) and the National Institute of Health (GM073439) for their financial support. This work was also supported by the University of Pittsburgh. We appreciate the assistance of Darrick A. Gross for his preliminary studies. The authors thank Gregg P. Kotchey for his comments on the manuscript.

REFERENCES

(1) Bard, A. J.; Mirkin, M. V., Eds. *Scanning Electrochemical Microscopy*; Marcel Dekker: New York, 2001.

(2) Barker, A. L.; Gonsalves, M.; Macpherson, J. V.; Slevin, C. J.; Unwin, P. R. *Anal. Chim. Acta* **1999**, *385*, 223–240.

(3) Amemiya, S.; Guo, J.; Xiong, H.; Gross, D. A. *Anal. Bioanal. Chem.* **2006**, *386*, 458–471.

(4) Bard, A. J.; Fan, F.-R. F.; Kwak, J.; Lev, O. *Anal. Chem.* **1989**, *61*, 132–138.

(5) Bard, A. J.; Zoski, C. G. *Anal. Chem.* **2000**, *72*, 346A–352A.

(6) Quinn, B. M.; Prieto, I.; Haram, S. K.; Bard, A. J. *J. Phys. Chem. B* **2001**, 7474–7476.

(7) Wang, J.; Song, F.; Zhou, F. *Langmuir* **2002**, *18*, 6653–6658.

(8) Liljeroth, P.; Quinn, B. M.; Ruiz, V.; Kontturi, K. *Chem. Commun.* **2003**, 1570–1571.

(9) Ruiz, V.; Liljeroth, P.; Quinn, B. M.; Kontturi, K. *Nano Letters* **2003**, *3*, 1459–1462.

(10) Liljeroth, P.; Vanmaekelbergh, D.; Ruiz, V.; Kontturi, K.; Jiang, H.; Kauppinen, E.; Quinn, B. M. *J. Am. Chem. Soc.* **2004**, *126*, 7126–7132.

(11) Fernandez, J. L.; Hurth, C.; Bard, A. J. *J. Phy. Chem. B* **2005**, *109*, 9532–9539.

(12) Ruiz, V.; Nicholson, P. G.; Jollands, S.; Thomas, P. A.; Macpherson, J. V.; Unwin, P. R. *J. Phys. Chem. B* **2005**, *109*, 19335–19344.

(13) Liljeroth, P.; Quinn, B. M. *J. Am. Chem. Soc.* **2006**, *128*, 4922–4923.

(14) Wilson, N. R.; Guille, M.; Dumitrescu, I.; Fernandez, V. R.; Rudd, N. C.; Williams, C. G.; Unwin, P. R.; Macpherson, J. V. *Anal. Chem.* **2006**, 7006–7015.

(15) Xiong, H.; Gross, D. A.; Guo, J.; Amemiya, S. *Anal. Chem.* **2006**, *78*, 1946–1957.

(16) Guo, J.; Amemiya, S. *Anal. Chem.* **2005**, *77*, 2147–2156.

(17) Mandler, D.; Unwin, P. R. *J. Phys. Chem. B* **2003**, *107*, 407–410.

(18) Zhang, J.; Barker, A. L.; Mandler, D.; Unwin, P. R. *J. Am. Chem. Soc.* **2003**, *125*, 9312–9313.

(19) O'Mullane, A. P.; Macpherson, J. V.; Unwin, P. R.; Cervera-Montesinos, J.; Manzanares, J. A.; Frehill, F.; Vos, J. G. *J. Phys. Chem. B* **2004**, *108*, 7219–7227.

(20) Whitworth, A. L.; Mandler, D.; Unwin, P. R. *Phys. Chem. Chem. Phys.* **2005**, *7*, 356–365.

(21) Wipf, D. O.; Bard, A. J. *J. Electrochem. Soc.* **1991**, *138*, 469–474.

(22) Macpherson, J.; Slevin, C. J.; Unwin, P. R. *J. Chem. Soc., Faraday Trans.* **1996**, *92*, 3799–3805.

(23) Selzer, Y.; Turyan, I.; Mandler, D. *J. Phys. Chem. B* **1999**, *103*, 1509–1517.

(24) Zoski, C. G.; Simjee, N.; Guenat, O.; Koudelka-Hep, M. *Anal. Chem.* **2004**, *76*, 62–72.

(25) Wei, C.; Bard, A. J.; Mirkin, M. V. *J. Phys. Chem.* **1995**, *99*, 16033–16042.

(26) O'Mullane, A. P.; Neufeld, A. K.; Bond, A. M. *Anal. Chem.* **2005**, *77*, 5447–5452.

(27) Ghilane, J.; Hauquier, F.; Fabre, B.; Hapiot, P. *Anal. Chem.* **2006**, *78*, 6019–6025.

(28) Peterson, R. R.; Cliffel, D. E. *Langmuir*, **2006**, *22*, 10307–10314.

(29) Shao, Y.; Mirkin, M. V. *J. Phys. Chem. B* **1998**, *102*, 9915–9921.

(30) Zoski, C. G.; Mirkin, M. V. *Anal. Chem.* **2002**, *74*, 1986–1992.

(31) Bard, A. J.; Faulkner, L. R. In *Electrochemical Methods: Fundamentals and Applications,* 2nd ed.; John Wiley & Sons: New York, 2001, pp 94–96.

(32) Bard, A. J.; Mirkin, M. V.; Unwin, P. R.; Wipf, D. O. *J. Phys. Chem.* **1992**, *96*, 1861–1868.

(33) Selzer, Y.; Mandler, D. *J. Phys. Chem. B* **2000**, *104*, 4903–4910.

(34) Kwak, J.; Bard, A. J. *Anal. Chem.* **1989**, *61*, 1221–1227.

(35) Bard, A. J.; Mirkin, M. V.; Unwin, P. R.; Wipf, D. O. *J. Phys. Chem.* **1992**, *96*, 1861–1868.

(36) Chen, Y.-W. D.; Santhanam, K. S. V.; Bard, A. J. *J. Electrochem. Soc.* **1982**, *129*, 61–66.

(37) Wightman, R. M.; Wipf, D. O. In *Electroanalytical Chemistry*; Bard, A. J., Ed.; Marcel Dekker: New York, 1989; Vol. 15, pp 267–351.

(38) Fan, F.-R. F. In *Scanning Electrochemical Microscopy*; Bard, A. J., Mirkin, M. V., Eds.; Marcel Dekker: New York, 2001, pp 111–143.

(39) Amemiya, S.; Bard, A. J. *Anal. Chem.* **2000**, *72*, 4940–4948.

(40) Xiong, H.; Guo, J. D.; Kurihara, K.; Amemiya, S. *Electrochem. Commun.* **2004**, *6*, 615–620.

(41) Bourdillon, C.; Demaille, C.; Moiroux, J.; Saveant, J. M. *J. Am. Chem. Soc.* **1995**, *117*, 11499–11506.

(42) Amphlett, J. L.; Denuault, G. *J. Phys. Chem. B* **1998**, *102*, 9946–9951.

(43) Denuault, G.; Mirkin, M. V.; Bard, A. J. *J. Electroanal. Chem.* **1991**, *308*, 27–38.

(44) Cline, K. K.; McDermott, M. T.; McCreery, R. L. *J. Phys. Chem.* **1994**, *98*, 5314–5319.

(45) Liu, B.; Rolland, J. P.; DeSimone, J. M.; Bard, A. J. *Anal. Chem.* **2005**, *77*, 3013–3017.

5.0 PROBING HETEROGENEOUS ELECTRON TRANSFER AT INDIVIDUAL ONE-DIMENSIONAL NANOSTRUCTURES BY SCANNING ELECTROCHEMICAL MICROSCOPY: FROM GOLD NANOBAND TO SINGLE-WALLED CARBON NANOTUBE

5.1 HETEROGENEOUS ELECTRON TRANSFER KINETICS AT SINGLE ONE-DIMENSIONAL GOLD NANOBANDS AS PROBED BY SECM

We describe an approach to the determination of heterogeneous electron transfer (ET) kinetics at a single one-dimensional (1D) nanostructure by scanning electrochemical microscopy (SECM). The 1D nanostructure is an anisotropic material, such as a wire, tube, and band with the width of 1 to 100 nm and the length of micrometers to centimeters.[1, 2] The nanomaterials composed of a noble metal, semiconductor, and organic material have been tailor-made for a variety of potential applications. Conductive and semiconducting 1D nanostructures are attractive electrode materials for molecular electronics,[3] sensors,[4, 5] catalysis,[6] and energy conversion/storage.[7] A high-aspect-ratio nanoelectrode is useful for studies of mass transport at a nanometer scale[8] and fast heterogeneous ET kinetics.[9] An ET rate at a single-walled carbon nanotube was predicted to depend on the tube diameter.[10] In contrast to an ensemble, however, electrochemical measurement at a single nanostructure level by standard techniques requires tedious nanoprocessing for integration of the nanomaterial into an electrode format.[9]

Recently, we reported non-contact and spatially-resolved measurement of an ET process at a 1D nanostructure by SECM.[11] With this approach, redox mediator molecules, O, are electrolyzed at the tip of a disk-shaped ultramicroelectrode probe positioned near a 1D nanostructure (Figure 5-1). The tip-generated species, R, react locally at the nanostructure surface directly under the tip so that regenerated mediators are detected at the tip to enhance an amperometric tip response. Current amplification based on the local feedback effect enables the detection of a 1D nanostructure with the nanometer dimension that is much smaller than a probe diameter. Steady-state electron transport between the nanoelectrode and the bulk solution is mediated directly at the exterior electrode/solution interface, eliminating a need of an external circuit connected to the nanoelectrode. Application of the SECM method, however, was demonstrated only with a traditional nanoband electrode[12] as a geometrical model, which is much longer than a probe diameter so that the mediator regeneration is diffusion-limited.[11]

Here we apply the novel SECM approach to probe heterogeneous ET kinetics at a single 1D nanostructure with a micrometer length. An Au nanoband with 100 nm width, 50 μm length, and 50 nm thickness was prepared on a SiO_2-covered Si wafer by electron beam lithography (Figure 5-2a; see Supporting Information). The Au nanoband was immersed in 0.1 M KCl containing 1 mM $Ru(NH_3)_6^{3+}$ as a redox mediator and was detected by rastering a 2.2 μm-diameter Pt disk probe at a constant height of ~1.6 μm from the substrate (Figure 5-2b). The tip current increased as the tip was brought laterally from above the SiO_2 surface to above the nanoband, indicating that $Ru(NH_3)_6^{2+}$ generated at the tip was oxidized at the nanoband surface to enhance the tip

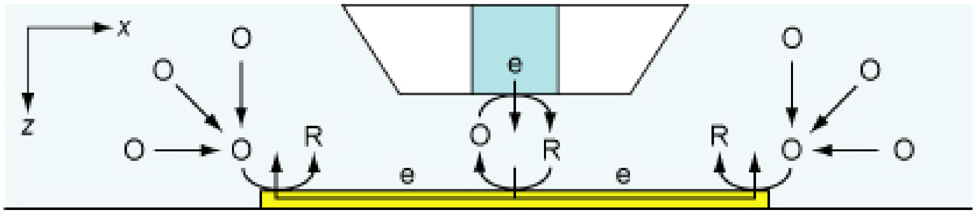

Figure 5-1. A side view of an SECM feedback experiment with a disk ultramicroelectrode probe positioned above a 1D nanostructure.

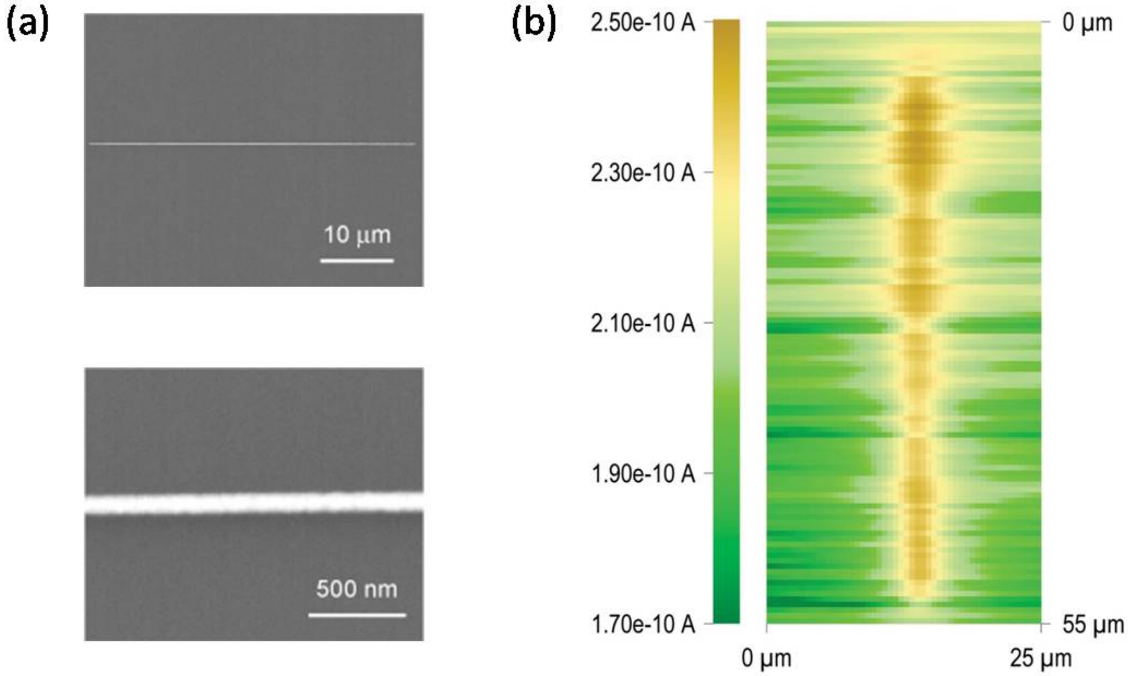

Figure 5-2. (a) Scanning electron microscopy and (b) SECM Images of an Au band with 100 nm width and 50 µm length.

current. The band length in the image agrees with 50 μm. The nanoband is apparently wider than 100 nm, because the spatial resolution of the image is determined by the tip size. Nevertheless, the tip center can be positioned directly above the band, where the tip current reaches the maximum value.

To obtain more quantitative information on the surface reactivity, the tip current, i_T, was measured as a function of the tip–substrate distance, d, using a 2.0 μm-diameter Pt disk probe. The resulting current approach curve was plotted in the normalized form for theoretical analysis (Figure 5-3a). When the tip is positioned in a bulk solution, a steady-state diffusion-limited current, $i_{T,\infty}$, is obtained as

$$i_{T,\infty} = 4nFDca \tag{1}$$

where n is the number of electrons transferred per redox molecule, F is the Faraday constant, D and c are the diffusion coefficient and concentration of the redox mediator in the bulk solution, and a is the radius of the disk tip. The tip current decreased monotonically toward zero as the tip was brought to the SiO_2 surface. The normalized approach curve fits with a theoretical one for an insulator, where

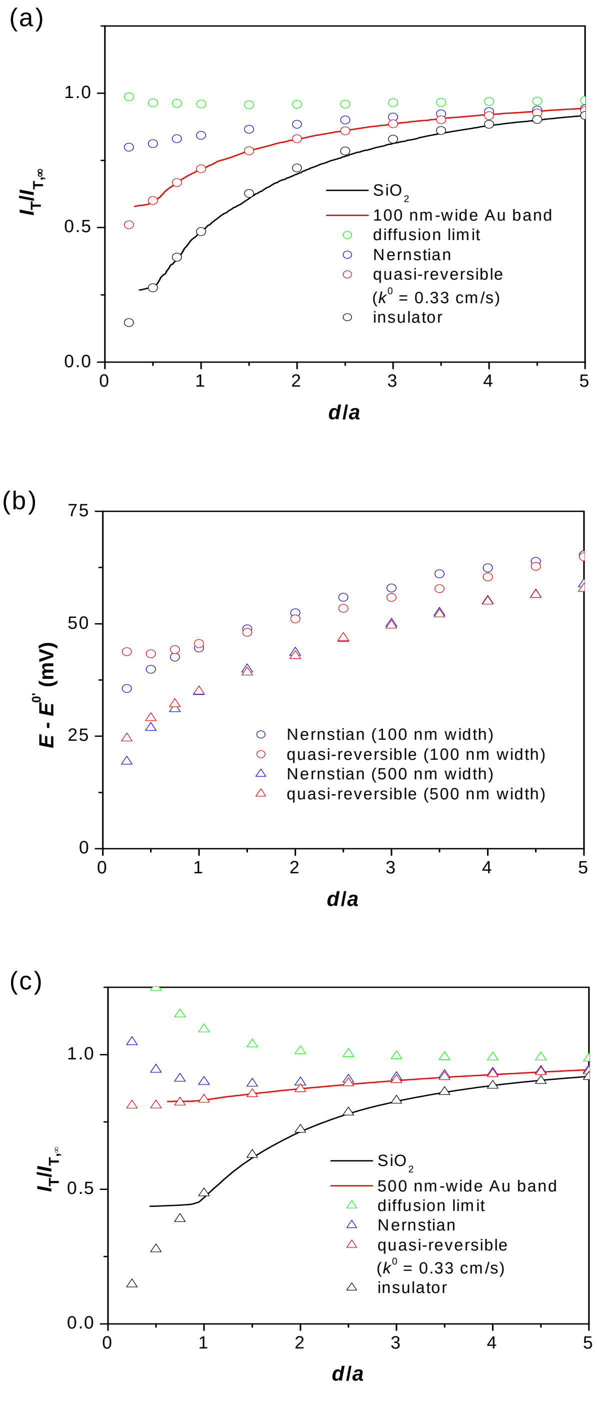

Figure 5-3. (a) Current and (b) potential approach curves with a 100 nm-wide Au band. Current and potential data with a 500 nm-wide Au band are presented in (c) and (b), respectively. The lines and circles represent experimental and theoretical curves, respectively.

diffusion of mediator molecules to the tip is hindered by the inert substrate. The tip current also decreased monotonically as the tip center was brought to the band center, because more than 90 % of the surface area directly under the tip is insulating. The tip current at the nanoband, however, is larger than that at the SiO_2 surface, confirming mediator regeneration.

The approach curve at the nanoband was analyzed to quantify the surface redox reactivity. Three-dimensional SECM diffusion problems were solved numerically using COMSOL Multiphysics® (see Supporting Information). The ET reaction at the nanoband surface was assumed to be purely diffusion limited, Nernstian, or quasi-reversible (Figure 5-3a). In Nernstian and quasi-reversible cases, an open circuit potential of the unbiased nanoband, E, was chosen such that the net current flow across the nanoband/solution interface is zero, yielding theoretical potential approach curves (Figure 5-3b).[13] The experimental current response fits with a theoretical one for a quasi-reversible reaction with a standard rate constant, k^0, of 0.33 cm/s and a transfer coefficient, α, of 0.5. A theoretical current response strongly depends on k^0 but not on α, because an open circuit potential of the nanoband during the tip approach is close to the formal potential, $E^{0'}$. The same k^0 value gives a good fit for an approach curve obtained with a higher mediator concentration (see Supporting Information), confirming that the lateral electronic conduction in the nanoband is not a rate-determining step.[14] The k^0 value determined with 0.1 M KCl is smaller than that of the same redox couple at an Au electrode in 0.1 M $HClO_4$ (k^0 = 1.43 cm/s),[15] where Cl^- adsorbs more specifically than ClO_4^-.[16]

A current approach curve was measured also with a 500 nm-wide Au band (50 μm long and 50 nm thick) using a 2.8 μm-diameter probe (Figure 5-3c), yielding the same k^0 value as determined with the 100 nm-wide band. The current approach curve with the wider nanoband is closer to the corresponding Nernstian curve, which indicates that, despite the similar probe size, mass transfer at the wider band is slower. In fact, a mass transfer coefficient at a nanoband in such SECM configuration was predicted to be inversely proportional to the band width rather than to the tip size or tip–substrate distance.[11] The open circuit potential of a nanoband mainly depends on the band length, which determines an effective length of the band surface exposed to the bulk solution for mediator electrolysis. Thus, the open circuit potentials of the 100 and 500 nm-wide bands with the same length are comparable. The potentials are not positive enough to drive the mediator regeneration to the diffusion limit.

In summary, we demonstrated that a single 1D nanostructure as prepared on an insulator can be detected by SECM on the basis of surface redox activity under solution. The heterogeneous ET kinetics at the 1D nanostructure without external control of the potential can be determined from the tip current by theoretical analysis with three-dimensional numerical simulations.

5.2 ELECTROCHEMICAL IMAGING OF AN INDIVIDUAL SINGLE-WALLED CARBON NANOTUBE BY SECM

Single-walled carbon nanotube (SWNT) has attracted much interest as electrode materials.[14, 17-19] SWNTs are formed from a graphene sheet rolled up seamlessly, which are hollow cylinders of 1-2 nm diameter.[20, 21] Depending on the chirality and tube diameter, SWNTs can be metals, semiconductors or small band gap semiconductors.[22, 23] It has been revealed that metallic and semiconducting SWNT exist in all materials synthesized by different methods (e.g., chemical vapor deposition, laser ablation, arc-discharge),[23] typically one third of which exhibit metallic property. Therefore, the structure-dependent properties can not be determined by studying ensembles of SWNTs.

Here we apply SECM to probe electron transfer at an individual pristine carbon nanotube with ~1 nm in diameter and ≥ 1 mm in length (Figure 5-4). The ultralong SWCNT was grown on a SiO_2-coated Si substrate by chemical vapor deposition.[24] The Si/SiO_2 substrate covered by aligned SWNTs was immersed in an aqueous solution containing 1 mM $Ru(NH_3)_6Cl_3$ as a redox mediator and 0.1 M KCl as the supporting electrolyte. An SECM image of an individual SWNT was obtained by rastering a 2 μm-diameter Pt tip at a constant height of ~ 1.8 μm from the substrate (Figure 5-5), where the horizontal bright band in the SECM image represents the individual SWNT. The potential applied at the Pt tip was -0.4 V versus a homemade Ag/AgCl reference electrode such that the reduction of $Ru(NH_3)_6^{3+}$ at the tip is diffusion-controlled. The tip current increased as the tip was scanned laterally from above the SiO_2 surface to above the

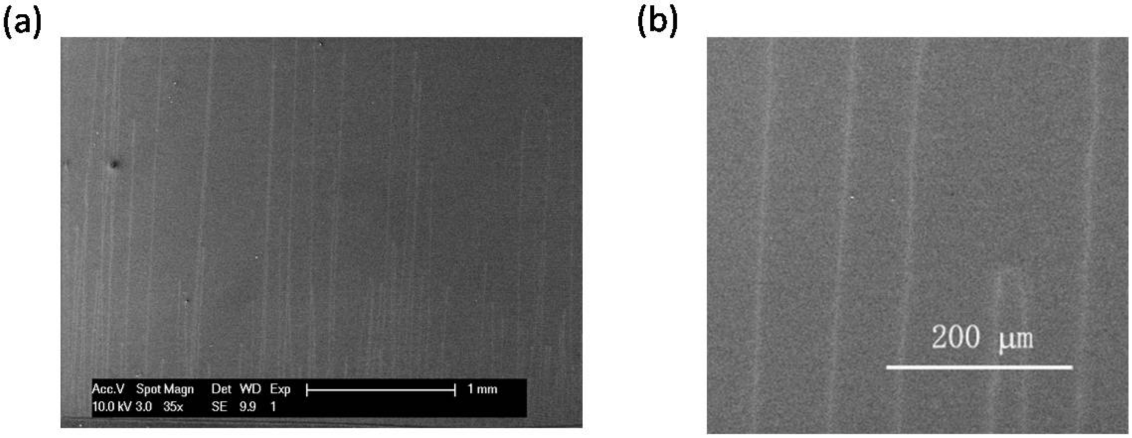

Figure 5-4. SEM images of (a) an oriented array of SWNTs grown on a Si/SiO_2 substrate and (b) SWNTs at a higher magnification.

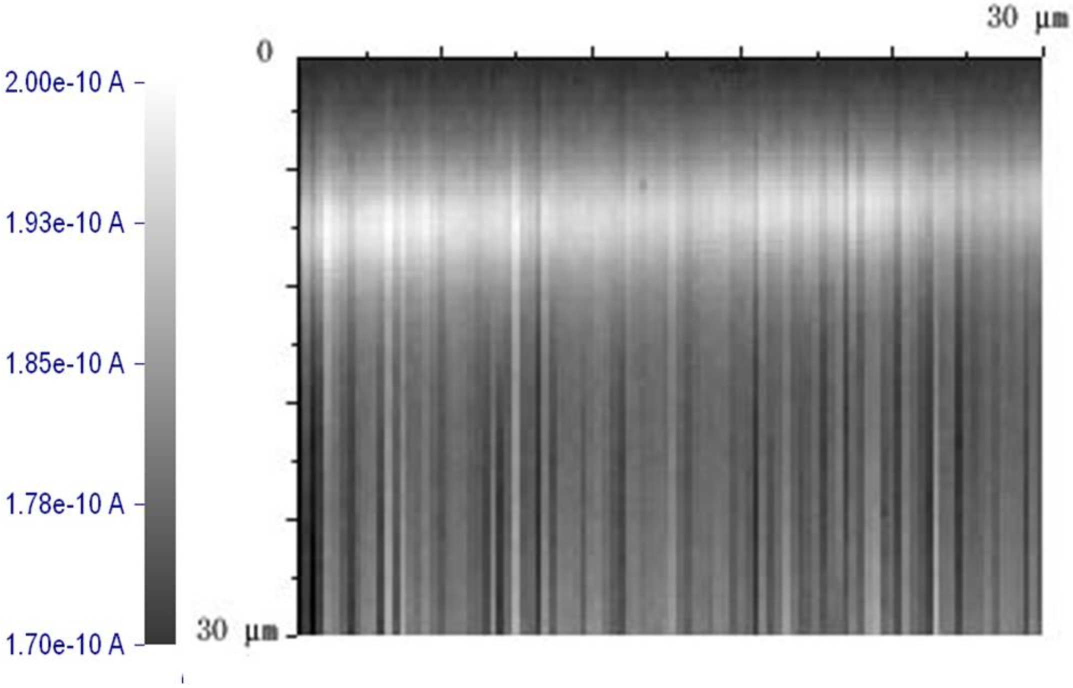

Figure 5-5. SECM image of an individual SWNT. The probe scan rate was 9 µm/s.

carbon nanotube, indicating $Ru(NH_3)_6^{3+}$ was regenerated at the nanotube surface to enhance the tip current. This image provides direct evidence that electron transfer occurs at the wall of a pristine SWNT. The tube diameter with respect to the tip radius is very small ($w/2a = 5 \times 10^{-4}$), which again confirms that SECM measurement is not limited by the tube diameter under diffusion-limited condition. Therefore, even such a narrow tube (~ 1.5 nm in diameter) could be detected by a micrometer-sized tip.

In summary, we demonstrated that an individual as-grown SWNT on a Si/SiO_2 substrate can be detected by SECM. Importantly, we discovered that the wall surface of the SWNT is highly reactive.

SUPPORTING INFORMATION

Nanoband Fabrication. An array of nanobands was fabricated as shown in Figure S 5-1. A 7000Å thermal oxide was grown at 1100 °C under flowing O2 on an RCA standard cleaned silicon chip (a 380 µm thick wafer polished on both sides from Silicon Quest, Santa Clara, CA). A side of the chip was spin-coated with poly(methylmethacrylate)/poly(methylmethacrylate-comethacrylic acid) as an e-beam bilayer resist. An e-beam tool (model EBPG-5HR, Leica Microsystems, Wetzlar, Germany) was used to expose the resist-coated chip to an electron beam. The exposed parts were dissolved by immersing the sample in the methyl isobutyl ketone:isopropyl alcohol (1:1 v/v) developer. A 5 nm-thick Cr film and then a 47 nm-thick Au film were deposited using e-gun evaporation (Semicore Equipment, Inc, Livermore, CA). The remaining e-beam resist and the metal on top of it were removed using Microposit Remover 1165. The nanobands were characterized using field-emission SEM equipped with an energy dispersed analysis of X-rays system, model XL-30 (Philips Electron Optics, Eindhoven, Netherlands).

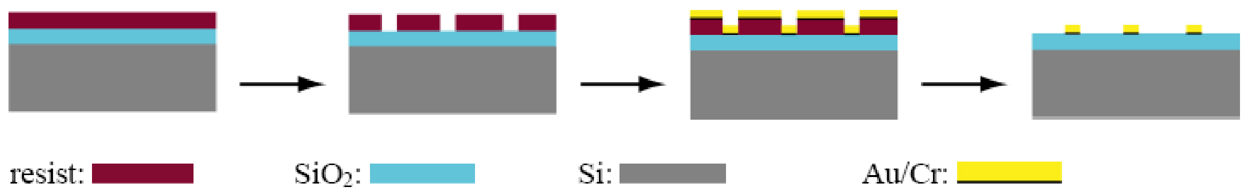

Figure S 5-1. Scheme of Nanoband Fabrication.

In order to obtain an active Au surface for electrochemical measurements, the nanoband array was soaked in acetone for 1 hour, dried with nitrogen, treated for 1 hour in a UV/ozone cleaner[27] (UV-tip Cleaner, BioForce Nanosciences, Inc., Ames, IA), soaked in ethanol for 1 hour, and dried with nitrogen.

Preteatments of Carbon Nanotube Sample. Prior to electrochemical measurements, the carbon nanotube sample was soaked in acetone and ethanol for 1 hour each, rinsed with 18.3 $M\Omega\cdot cm^{-1}$ deionized water (Nanopure, Barnstead, Dubuque, IA), and dried with nitrogen.

Electrochemical Measurement. All SECM experiments were carried out using 1 or 2 mM Ru(NH3)6Cl3 (Strem Chemicals, Newburyport, MA) in 0.1 M KCl. All reagents were used as received. All aqueous solutions were prepared with 18.3 $M\Omega\cdot cm^{-1}$ deionized water. The experiments were performed using a commercial SECM instrument with close-loop piezoelectric motors, CHI 910B (CH Instruments, Austin TX). The instrument was placed on a vibration isolation platform (model 63-533, TMC, Peabody, MA). A two-electrode setup was employed with a 1 mm-diameter AgCl-coated Ag wire serving as a reference/counter electrode and a ~2 μm-diameter Pt disk electrode (CH Instruments) as a SECM probe. The tip radius and insulating sheath thickness of Pt probes were determined from current approach curves at an insulating Teflon substrate.[28, 29] The tip diameters were also checked by optical microscopy.

For approach curve measurements, the center of a ~2 μm-diameter disk Pt probe was positioned directly above the center of a nanoband. The long axis of a nanoband was aligned in parallel to *x*-direction of the probe scan as shown in Figure 5-1. The tip was biased at a potential negative enough to reduce $Ru(NH3)_6^{3+}$ at a diffusion-limited rate and brought close to the SiO2 surface using the feedback mode. When the tip scanned over the nanoband in *y*-direction, an increase in tip current was observed. When no increase in the tip current was observed, the tip was moved in *x*-direction and then in *y*-direction, repeating the process until an increase in the tip current was obtained. The tip was stopped when the tip current reached the maximum value, where the tip center was positioned directly above the nanoband center in *y*-direction. Then, the tip was scanned in *x*-direction, where a plateau current was obtained over ~50 μm above the nanoband. The tip was positioned at the middle of the plateau region, which corresponds to the location of the nanoband center in *x*-direction. For approach curve measurements with 100 and 500 nm-wide Au bands, a tip potential was set at −0.35 and −0.40 V vs Ag/AgCl, respectively. The probe scan rate was 0.15 μm/s for data in Figure 5-3a and 0.75 μm/s for data in Figure 5-3c and Figure S 5-2.

Numerical Simulation. A SECM diffusion problem with a finite nanoband under a disk SECM probe was defined in Cartesian coordinates as reported elsewhere.[11] Actual simulations were carried out in a quarter of the whole domain, i.e., x, y, $z > 0$. The outer substrate radius corresponds to $50a$ and limits the simulation space in the *x*- and *y*-directions. The simulation space behind the tip is defined by the value of $20a$, which is large enough to accurately simulate back diffusion of a mediator at a probe, even with $rg/a < 10$,[28] where rg is the outer diameter of the insulating sheath at the tip. The width and length of a band is defined by w and l, respectively. The band thickness is neglected, because of its small contribution to a quasi steady-state current at a band electrode.S5 Initially, the solution phase contains only one redox-active mediator, O, which is reduced to R at the tip (O + ne → R). The diffusion coefficients of O and R are assumed to be the mean value so that mathematical treatment is restricted to the concentration of O as given by $c(x, y, z)$.

The SECM diffusion problem is solved in a dimensionless form, where dimensionless parameters are defined by:

$$X = x/a \tag{S1}$$

$$Y = y/a \tag{S2}$$

$$Z = z/a \tag{S3}$$

$$L = d/a \tag{S4}$$

$$W = w/2a \tag{S5}$$

$$LL = l/2a \tag{S6}$$

$$\mathrm{C}(\mathrm{X}, Y, Z) = c(x, y, z)/c_0 \tag{S7}$$

$$\tau = 4Dt/a^2 \tag{S8}$$

$$\mathrm{RG} = r\mathrm{g}/a \tag{S9}$$

Steady-state diffusion of O in the solution phase can be expressed in the dimensionless form as

$$\frac{\partial C(X,Y,Z)}{\partial \tau} = 0.25[\frac{\partial^2 C(X,Y,Z)}{\partial X^2} + \frac{\partial^2 C(X,Y,Z)}{\partial Y^2} + \frac{\partial^2 C(X,Y,Z)}{\partial Z^2}] = 0 \tag{S10}$$

The value of 0.25 in eq S10 was used as a dimensionless diffusion coefficient in the simulation.

The boundary condition on the nanoband surface depends on the rate of mediator regeneration. When mediator regeneration occurs at the diffusion-limited rate, the boundary condition is given by

$$C(X, Y, Z) = 1 \; X \leq L, \mathrm{Y} \leq W, Z = 20 \tag{S11}$$

The substrate boundary condition for reversible mediator regeneration is given by

$$E = E^{0'} - \frac{RT}{nF} \ln \frac{1 - C(X,Y,L)}{C(X,Y,L)} \quad X \leq L, \mathrm{Y} \leq W, Z = 20 \tag{S12}$$

In a simulation, a value of $C(X,Y,L)$ was given as the boundary condition. The substrate potential was calculated using eq S12 to obtain a potential approach curve. When mediator regeneration is kinetically limited, only one-step, one-electron transfer processes (n = 1) are considered

$$\mathrm{O} + \mathrm{e} \underset{k_{\mathrm{b,s}}}{\overset{k_{\mathrm{f,s}}}{\rightleftharpoons}} \mathrm{R} \qquad \text{(S13)}$$

where kf,s and kb,s are the first-order heterogeneous rate constants. The rate constants are given

by

the Butler-Volmer relations[30]

$$k_{\mathrm{f,s}} = k^0 \exp[-\alpha F(E - E^{0'})/RT] \qquad \text{(S14)}$$

$$k_{\mathrm{b,s}} = k^0 \exp[(1-\alpha) F(E - E^{0'})/RT] \qquad \text{(S15)}$$

where k^0 is the standard rate constant, and α is the transfer coefficient. The corresponding substrate surface boundary condition in the dimensionless form is given by

$$0.25[\frac{\partial C(X,Y,Z)}{\partial Z}]_{Z=20} = \frac{0.25K(1+\theta)}{\theta^{\alpha}}\left(\frac{\theta}{\theta+1}\right) - C(X,Y,20)$$

$$X \le L,\ \mathrm{Y} \le W,\ Z = 20 \qquad \text{(S16)}$$

with

$$\theta = \exp[\frac{F}{RT}(E - E^{0'})] \qquad \text{(S17)}$$

$$K = \frac{k^0 \alpha}{D} \qquad \text{(S18)}$$

Eq S16 is equivalent to the expression of the flux boundary condition in COMSOL Multiphysics.

The other boundary conditions are:

disk probe surface

$$C(X,\ Y,\ Z) = 0 \qquad X^2 + Y^2 \le 1,\ Z = 20 \qquad \text{(S19)}$$

insulation region around the disk electrode

$$\left[\frac{\partial C(X,Y,Z)}{\partial Z}\right]_{Z=20} = 0 \qquad 1 < X^2 + Y^2 < \mathrm{RG}^2,\ Z = 20 \qquad \text{(S20)}$$

insulation region at the side of the disk electrode

$$\left[\frac{\partial C(X,Y,Z)}{\partial X}\right]_{Z=L} = 0 \qquad X^2 + Y^2 = \mathrm{RG}^2,\ 0 \le Z \le 20 \qquad \text{(S21)}$$

insulation region around the band electrode

$$\left[\frac{\partial C(X,Y,Z)}{\partial Z}\right]_{Z=0} = 0 \qquad LL < X \text{ or } W < Y, X^2 + Y^2 < 50^2,\ Z = 20 + L \quad \text{(S22)}$$

simulation space limits

$$C(X, Y, Z) = 1 \qquad X^2 + Y^2 = {}^{5022},\ 0 \le Z \le 20 + L \qquad \text{(S23)}$$

$$C(X, Y, Z) = 1 \qquad X^2 + Y^2 = \mathrm{RG}^2,\ Z = 0 \qquad \text{(S24)}$$

The diffusion problem was solved using COMSOL Multiphysics® version 3.2 (COMSOL, Inc., Burlington, MA), which applies the finite element method. An open circuit potential of a nanoband was chosen such that the substrate current, *i*s, is less than 1% of *i*T,∞ to satisfy an open circuit condition at the nanoband.[13] Integration of the surface fluxes at the nanoband and disk probe results in a quarter of the substrate and tip currents normalized with respect to $i_{T,\infty}$, respectively. Plots of the normalized tip current and the substrate potential versus the tip−substrate distance give the current and potential approach curves, respectively. Calculation at each distance took 5.10 minutes on a workstation equipped with a Xeon 3.0 GHz processor unit and 5.0 GB RAM with Linux. An example of the simulation for a quasi-reversible case is provided as an attachment, where $L = 1$, $W = 0.05$, $LL = 25$, RG = 10, $\theta = 5.9$, $\alpha = 0.5$, and $K = 4.38$. Diffusion coefficient of 7.5×10^{-6} cm^2/s for $\mathrm{Ru(NH3)_6}^{3+}$ was used to calculate k^0 from K using eq S18.

Effect of Mediator Concentration on Current Approach Curves. A solution of 2 mM Ru(NH3)6Cl3 in 0.1 M KCl was used to obtain a current approach curve at a 100 nm-wide Au band using a 2.8 μm-diameter disk Pt probe (Figure S 5-2). The normalized curve fits with a theoretical one for a quasi-reversible substrate reaction with $k0$ = 0.33 cm/s and α = 0.5. The kinetic parameters are the same as those obtained with 1 mM Ru(NH3)6Cl3, which confirms that the lateral electron conduction in the nanoband is not a rate-determining step.[14]

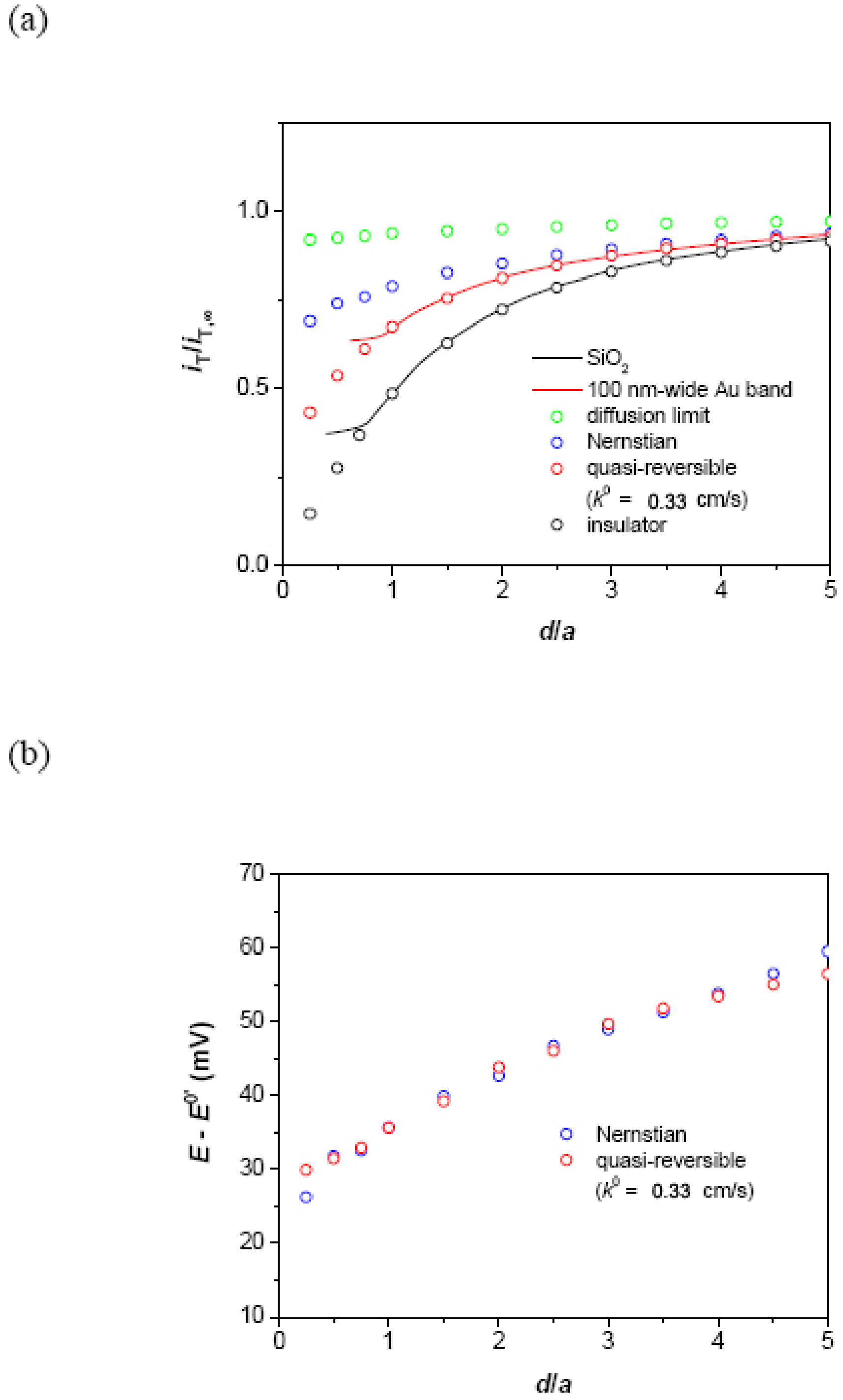

Figure S 5-2. (a) Current and (b) potential approach curves at a 100 nm-wide Au band as obtained using a 2.8 µm-diameter Pt disk probe in 0.1 M KCl containing 2 mM Ru(NH3)6Cl3. The lines and circles represent experimental and theoretical curves, respectively.

COMSOL Model Report

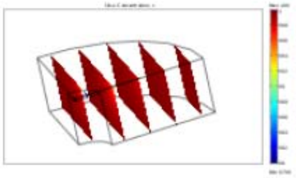

1. Table of Contents

- Title - COMSOL Model Report
- Table of Contents
- Model Properties
- Constants
- Geometry
- Geom1
- Geom2
- Geom3
- Solver Settings
- Postprocessing
- Variables

2. Model Properties

Property	**Value**
Model name	
Author	
Company	
Department	
Reference	
URL	
Saved date	Jan 6, 2007 4:23:53 PM
Creation date	Aug 19, 2005 8:34:48 AM
COMSOL version	COMSOL 3.2.0.304

File name: /home/sim/claire/band/l2a25 w2a0.05 rate/K=4.38/L=1.mph

Application modes and modules used in this model:

- Geom1 (3D)
    - Diffusion (Chemical Engineering Module)
- Geom2 (2D)
- Geom3 (2D)

3. Constants

Name	Expression	Value	Description
K	4.38	4.38	
theta	5.9	5.9	
alpha	0.5	0.5	

4. Geometry

Number of geometries: 3

4.1. Geom1

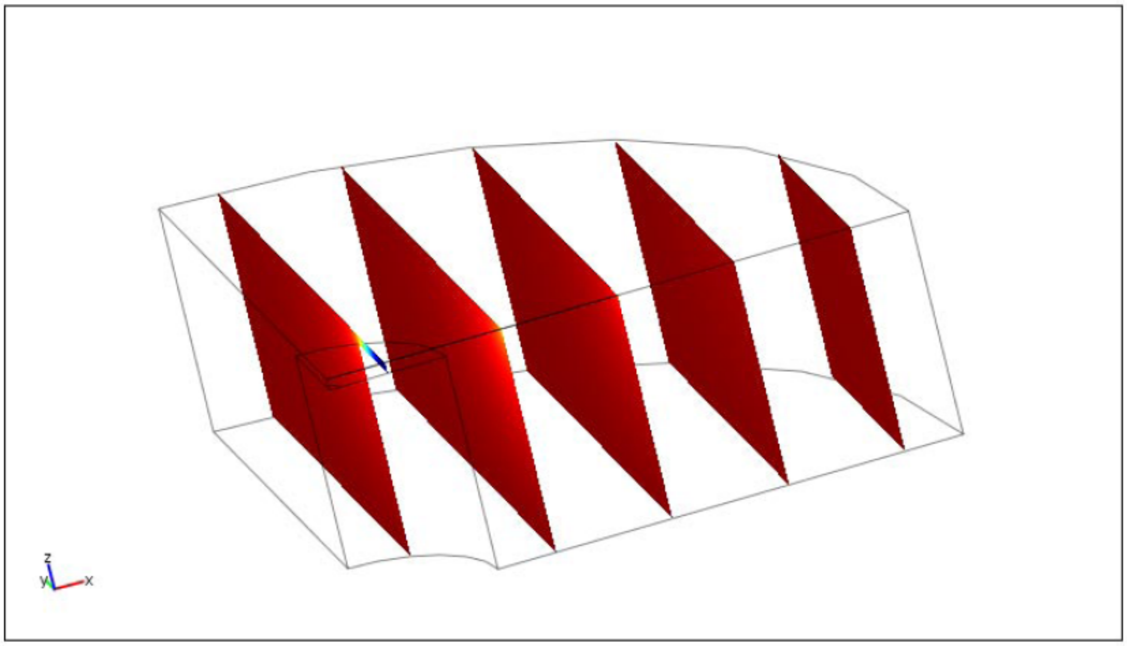

4.1.1. Point mode

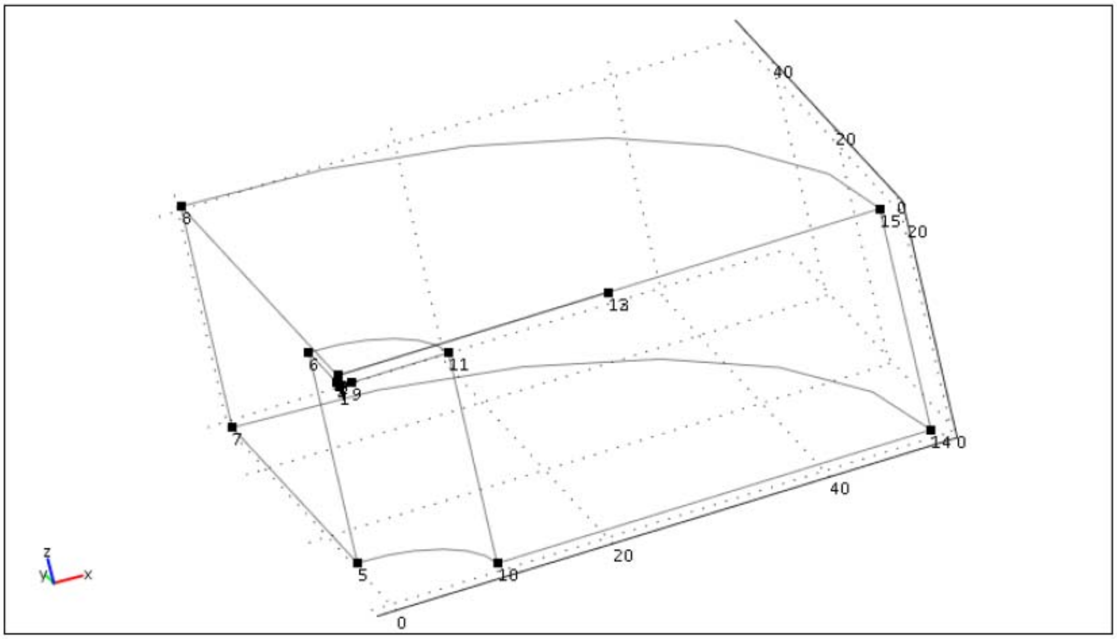

4.1.2. Edge mode

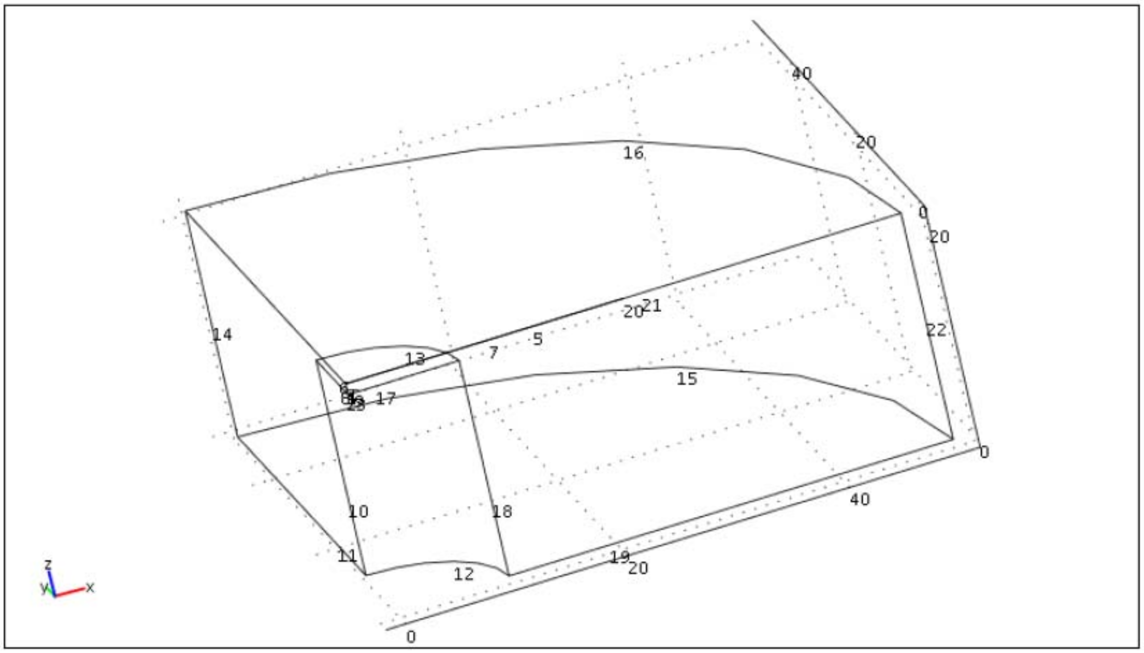

4.1.3. Boundary mode

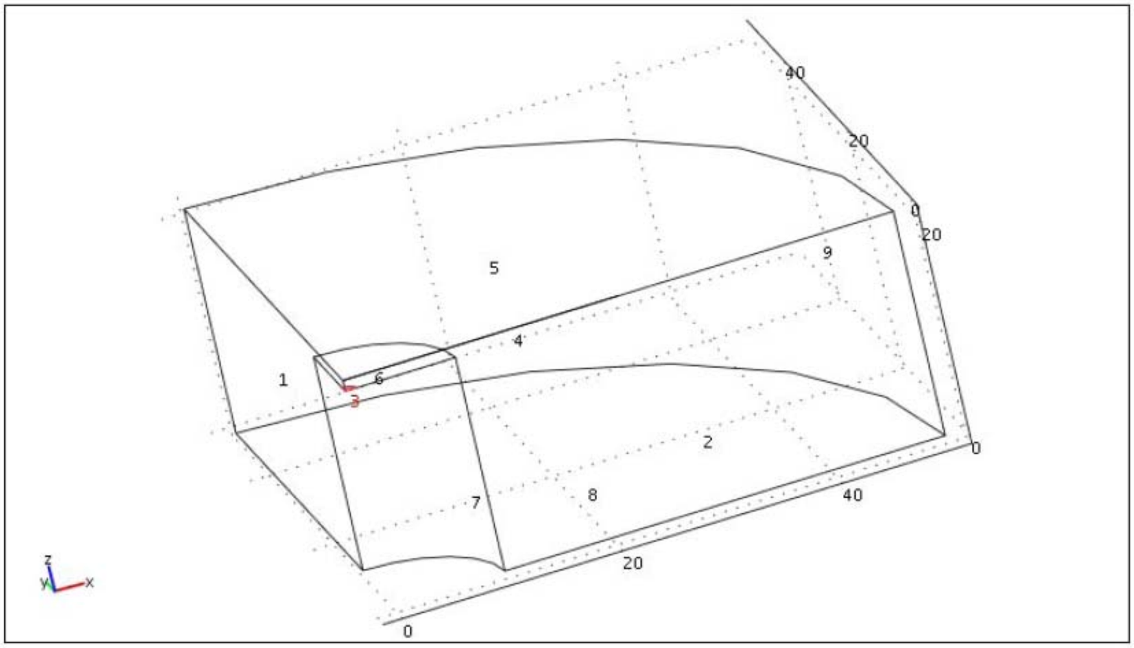

4.1.4. Subdomain mode

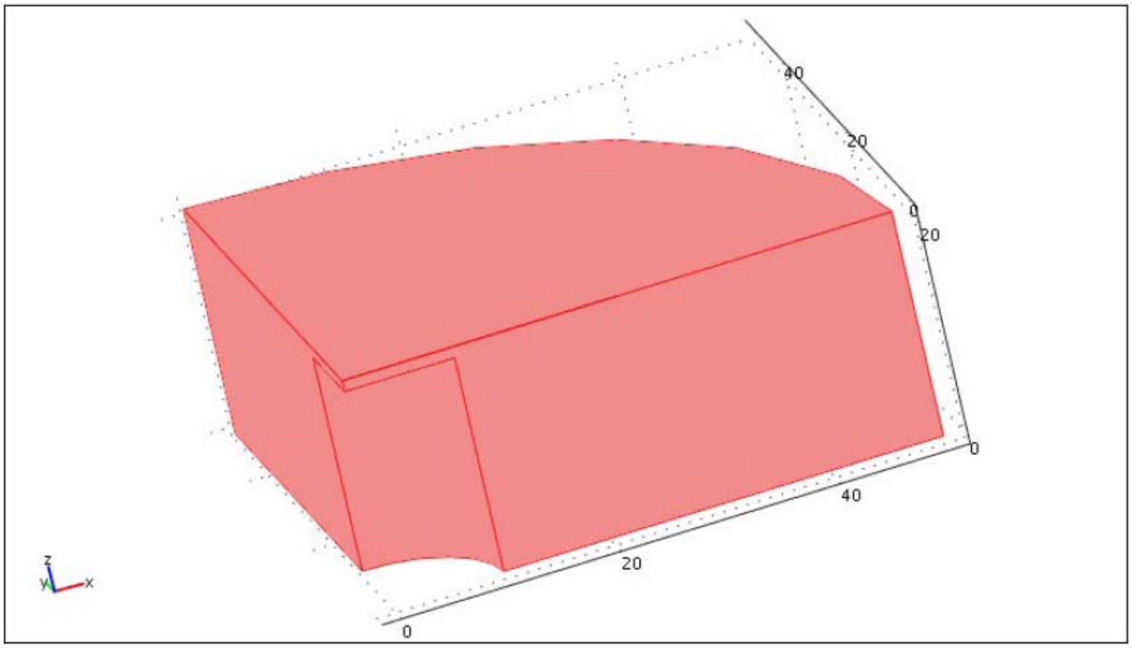

4.2. Geom2

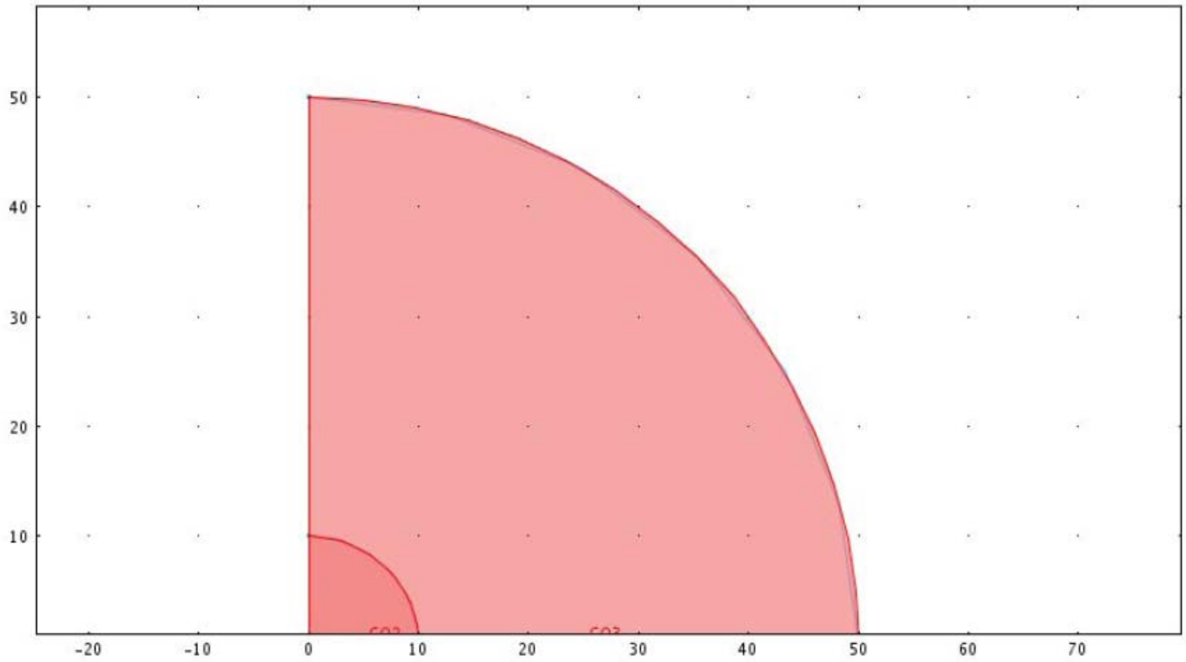

4.3. Geom3

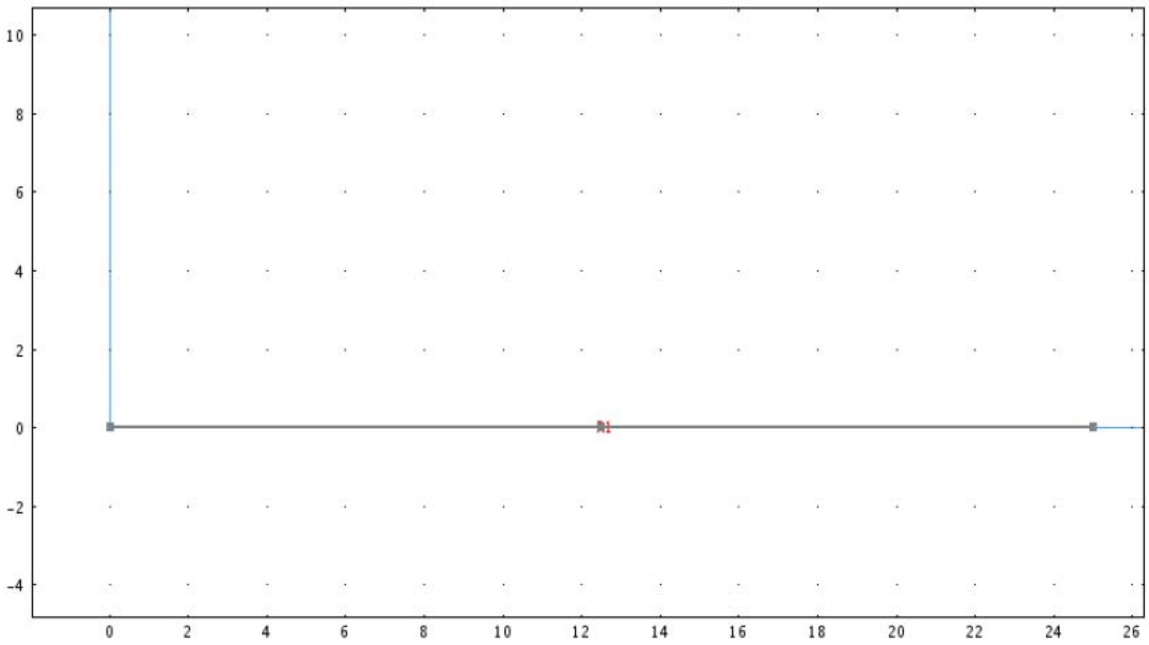

5. Geom1

Space dimensions: 3D

Independent variables: x, y, **z**

5.1. Mesh

5.1.1. Mesh Parameters

Parameter	Value
Maximum element size	
Maximum element size scaling factor	1
Mesh curvature factor	0.6
Element growth rate	1.5
Mesh curvature cut off	0.03
Resolution of narrow regions	0.5
Resolution of geometry	20
x-direction scale factor	1.0
y-direction scale factor	1.0

z-direction scale factor	1.0
Optimize quality	On
Mesh geometry to level	Subdomain

Subdomain	1
Maximum element size	
Element growth rate	

Boundary	1-9
Maximum element size	
Element growth rate	
Mesh curvature factor	
Mesh curvature cut off	

Edge	9, 13	7	1-6, 8, 10-12, 14-22
Maximum element size	0.01	0.1	
Element growth rate			
Mesh curvature factor			
Mesh curvature cut off			

Point	1-15
Maximum element size	
Element growth rate	

5.1.2. Mesh Statistics

Number of degrees of freedom	380659
Number of edge elements	2394
Number of boundary elements	30424
Number of elements	262118
Minimum element quality	0.2430

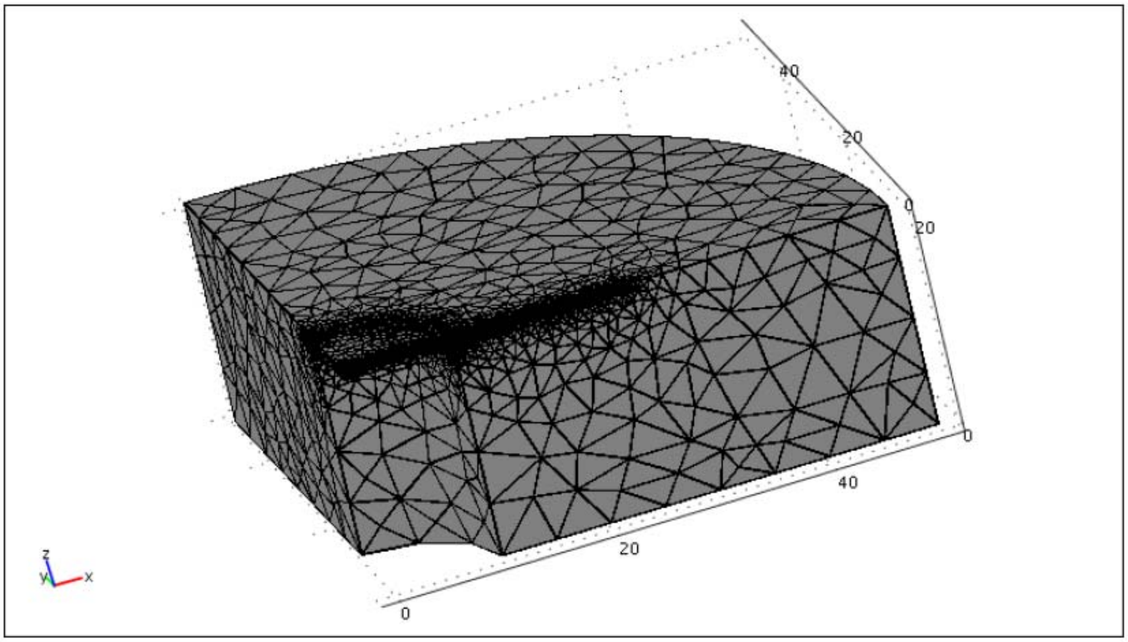

5.2. Application Mode: Diffusion (di)

Application mode type: Diffusion (Chemical Engineering Module)

Application mode name: di

5.2.1. Application Mode Properties

Property	Value
Default element type	Lagrange - Quadratic
Analysis type	Transient
Equilibrium assumption	Off
Frame	Frame (xyz)
Weak constraints	Off

5.2.2. Variables

Dependent variables: c

Shape functions: shlag(2,'c')

Interior boundaries active

5.2.3. Boundary Settings

Boundary		1-2, 5-7	3
Type		Insulation/Symmetry	Concentration
Mass transfer coefficient (kc)		0	0
Bulk concentration (cb)		0	0
Concentration (c0)		0	0

Boundary	4	8-9
Type	Flux	Concentration
Mass transfer coefficient (kc)	**0.25*K*(1+theta)/theta^alpha**	0
Bulk concentration (cb)	**theta/(1+theta)**	0
Concentration (c0)	0	**1**

5.2.4. Subdomain Settings

Subdomain		1
Diffusion coefficient (D)		**0.25**

Subdomain initial value		1
Concentration, c (c)		1

6. Geom2

Space dimensions: 2D

Independent variables: x, y, **z**

7. Geom3

Space dimensions: 2D

Independent variables: x, y, **z**

8. Solver Settings

Solve using a script: off

Analysis type	Transient
Auto select solver	On
Solver	Stationary nonlinear
Solution form	General
Symmetric	On
Adaption	Off

8.1. Conjugate gradients

Solver type: Linear system solver

Parameter	Value
Relative tolerance	1.0E-6
Factor in error estimate	400.0
Maximum number of iterations	10000

8.1.1. Algebraic multigrid

Solver type: Preconditioner

Parameter	Value
Number of iterations	2
Multigrid cycle	V-cycle
Maximum number of levels	6
Max DOFs at coarsest level	5000
Quality of multigrid hierarchy	3

8.1.1.1. SOR

Solver type: Presmoother

Parameter	Value
Number of iterations	2
Relaxation factor (omega)	1.0

8.1.1.2. SORU

Solver type: Postsmoother

Parameter	Value
Number of iterations	2
Relaxation factor (omega)	1.0

8.1.1.3. UMFPACK

Solver type: Coarse solver

Parameter	Value
Drop tolerance	0.0
Pivot threshold	0.1
Memory allocation factor	0.7

8.2. Nonlinear

Parameter	Value
Relative tolerance	1.0E-6
Maximum number of iterations	25
Manual tuning of damping parameters	Off
Highly nonlinear problem	Off
Initial damping factor	1.0
Minimum damping factor	1.0E-4

Restriction for step size update	10.0

8.3. Advanced

Parameter	Value
Constraint handling method	Elimination
Null-space function	Automatic
Assembly block size	5000
Use Hermitian transpose of constraint matrix	On
Use complex functions with real input	Off
Stop if error due to undefined operation	On
Type of scaling	Automatic
Manual scaling	
Row equilibration	On
Manual control of reassembly	Off
Load constant	On
Constraint constant	On
Mass constant	On
Damping (mass) constant	On
Jacobian constant	On
Constraint Jacobian constant	On

9. Postprocessing

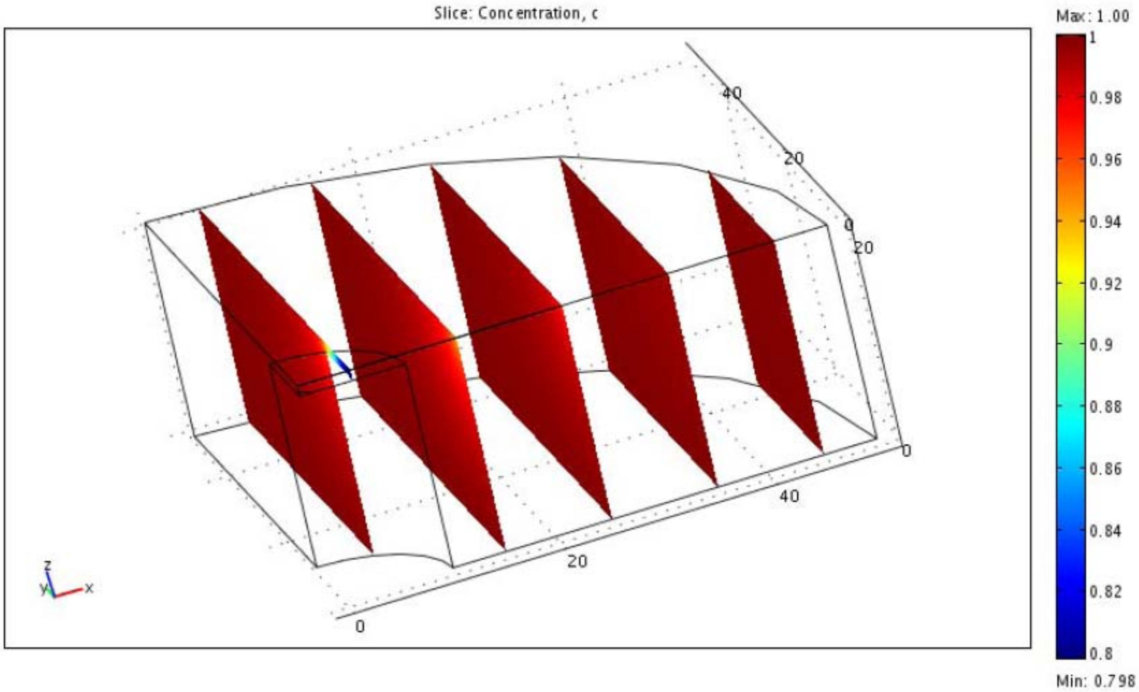

10. Variables

10.1. Boundary

Name	Description	Expression
ndflux_c_di	Normal diffusive flux, c	nx_di * dflux_c_x_di+ny_di * dflux_c_y_di+nz_di * dflux_c_z_di

10.2. Subdomain

Name	Description	Expression
grad_c_x_di	Concentration gradient, c, x component	cx
dflux_c_x_di	Diffusive flux, c, x component	-(Dxx_c_di * cx+Dxy_c_di * cy+Dxz_c_di * cz)
grad_c_y_di	Concentration gradient, c, y component	cy
dflux_c_y_di	Diffusive flux, c, y component	-(Dyx_c_di * cx+Dyy_c_di * cy+Dyz_c_di * cz)
grad_c_z_di	Concentration gradient, c, z component	cz
dflux_c_z_di	Diffusive flux, c, z component	-(Dzx_c_di * cx+Dzy_c_di * cy+Dzz_c_di * cz)
grad_c_di	Concentration gradient, c	sqrt(grad_c_x_di^2+grad_c_y_di^2+grad_c_z_di^2)
dflux_c_di	Diffusive flux, c	sqrt(dflux_c_x_di^2+dflux_c_y_di^2+dflux_c_z_di^2)

ACKNOWLEDGEMENT

This work was supported by grants from the National Science Foundation (DBI0242561) and the National Institute of Health (GM073439). We are grateful to Prof. Jing Kong (Department of Material Science and Engineering and Department of Electrical Engineering and Computer Science, Massachusetts Institute of Technology) for kindly providing us the carbon nanotube samples. We thank the Department of Materials Science and Engineering for the provision of access to the scanning electron microscopy instrumentation. Nanoband fabrication was performed at the Penn State Nanofabrication Facility, a member of the NSF's National Nanotechnology Infrastructure Network.

REFERENCES

(1) Xia, Y.; Yang, P.; Sun, Y.; Wu, Y.; Mayers, B.; Gates, B.; Yin, Y.; Kim, F.; Yan, H. *Adv. Mater.* **2003**, *15*, 353–389.

(2) Hurst, S. J.; Payne, E. K.; Qin, L. D.; Mirkin, C. A. *Angewandte Chemie-International Edition* **2006**, *45*, 2672-2692.

(3) Avouris, P. *Accounts Of Chemical Research* **2002**, *35*, 1026–1034.

(4) Kolmakov, A.; Moskovits, M. *Annu. Rev. Mater. Sci.* **2004**, *34*, 151–180.

(5) Wang, J. *Electroanalysis* **2005**, *17*, 7–14.

(6) Kline, T. R.; Tian, M. L.; Wang, J. G.; Sen, A.; Chan, M. W. H.; Mallouk, T. E. *Inorganic Chemistry* **2006**, *45*, 7555-7565.

(7) Che, G.; Lakshmi, B. B.; Fisher, E. R.; Martin, C. R. *Nature* **1998**, *393*, 346–349.

(8) Morris, R. B.; Franta, D. J.; White, H. S. *J. Phys. Chem.* **1987**, *91*, 3559–3564.

(9) Heller, I.; Kong, J.; Heering, H. A.; Williams, K. A.; Lemay, S. G.; Dekker, C. *Nano Lett.* **2005**, *5*, 137–142.

(10) Heller, I.; Kong, J.; Williams, K. A.; Dekker, C.; Lemay, S. G. *J. Am. Chem. Soc.* **2006**, *128*, 7353-7359.

(11) Xiong, H.; Gross, D. A.; Guo, J.; Amemiya, S. *Anal. Chem.* **2006**, *78*, 1946–1957.

(12) Wightman, R. M.; Wipf, D. O. In *Electroanalytical Chemistry*; Bard, A. J., Ed.; Marcel Dekker: New York, 1989; Vol. 15, pp 267–351.

(13) Xiong, H.; Guo, J.; Amemiya, S. *Anal. Chem.* **2007**, *79*, 2735–2744.

(14) Wilson, N. R.; Guille, M.; Dumitrescu, I.; Fernandez, V. R.; Rudd, N. C.; Williams, C. G.; Unwin, P. R.; Macpherson, J. V. *Anal. Chem.* **2006**, 7006–7015.

(15) Muzikar, M.; Fawcett, W. R. *Analytical Chemistry* **2004**, *76*, 3607-3611.

(16) Tusseri, R. I.; Posadas, D. *J. Electoanal. Chem.* **1985**, *191*, 387–399.

(17) Baughman, R. H.; Zakhidov, A. A.; de Heer, W. A. *Science* **2002**, *297*, 787-792.

(18) Gooding, J. J. *Electrochimica Acta* **2005**, *50*, 3049-3060.

(19) Bertoncello, P.; Edgeworth, J. P.; Macpherson, J. V.; Unwin, P. R. *J. AM. Chem. Soc.* **2007**, *129*, 10982-10983.

(20) Ajayan, P. M.; Lambert, J. M.; Bernier, P.; Barbedette, L.; Colliex, C.; Planeix, J. M. *Chem. Phys. Lett.* **1993**, *215*, 509-517.

(21) Guo, T.; Nikolaev, P.; Thess, A.; Colbert, D. T.; Smalley, R. E. *Chem. Phys. Lett.* **1995**, *243*, 49-54.

(22) Odom, T. W.; Huang, J. L.; Kim, P.; Lieber, C. M. *Nature* **1998**, *391*, 62-64.

(23) Dai, H. *Acc. Chem. Res.* **2002**, *35*, 1035-1044.

(24) Reina, A.; Hofmann, M.; Zhu, D.; Kong, J. *J. Phys. Chem. C* **2007**, *111*, 7292-7297.

(25) Gooding, J. J.; Wibowo, R.; Liu, J.; Yang, W.; Losic, D.; Orbons, S.; Mearns, F. J.; Shapter, J. G.; Hibbert, D. B. *J. Am. Chem. Soc.* **2003**, *125*, 9006-9007.

(26) Nugent, J. M.; Santhanam, K. S. V.; Rubio, A.; Ajayan, P. M. *Nano Lett.* **2001**, *1*, 87-91.

(27) Zhou, J. F.; Wipf, D. O. *J. of Electroanal. Chem.* **2001**, *499*, 121-128.

(28) Shao, Y.; Mirkin, M. V. *J. Phys. Chem. B* **1998**, *102*, 9915–9921.

(29) Amemiya, S.; Bard, A. J. *Anal. Chem.* **2000**, *72*, 4940–4948.

(30) Bard, A. J.; Faulkner, L. R. *Electrochemical Methods: Fundamentals and Applications*, 2nd ed.; John Wiley & Sons: New York, 2001.

6.0 INTRODUCTION TO NANOPROBES FOR SCANNING ELECTROCHEMICAL MICROSCOPY

Nanoelectrodes are useful as SECM probes for obtaining better spatial resolution of the electrochemical imaging of the surface. The spatial resolution of the SECM imaging strongly depends on the size and shape of the electrode as well as on the separation between the electrode and the substrate surface. Advanced nanofabrication methods are advantageous in fabrication of nanoelecterodes with controlled size and shape in comparison to conventional manual fabrication methods.

In the following chapters I present a novel approach to reproducible fabrication of nanometer-size probes for SECM by utilizing nanofabrication methods. I found that chemically etched optical fibers are very good templates for nanoelectrodes because of their sharpness at the tip (~10 nm in diameter) as well as good etching reproducibility. My strategy in fabrication of nanoelectrodes is to cover the chemically etched optical fiber template with a sputtered thin gold layer and seal the Au-coated optical fiber by an insulating material (e.g. electrophoretic paint and SiO_2 deposited by plasma-enhanced chemical vapor deposition) leaving only the tip of the fiber exposed by shrinking of the electrophoretic paint film or by milling through focused ion beam.

7.0 FABRICATION AND CHARACTERIZATION OF CONICAL MICROMETER-SIZED AND SUBMICROMETER-SIZED PROBES TEMPLATED BY SELECTIVELY ETCHED OPTICAL FIBERS FOR SCANNING ELECTROCHEMICAL MICROSCOPY

Part of this work has been published as Hui Xiong, Jidong Guo, Kazuyoshi Kurihara, and Shigeru Amemiya, *Electrochem. Commun.,* 2004, 6, 615–620.

7.1 ABSTRACT

Selectively etched optical fibers were used as a template for fabrication of ultramicroelectrodes (UME), which are suitable for use as a probe in scanning electrochemical microscopy (SECM). Multistep index optical fibers with high-GeO_2-doped core and two cladding layers were chemically etched to a sharp point (10 nm in diameter) in NH_4F/HF buffer solutions. The etched fibers had a defined geometry and the etching process was highly reproducible. After etching, a layer of gold was sputtered on the fibers. The Au-coated fibers were then insulated by electrophoretic paint. The size and shape of the electrodes were determined by steady-state cyclic voltammetry and SECM. The SECM tip current-distance (approach) curves over conductive and insulating substrates agreed with the theoretical curves obtained by numerical simulations, which proves a conical electrode geometry. The base radius

and height of the conical electrodes determined by SECM were in the range of 0.255-1.0 and 0.3-1.2 μm, respectively.

7.2 INTRODUCTION

Optical fibers were first employed as microelectrodes for simultaneous electrochemical measurements in the early 90s.[1, 2] Since then, they become more important as the templates for the fabrication of probes for scanning photoelectrochemical microscopy[3,4] and scanning electrochemical/optical microscopy,[5,6] which allow the simultaneous measurements at microenvironments. The conventional way to fabricate such probes based on optical fibers is: (1) heating and pulling of optical fiber (2) metal coating (3) electrical insulation and (4) tip exposure. This method is typical in fabrication of near-field scanning optical microscope (NSOM) probes.[7] However, the electrodes made by the first step are not reproducible and the sharpness of the fibers is limited down to ~50nm in diameter.

In our work, we propose[8] a selective etching technique to reproducibly fabricate probes with defined geometry. High-GeO_2-doped optical fibers are chemically etched to a sharp point (10 nm in diameter)[9] in NH_4F/HF buffer solutions, due to the difference of the etching rate in high-GeO_2-doped fiber core and cladding layers. Also, we can easily adjust the apex angle of the fiber electrode by simply varying NH_4F/HF ratio and etching time. By coating etched fibers with a thin layer of Au through sputtering and then with an insulating polymer layer by electrophoretic paint technique, we successfully prepared conical electrodes in micro to sub-micrometer size. The probes were characterized by steady-state cyclic voltammetry, SECM and scanning electron microscopy (SEM).

7.3 MODEL

Theoretical SECM approach curves with conical probes have been obtained by analytical approximations[10] and later using numerical simulations based on the boundary element method[11]. There are also reports about steady-state limiting currents at finite conical microelectrodes[12]. However, none of them treated the geometry of the conical probes constructed here. Therefore, numerical simulations were carried out to describe the steady-state current at the conical tips as a function of the tip-substrate distance.

The geometry of the electrode is shown in Figure 7-1, where the angles at the tip and the insulating layer were determined to be 80° and 58°, respectively, by SEM. The tip angle corresponds to the aspect ratio, *h/a*, of 1.2, where *a* is the base radius of the conical tip and *h* is the height.

Consider a one-step reaction

$$O + ne \Leftrightarrow R \tag{1}$$

taking place at a conical electrode surface where species R reaches and species O leaves the electrode solely by diffusion. The steady-state diffusion equation in cylindrical coordination is

$$\frac{\partial c}{\partial t} = D\left(\frac{\partial^2 c}{\partial r^2} + \frac{1}{r}\frac{\partial c}{\partial r} + \frac{\partial^2 c}{\partial z^2}\right) = 0\,, \tag{2}$$

where r and z are the coordinates in directions parallel and normal to the electrode base plane, respectively, c is the mediator concentration at (r, z), and D is the diffusion coefficient of the mediator. The boundary conditions are: at conical electrode surface

$$c\left(r, -\frac{hr}{a}\right) = 0,\ 0 < r < a \tag{3}$$

at insulation regions

$$[\frac{\partial c(r,z)}{\partial r}]_{r=12a} = 0,\ \text{-}20a\text{-}h < z < \text{-}8a, \tag{4}$$

$$[\frac{\partial c(r,z)}{\partial N}] = 0,\ a < r < 12a, \tag{5}$$

where $\partial c(r,\ z)/\partial N$ is the normal derivative of the mediator concentration at the peripheral insulating surface of the conical tip

simulation space limit

$$c\ (r,\ z) = c_o,\ 12a < r < 100a,\ z = \text{-}20a\text{-}h, \tag{6}$$

$$\text{and } r = 100a,\ \text{-}20a\text{-}h < z < d \tag{7}$$

where c_o is the initial mediator concentration in the bulk solution and d is the tip-substrate distance.

axis of symmetry

$$[\frac{\partial c(r,z)}{\partial r}]_{r=0} = 0,\ 0 < z < d, \tag{8}$$

$$[\frac{\partial c(r,z)}{\partial z}]_{z=d} = 0,\ 0 < r < 100a \text{ (insulating substrate)} \tag{9}$$

$$c(r,\ d) = c_o,\ 0 < r < 100a \text{ (conductive substrate)} \tag{10}$$

The steady-state current to the conical electrode, i, is given by integrating the flux over the electrode surface

$$i = 2\pi nFD\int_0^a r[\frac{\partial c(r,-\frac{hr}{a})}{\partial N}]dr, \tag{11}$$

where $\partial c(r,\ \text{-}hr/a)/\partial N$ is the normal derivative of the mediator concentration at the electrode surface. The numerical solution of this SECM diffusion was solved with the program FEMLAB version 2.3 (COMSOL, Inc., Burlington, MA, USA), which uses the finite element method.

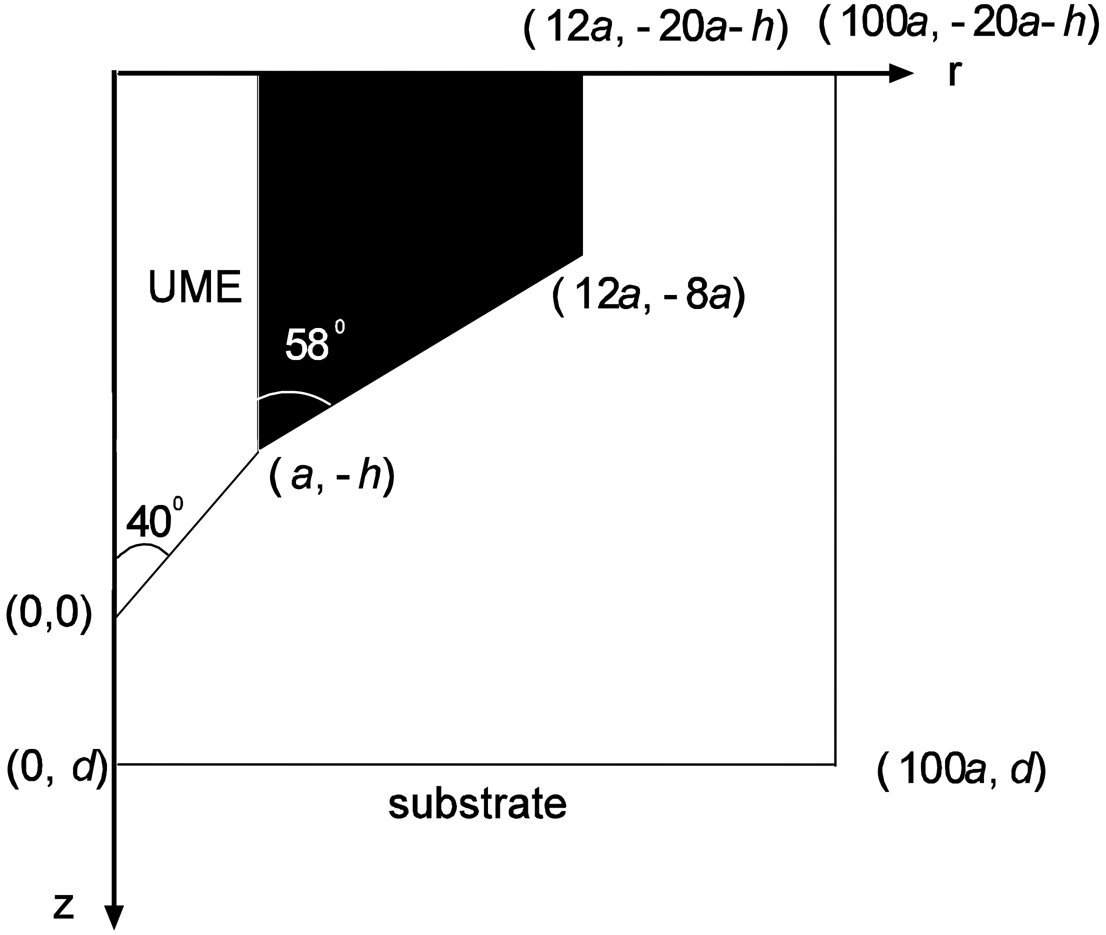

Figure 7-1. Diagram of space domain for the numerical analysis of a conical electrode. The electrode geometry was determined from SEM.

The typical concentration profiles of the mediator near the probe at a conductive and an insulating substrate are shown in Figure 7-2 and Figure 7-3, respectively.

Simulations were further modified for smaller tips ($a < 500$ nm) as the tip sharpness becomes comparable to the tip size. The geometry of the probe was revised as shown in Figure 7-4. And a parameter R (radius of inscribed circle) was introduced.

7.4 EXPERIMENTAL

7.4.1 Chemicals and Reagents

1,1′-ferrocenedimethanol (Sigma-Aldrich, St. Louis, MO, USA), KCl (J.T.Baker Chemical Co, Phillipsburgh, NJ, USA), sulfuric acid (J. T. Baker), NH_4F (Sigma-Aldrich) and HF (J.T. Baker) were reagent grade and used without further purification. All solutions were prepared with 18 $M\Omega\ cm^{-1}$ deionized water (Nanopure, Barnstead, Dubuque, IA, USA)

7.4.2 Electrode Fabrication

Multistep index optical fibers with GeO_2-doped SiO_2 core, SiO_2 inner cladding, and F-doped SiO_2 outer cladding (Figure 7-5) were obtained from Hoden Seimitsu Kako Kenkyusho, Kanagawa, Japan.[13] Optical fiber tips were prepared by stripping 1.5 cm of the insulating jacket from the tip of a 5-cm-long fiber with jacket remover JR-22 (Sumitomo, Electric Lightwave Copr., Research Triangle Park, NC, USA). The exposed portion of the fiber was cleaned with

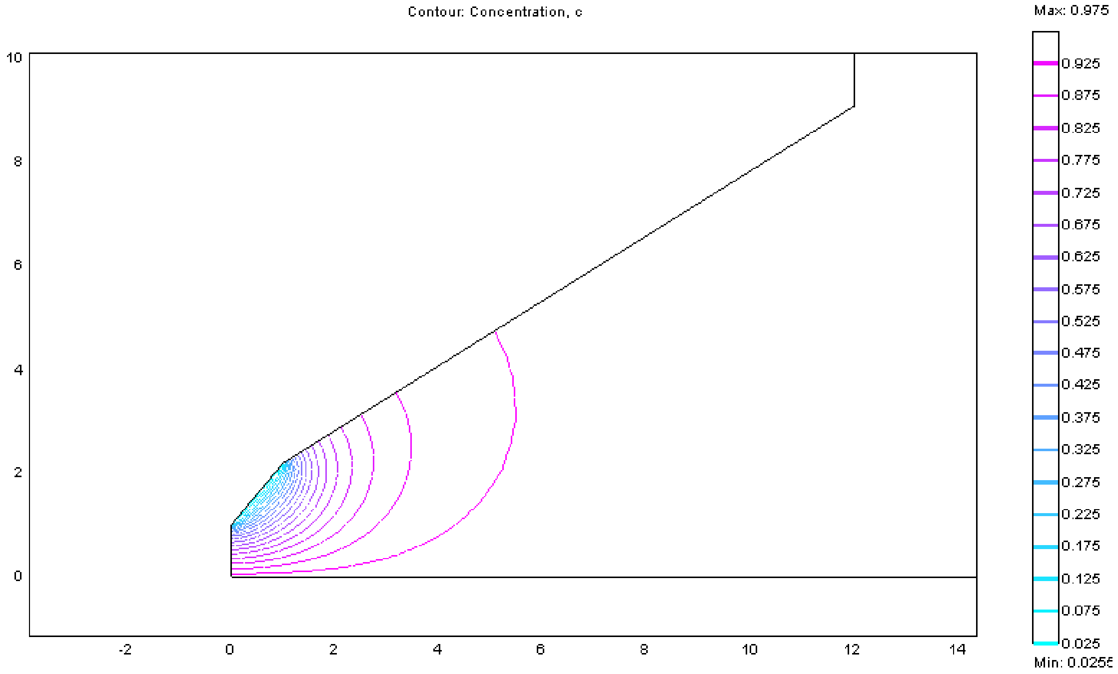

Figure 7-2. Concentration profile of the mediator near a conical probe approaching a conductor (d/a=1)

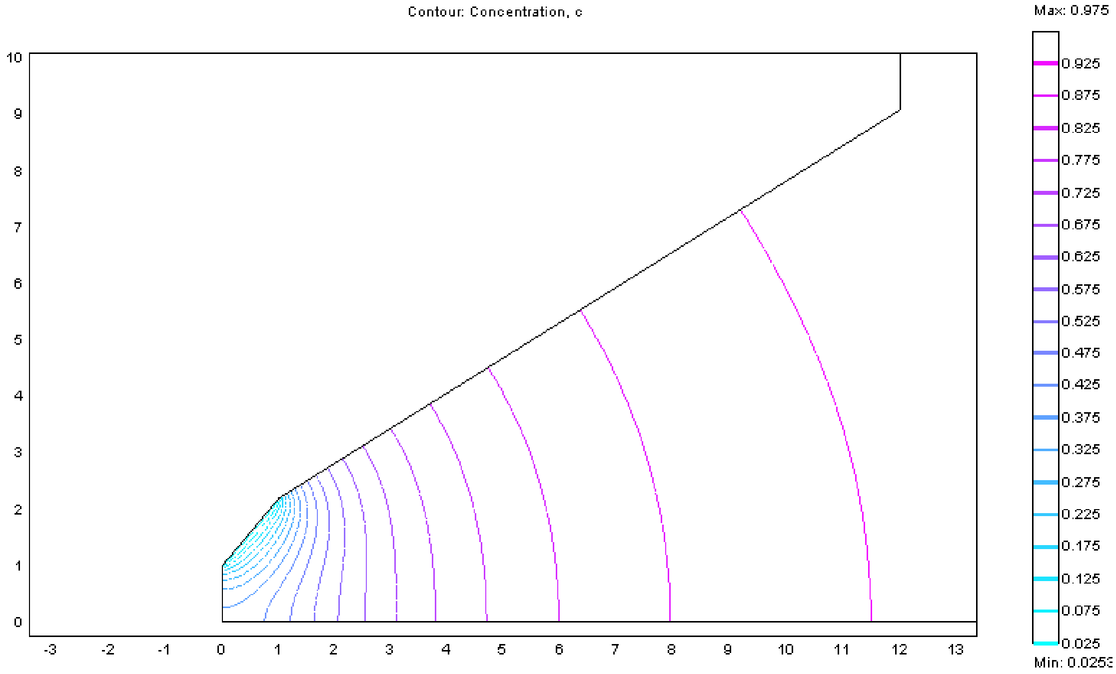

Figure 7-3. Concentration profile of the mediator near a conical probe approaching a insulator (d/a=1)

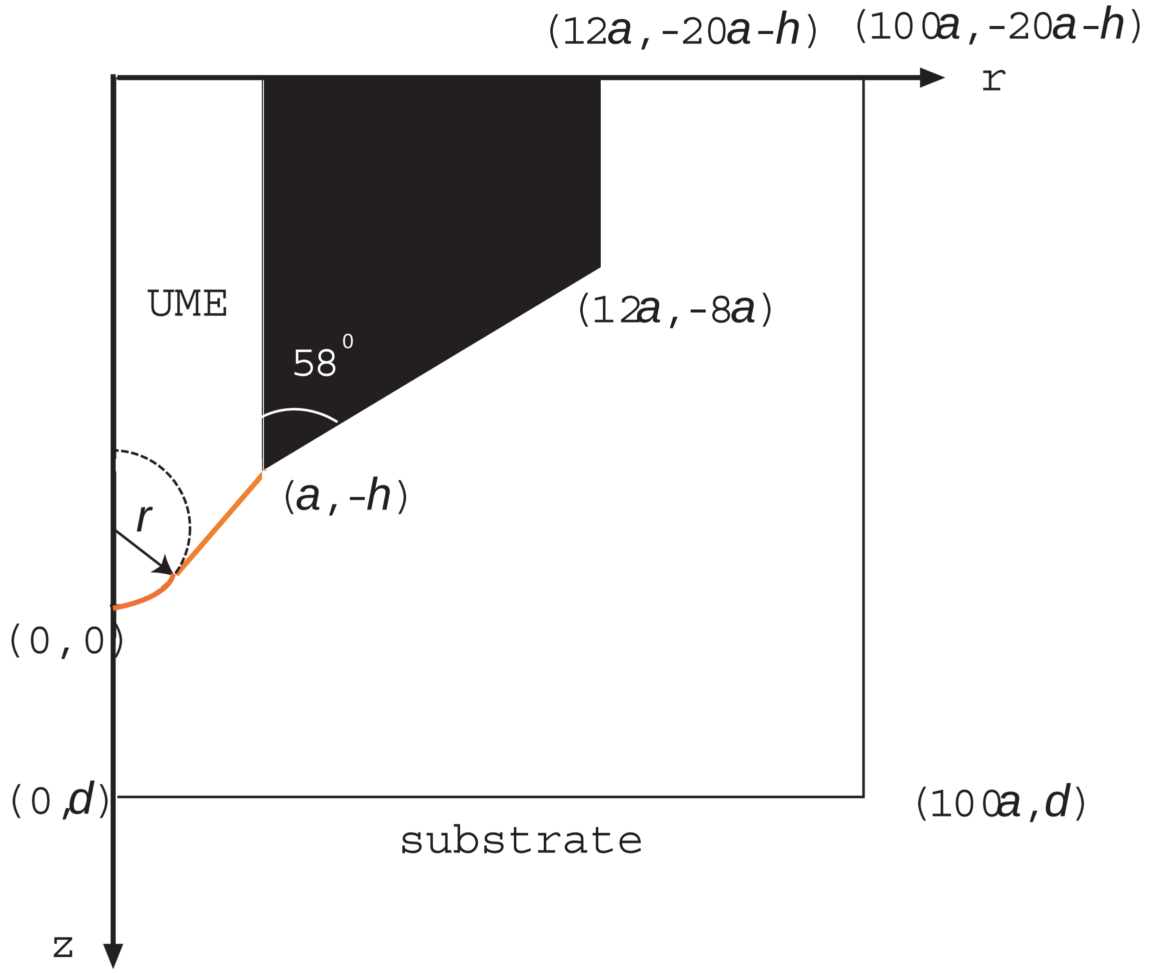

Figure 7-4. Modified geometry of the simulation space for numerical analysis of a conical electrode (a < 500 nm).

ethanol to remove any residual. A flat, smooth tip surface was obtained by cutting the exposed end of the fiber with fiber cleaver CT-20-12 (AFL Telecommunications, Franklin, TN, USA).

The fibers with smooth surfaces at the tips were then immersed in a NH_4F/HF etching solution. In order to optimize the solution composition as well as the etching time, the fiber tip was brought under an optical microscope BX-41 (Olympus America Inc., Melville, NY, USA) for investigation. Field-emission SEM equipped with an energy-dispersed analysis of X-rays (EDX) system, model XL-30 (Philips Electron Optics, Eindhoven, the Netherlands), was used to further determine the tip size and geometry. The optimum etching solution, which yields defined cone shape, consists of 40 wt% NH_4F, 48.0-51.0 wt% HF and water with volume ratio of 1.45:1:1.

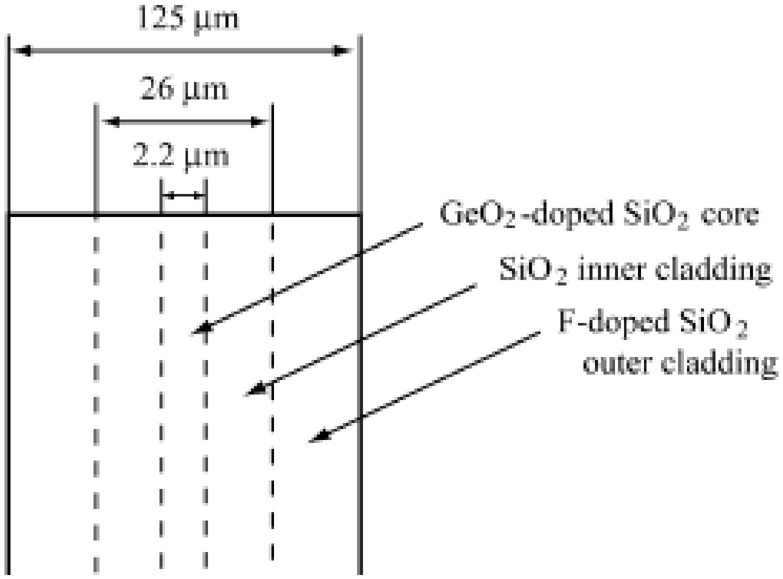

Figure 7-5. Schematic drawing of multistep index optical fibers.

An etched optical fiber was coated with a gold layer by sputter coater 108 auto (Ted Pella Inc., Redding, CA, USA). The fiber was vertically attached to a home-made stage so that the tapered tip is positioned toward the target. The tip-target distance was kept at 10 cm for reproducible coating. A flat glass substrate was simultaneously coated on the stage and the gold layer thickness on the glass was measured to be ~ 100 nm by atomic force microscope (DI 3100, Digital Instruments, Santa Barbara, CA, USA). Silver epoxy H20E (Epoxy Technology Inc., Billerica, MA, USA) was used to establish electrical connection via a Chrome wire.

The gold-coated fiber was immersed in a 1 M H_2SO_4 solution and scanned for 20 cycles at 1.5 V to clean the Au surface and thoroughly rinsed with deionized water. The insulation of the Au-coated fibers was carried out by electrophoretic paint method[5, 14, 15] originally developed by Bach et al. for coating STM tips[16, 17] and adapted by Schulte[18] for preparing carbon fiber microelectrodes. Slevin et al. used this method to prepare nanometer-scale Pt electrodes and electrochemical AFM tips,[14] which has then been adopted and modified by White's group[15] and Bard's group.[5] The gold-coated etched fiber was dipped in an aqueous anodic paint solution AE-X (Shimizu, Co., Ltd., Osaka, Japan), which contains poly (acrylic acid) (PAAH) with excess base to make it water soluble by deprotonation of the acidic groups, and a +2.0 V dc potential was applied between the optical fiber and a Pt coil for 5 s to oxidize H_2O ($2\ H_2O \rightarrow O_2 + 4H^+ + 4e^-$) at the fiber. PAA^- at the electrode surface was protonated, resulting in the precipitation of an insulating PAAH layer on the electrode. The insulated electrode was then removed from solution and cured in oven at 80°C for 20 min and then at 150°C for 30 min. The insulating layer shrank during curing step so that the sharp end of tip was exposed (Figure 7-6).

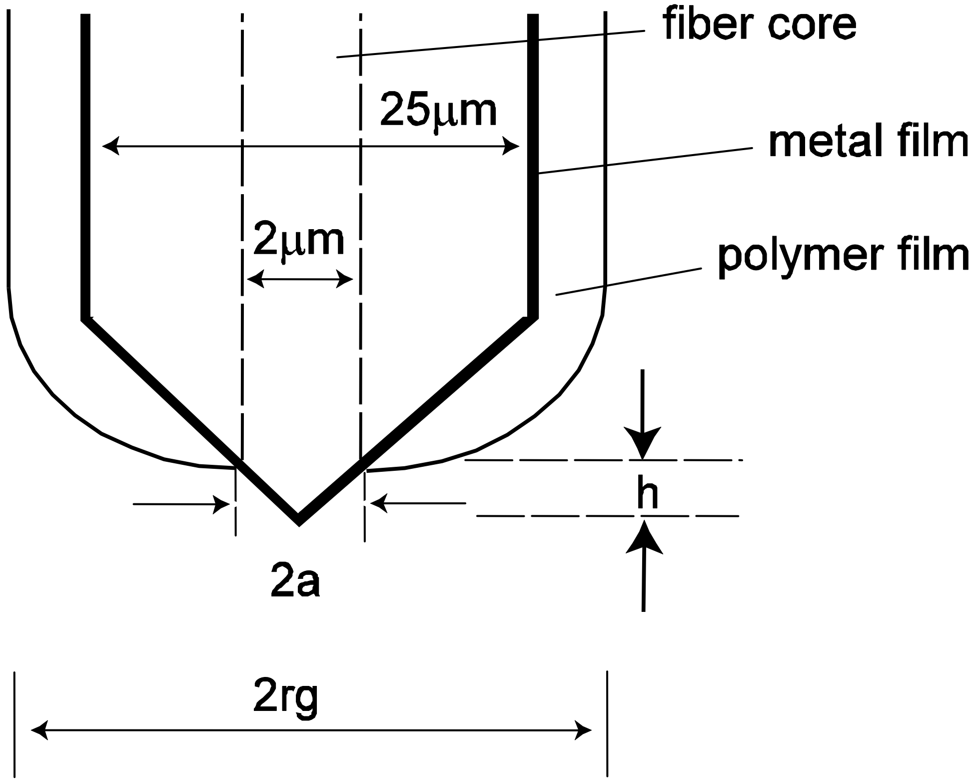

Figure 7-6. Electrode profile.

7.4.3 Electrochemical Measurements

For electrochemical measurements, a two-electrode system was used. The working electrode was the prepared tip and the quasi-reference electrode was a silver wire. A CH Instruments (Austin, TX, USA) model 600A and a home-built SECM were used for all electrochemical measurements. In SECM approach curve experiments, the prepared tip was brought to a substrate surface by a set of x, y, z stages (M-462, Newport Corp., CA, USA) and a piezoelectric positioner and controller (models P621.ZCD and E621SR, Physik Instrumente, Germany) to give smooth movement in the direction perpendicular to the surface. Flat glass, polychlorotrifluoroethylene and Pt were used as substrates for SECM experiments.

7.5 RESULTS AND DISCUSSION

7.5.1 Fabrication of Conical Probes based on Selectively Etched Optical Fibers and Characterization by SEM

The multistep index optical fibers were etched in a NH_4F/HF buffer solution and used as a template of conical microelectrodes. The composition of the etching solution was adjusted so that the GeO_2-doped fiber core and the inner pure silica cladding were etched at the same speed while the outer F-doped cladding was etched faster. Actually, right after 60 min of etching, the outer cladding layer became much thinner (Figure 7-7) and the ensemble of fiber core and inner cladding looked like a trapezoid. After 80 min, the outer cladding had been completely etched

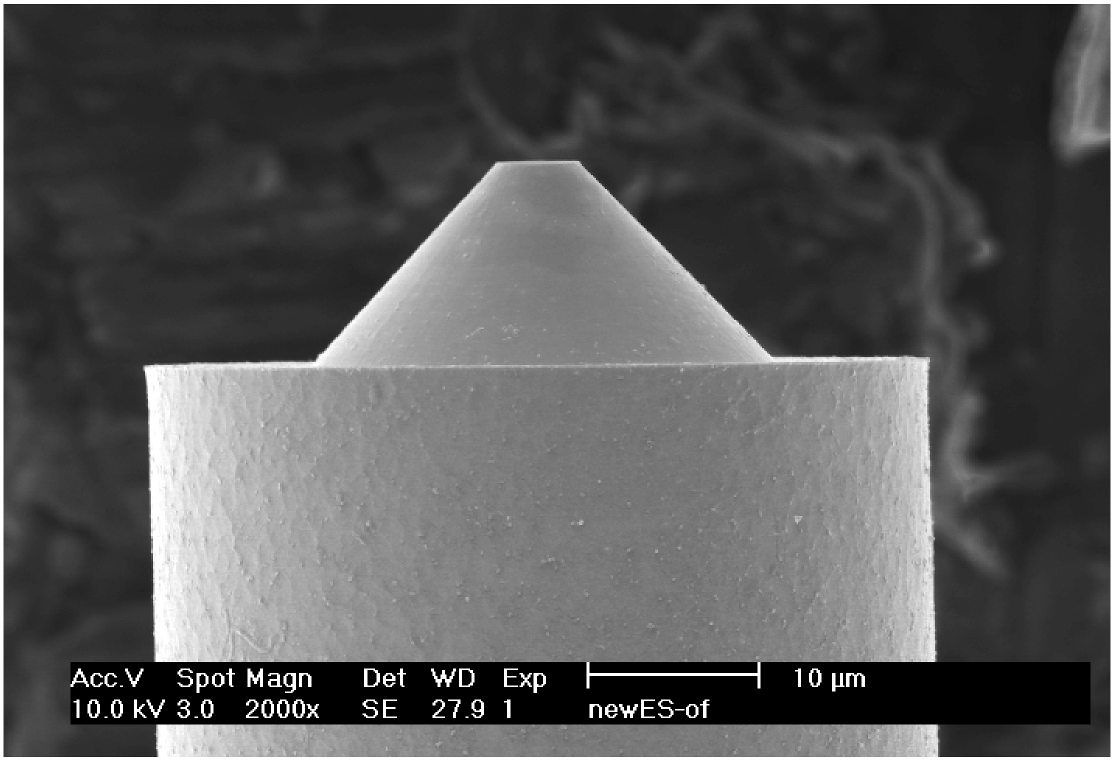

Figure 7-7. SEM image of a selectively etched optical fiber after etching for 60 min.

off and a sharp tip was formed (Figure 7-8). In SECM applications, using selectively etched multistep index fibers has advantages over fibers with GeO_2-doped core and a single cladding layer[9, 19, 20] in that it has smaller tip size (~ 25 μm in outer diameter), which makes it possible to bring the tip closer to the substrate. We also noticed that the temperature played an important role on the etching speed; even one degree increase of the temperature would increase the etching rate in 70 nm/min.

An etched fiber was coated with gold by sputtering and then insulated with electrophoretic paint. Figure 7-9 shows the SEM image of a conical probe after insulation. The image clearly shows a conical protrusion, which corresponds to the exposed gold tip. EDAX analysis was carried out to make sure that the protruding part was indeed the exposed gold tip as confirmed by EDAX spectrum.

7.5.2 Steady-state Cyclic Voltammetry

Exposition of a gold layer after deposition of electrophoretic paint was also confirmed by cyclic voltammetry carried out in a 1 mM 1,1′-ferrocenedimethanol/ 0.1 M KCl aqueous solution. The cyclic voltammogram obtained with the prepared tip is shown in Figure 7-10. Typically, a well defined sigmoidal cyclic voltammogram of a good-quality UME was obtained with a selectively etched conical probe insulated by electrophoretic paint. The diffusion-limited steady-state current at a conical electrodes in a bulk solution, $i_{T,\infty}$, can be expressed as

$$i_{T,\infty} = nFDc_o ax, \qquad (12)$$

where F is the Faraday constant, D is the diffusion coefficient of the mediator, and x is a geometric factor depending on the shape of the electrode. With the geometry defined in

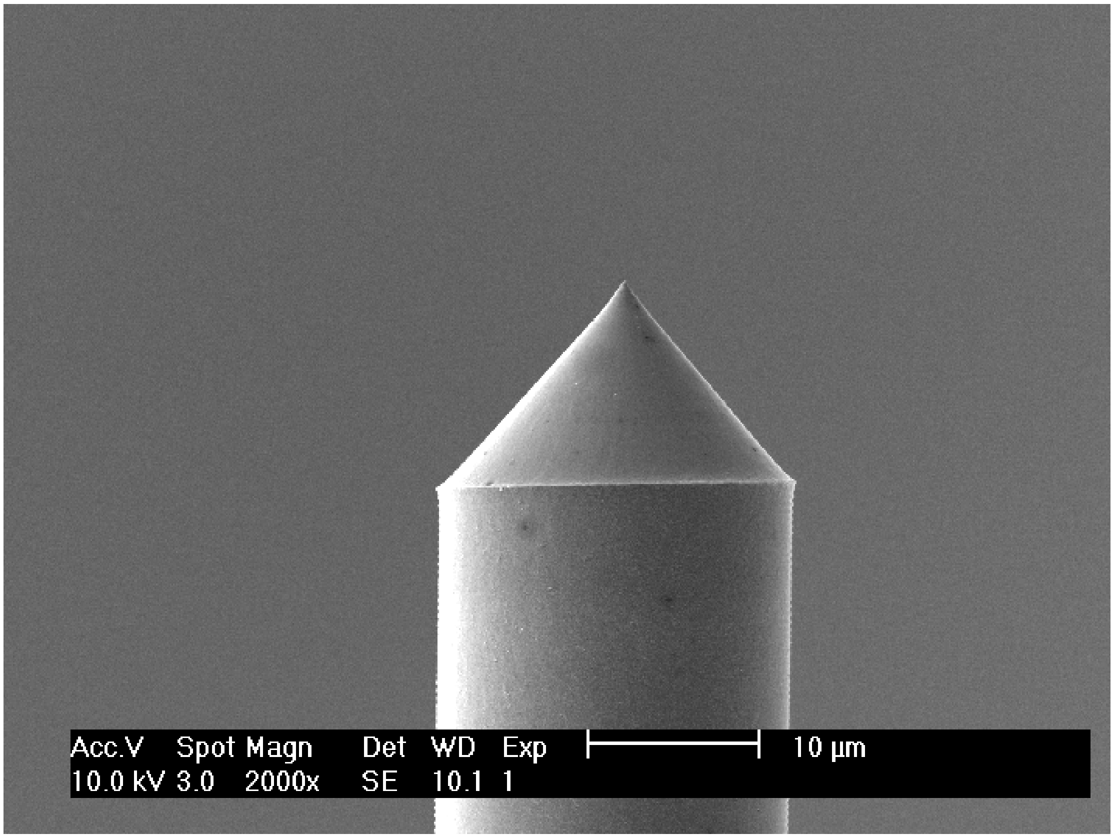

Figure 7-8. SEM image of a selectively etched optical fiber after etching for 80 min.

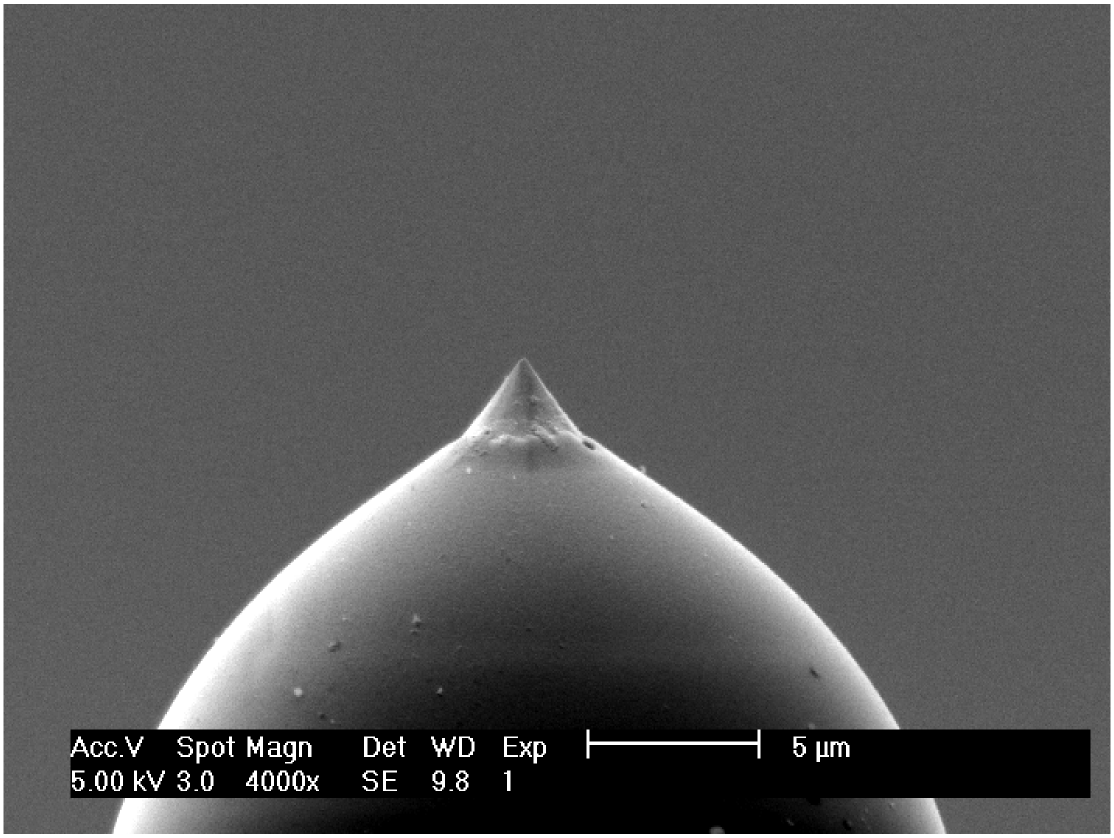

Figure 7-9. SEM image of a conical electrode after insulation by electrophoretic paint.

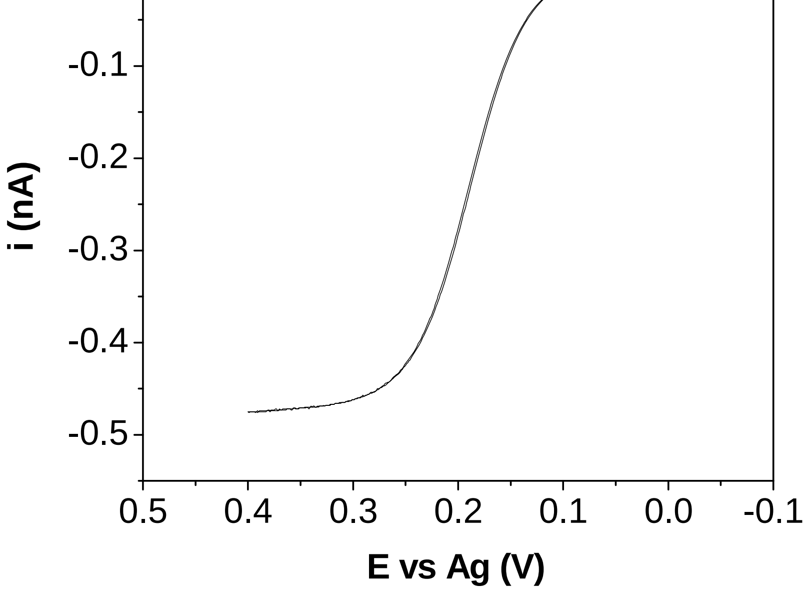

Figure 7-10. Cyclic votammogram from a conical probe in a aqueous solution of 1mM 1,1′-ferrocenedimethanol and 0.1 M KCl. Scan rate, 0.01 V/s.

Figure 7-1, a value of 6.74 was obtained for the geometry factor, *x*, using numerical simulations at a large tip-current separation ($d = 100a$). With the diffusion coefficient of 1,1′-ferrocenedimethanol (6.9×10^{-6} cm^2/s) determined by chronoamperometry at a 10 μm Pt microelectrode,[19, 20] the base radius, *a*, was calculated to be 1.0 μm according to Eq. 12 with $i_{T,\infty}$ of 0.470 nA. Only steady-state voltammetry, however, is not enough to confirm the profile of the prepared probes.[21] Indeed, the geometry and size of conical tips are determined by three independent parameters, i.e., the base radius, height of the conical tip, and the shape of the insulating sheath. Also, a gold surface may be exposed at the location other than the tip as pinholes.

7.5.3 SECM Approach Curve Measurements

SECM approach curves were measured for further characterization of the electrode size and geometry. SECM approach curves depend on the size and geometry of the probes so that they are used to characterize disk,[22] conical,[10, 23] spherical,[24, 25] hemispherical[26, 27] and ring electrodes.[28] The SECM approach at a Pt substrate was measured with the same conical probe for cyclic voltammetry in Figure 7-11. The tip potential was kept at 0.35 V where the oxidation of 1,1′-ferrocenedimethanol is diffusion limited and the probe was brought to the Pt surface at the speed of 1.0 μm/s. As the electrode moved toward the Pt substrate, the tip current increased gradually to 1.8 times of $i_{T,\infty}$ and then rapidly to more than 270 times of it (Figure 7-11a). The rapid increase is due to the contact between the tip and the substrate, where the active electrode area increases from the conical tip to the whole Pt substrate. This result confirms that the

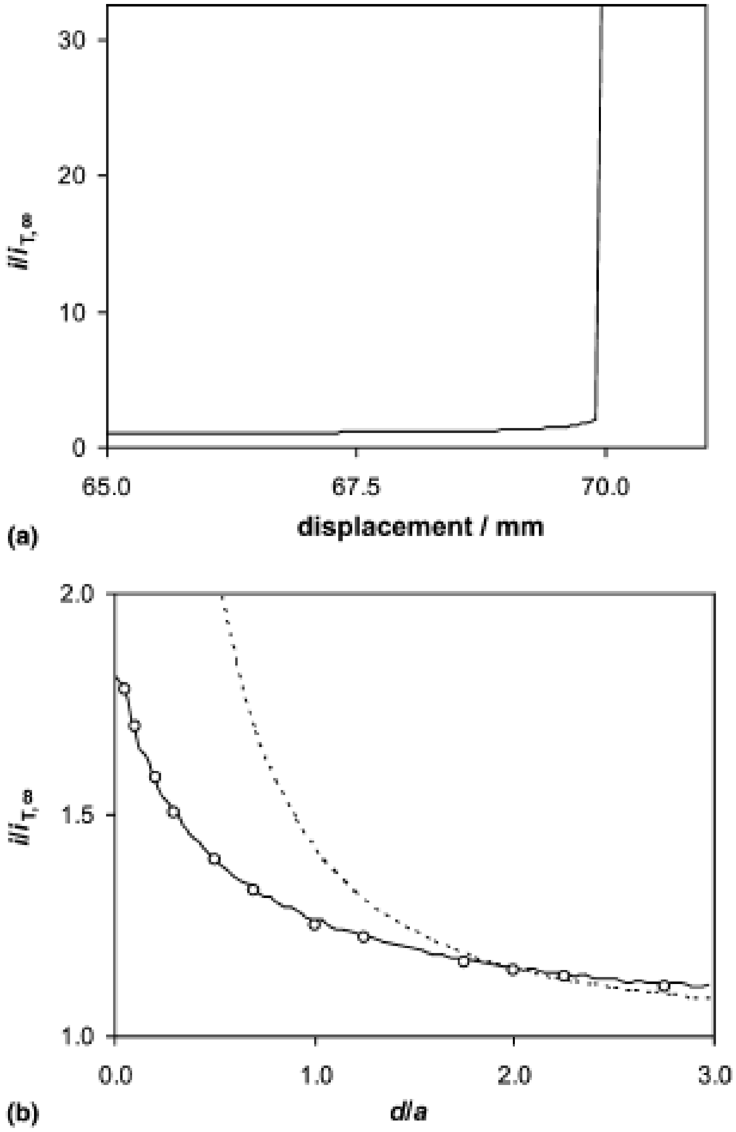

Figure 7-11. Experimental SECM approach curve (solid line) at a Pt substrate as obtained with the conical microelectrode used for cyclic voltammetry in Fig. 7-10. Solution contained 1 mM 1, 1'-ferrocenedimethanol and 0.1 M KCl in water. The circles represent the theoretical curve for a conical electrode with the tip angle of 80° (See Fig. 7-1 for the insulating layer geometry). The dotted line represents an approach curve of a disk-shaped electrode, where the disk radius and the outer radius of the insulating layer are *a* and 2*a*, respectively.

electrode tip is protruding from the insulating layer; otherwise, the insulating layer would touch the surface before the metal surface of the electrode touches it because even a slight tilt will cause the tip not moving vertically to the substrate. Figure 7-11b also shows a theoretical SECM approach curve of a disk-shaped electrode (RG=2). Compared to disk electrode (h = 0), conical electrode must approach closer to the substrate to reach a similar value of feedback current for a conductive substrate. The reason for the relatively smaller feedback at conical electrode with conductive substrates can be explained as follows: Far from the substrate, the diffusion to the UME tip achieves a spherical diffusion layer, whose dimensions are predominately determined by the base radius a, so the behavior is rather disk-like. However, when the tip approaches very close to the substrate, the diffusion layer is disturbed by the substrate before reaching a spherical diffusion layer and the dimensions of the diffusion layer are largely depend on the aspect ratio (h/a) or the tip angle of the conical tip. The experimental curve agrees very well with the theoretical one (Figure 7-11b), giving a = 1.0 μm and h = 1.2 μm. This good agreement also confirms the electrode geometry as defined in Figure 7-1.

The electrode geometry and size were further confirmed by SECM approach curve experiments at an insulating substrate. Figure 7-12a shows an experimental approach curve at a polychlorotrifluoroethylene substrate. The curve was obtained with the same probe as used for cyclic voltammertric and SECM positive feedback measurements in Figure 7-10 and Figure 7-11b. As the electrode moved to the insulating substrate, the tip current decreased to 48% of $i_{T,\infty}$. Compared to the theoretical approach curve by a disk electrode over an insulating substrate also shown in Figure 7-12b, the SECM feedback response for a conical probe needs to approach closer than a disk one in order to get the same level decrease of tip current. When the conical probe is positioned close to the insulating substrate, the substrate hinders the diffusion of the

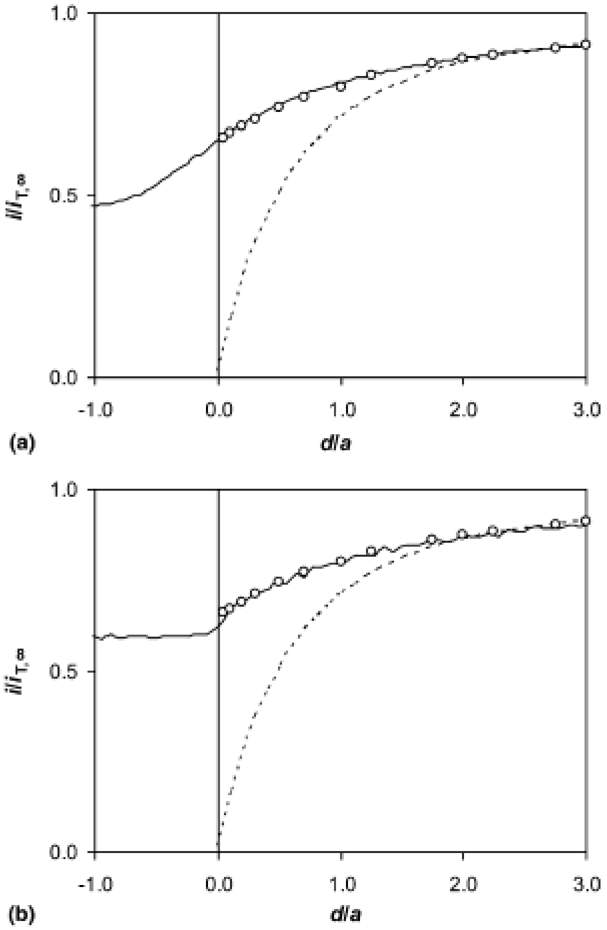

Figure 7-12. Experimental approach curves (solid lines) (a) over a polychlorotrifluoroethylene substrate of the same probe as used for Figs. 7-10 and 7-11 and (b) over a glass substrate of a conical electrode with the base radius of 0.70 μm. Solution contained 1 mM 1, 1’-ferrocenedimethanol and 0.1 M KCl in water. The circles represent the theoretical curve for a conical electrode with the tip angle of 80° (see Fig. 7-1 for the insulating layer geometry). The dotted lines represent an approach curve of a disk-shaped electrode, where the disk radius and the outer radius of the insulating layer are *a* and 2*a*, respectively.

mediator from the bulk solution to the electrode surface so that the tip current decreases to a value lower than $i_{T,\infty}$. The experimental curve fits well with the theoretical one based on the geometry defined in Figure 7-1 until the current decreases to 65% of $i_{T,\infty}$. The base radius was determined to be 1.0 μm, which agrees well with the value determined by cyclic voltammetry and the SECM approach experiment at a Pt substrate. However, the tip current decreased further. The final current value varies among electrodes in the range between 48% of $i_{T,\infty}$ and almost 0 as observed with a smaller electrode (a = 0.44 μm). We observed the further decrease of tip current with freshly prepared tips, which excludes the possibility of geometry changes on the tips dues to the contact with the tips and substrate by previous experiments. Meanwhile, the tip current over a glass substrate did not decrease to lower than 65% of $i_{T,\infty}$. Figure 7-12b shows an approach curve over a glass substrate at another conical electrode (a =0.70 μm). This result indicates that the further decrease of the tip current lower than 65% of $i_{T,\infty}$ is cause by the penetration of the conical tip into the soft polymer substrate. The penetration effect on the approach curve not only shows the robustness of the conical probe but also is important in interpreting SECM approach curves at a sharp probe over a soft substrate such as biological samples.

Finally, it should be note that both negative and positive feedback effects at conical electrodes are much smaller than those at disk-like ones (Figs. 7-11b, 7-12). This result indicates that, at a short tip-substrate distance, the tip current at conical electrodes is mainly controlled by diffusion of mediator through the gap between the tip and the substrate. The space domain of the gap is determined not only by the geometry of the insulating layer but also by the tip angle. A smaller feedback is expected with a sharper conical electrode.[10, 11, 23]

7.5.4 SECM Approach Measurements at Smaller Electrodes

Simulations with modified geometry (R=0.156a) as shown in Figure 7-4 was applied for smaller electrode (a < 500 nm). The fitting of the experimental approach curves and theoretical ones are shown in Figure 7-13. It has been noticed that, at smaller electrodes, deviations appear between experimental curves and theoretical one with the simulation based on Figure 7-1. Experimental data agree very well with simulation taking into account the sharpness effect (geometry shown in Figure 7-4) and this confirms that the tip is very sharp: ~ 80 nm in diameter for a conical electrode with base radius of 255 nm (Figure 7-13).

7.5.5 Insulation with Electrophoretic Paint by Multiple Coating

The smallest electrode we can prepare by one-time insulation with electrophoretic paint is 255 nm in radius. White's group has reported fabrication of quasi-hemispherical nano-electrodes from etched Pt wires by electrophoretic paint method.[21] They fabricated electrodes with apparent radii in the range of 2-150 nm by repeated applications of polymer layers. We used a slightly modified version of their electrophoretic paint method. We used the original polymer solution for the first deposition of electrophoretic paint. After insulation, we checked the electrode size by steady-state cyclic voltammetry. Depending on the size of the electrode, we repeated the electrophoretic paint coating by a 1:1 (volume ratio) diluted polymer solution. Figure 7-14 shows the

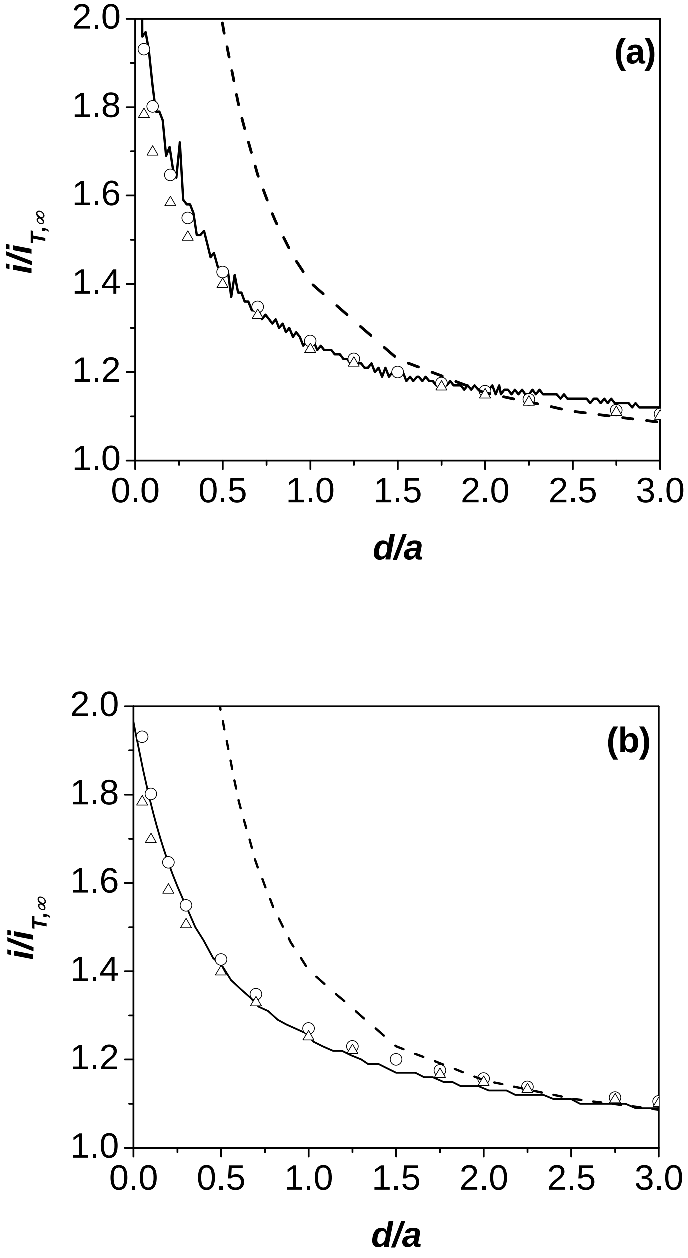

Figure 7-13. Comparison of theoretical (circles) and experimental SECM (solid line) curves at a Pt substrate for conical electrodes with base radius: (a) 255 nm and (b) 382 nm. The geometry for simulation is based on Fig. 7-4 with R=0.156a. The dashed line represents a theoretical approach curve of a disk-like electrode with RG=2. Triangles represent theoretical approach curve at a conical electrode with geometry defined in Fig. 7-1. Solution contained 1 mM 1,1′-ferrocenedimethanol and 0.1 M KCl in water.

steady-state cyclic voltammograms of electrodes prepared by multiple polymer coating. Assuming the electrode maintains its conical shape, we calculated the electrode radius by Eq. 12 to be 180 (Figure 7-14a) and 100 nm (Figure 7-14b), respectively. Because it's not enough to confirm the size and geometry of the prepared electrode with only cyclic voltammetry, we also characterized it with SECM. Unfortunately, we could not obtain apparent feedback changes by approaching the electrode to both an insulating substrate and a conductor. It seems that the metal coated part of the electrode is not protruding from the insulating layer. And from the SEM image (Figure 7-15) taken from an electrode with multiple polymer coatings, it looks more like a recessed electrode. From our results, we also found repeatedly coating polymer is not very controllable and reproducible. Therefore, it is necessary for us to find another option to fabricate nanometer-sized probes.

7.5.6 Gold Quality of the Electrodes

During our experiments, we found out that sometime the electrode surfaces were quite rough after sputtering of gold (Figure 7-16). The cause might be that the pressure of sputter coater 108 auto is not low enough (~ 1e-4 Torr) and the environment is too humid. So we decided to use the Perkin-Elmer 2400 6J sputtering instrument in the cleanroom of Carnegie Mellon University with the capacity of pressure as low as 1e-8 Torr.

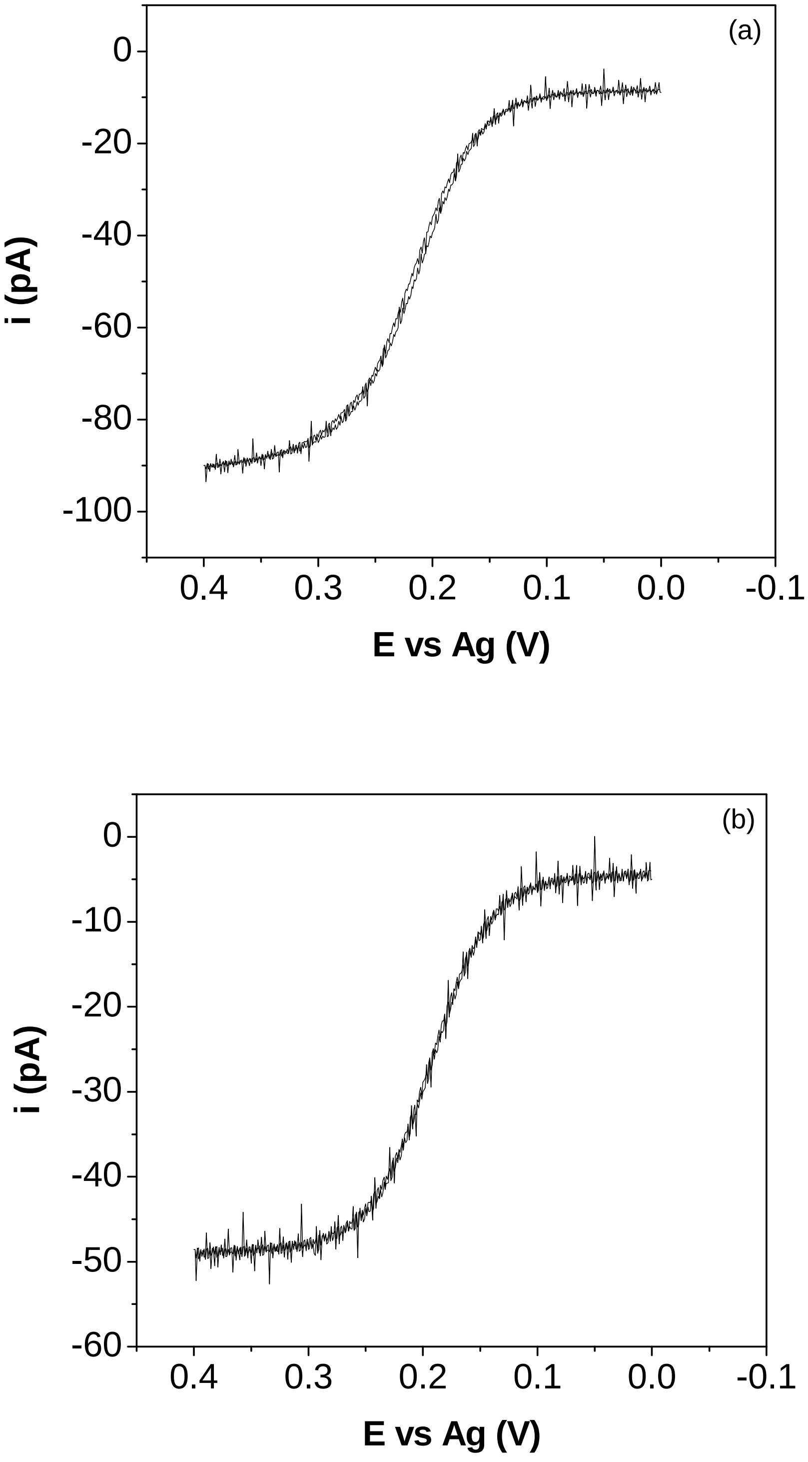

Figure 7-14. Cyclic votammogram from probes prepared by repeated polymer applications in an aqueous solution of 1 mM 1,1′-ferrocenedimethanol and 0.1 KCl. Scan rate 0.01 V/s.

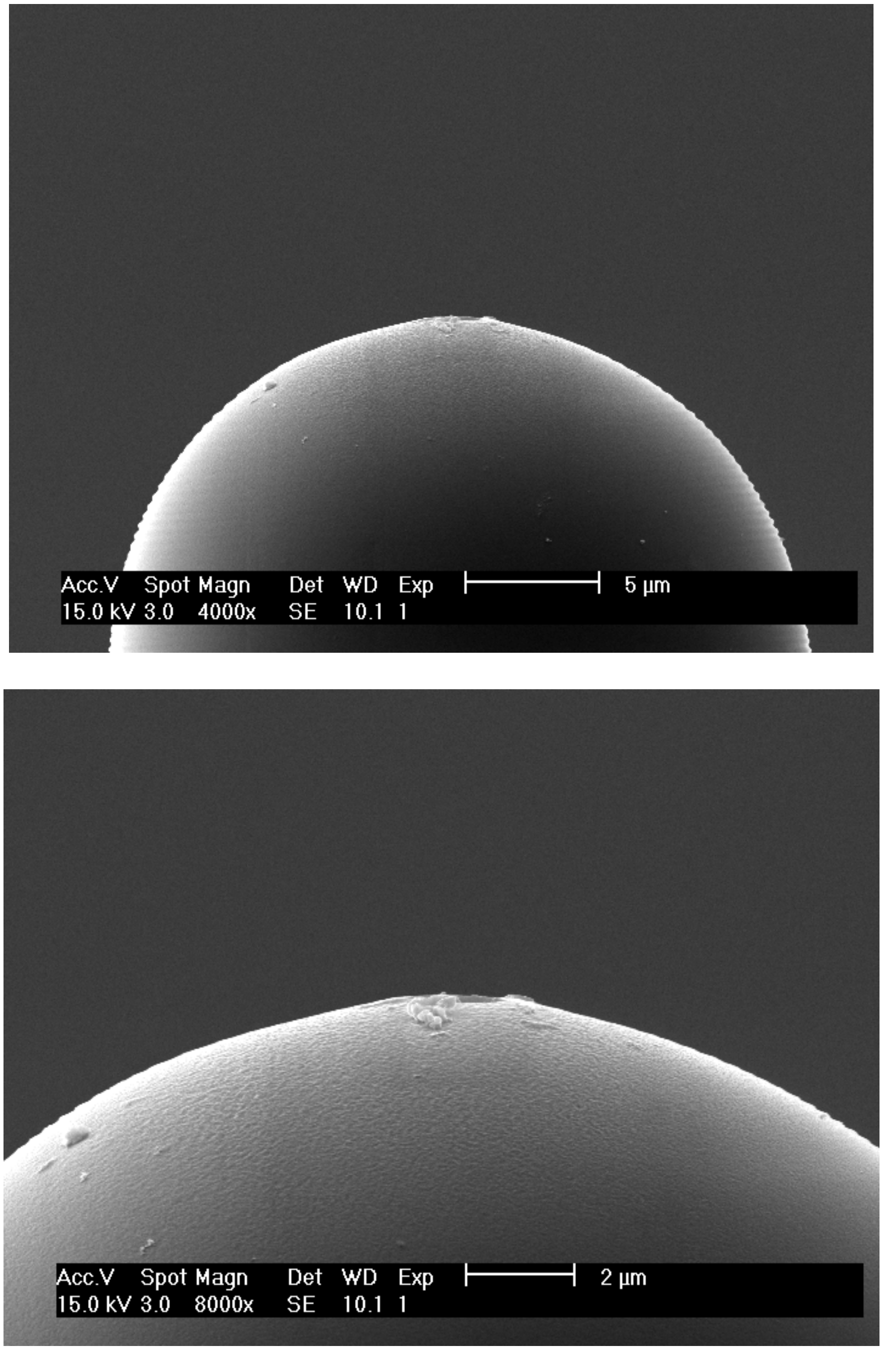

Figure 7-15. SEM images of a probe prepared by multiple polymer coatings.

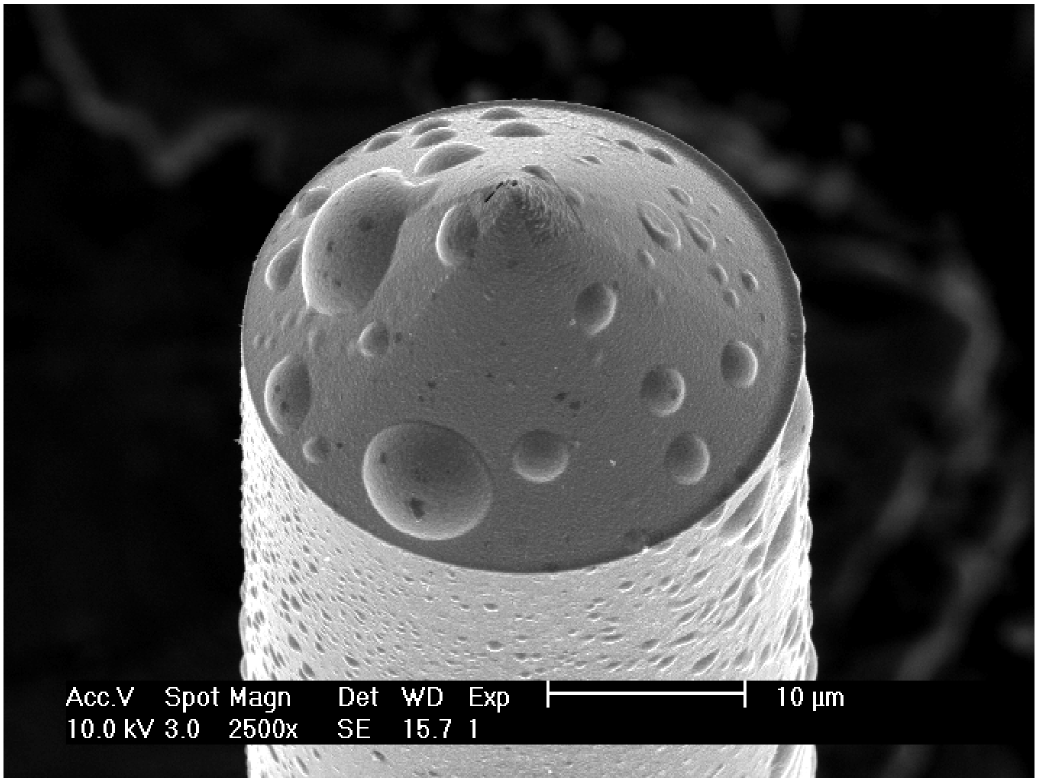

Figure 7-16. SEM image of an electrode with rough gold surface.

7.6 CONCLUSIONS

Selectively etched optical fibers were used as a template of conical microelectrode. The gold coated tapered optical fibers were insulated with electrophoretic paint leaving only tips exposed. The electrode geometry and size were determined by both steady-state cyclic voltammetry and SECM. The experimental approach curve data fit well with theoretical ones, yielding values in the range of 0.255-0.98 and 0.3-1.2 μm for the base radius and height of the conical probes, respectively. The aspect ratio of the conical tip corresponds to the tip angle of 80^0, which is consistent with the tip angle of the tapered optical fiber determined by SEM. This result indicates the geometry of the conical electrode is well controlled by the selective etching technique. Moreoever, the etching technique allows control of tip angle in the range between 14^0 and 180^0.[9] A smaller feedback current, however, will be observed for a conical probe with a smaller tip angle. Both SECM positive and negative feedback effects at the conical probes indicate that the tip current is mainly controlled by the gap between the tip and the substrate, namely, the domain defined by the tip angle and the insulating layer.

It is possible to construct smaller probes by varying the insulating procedure. Multiple coating of electrophoretic paint, however, typically results recessed electrodes, which are not suitable for SECM applications. A more controllable fabrication method is desired to create nanometer-sized probes for SECM.

ACKNOWLEDGEMENTS

The support by National Science Foundation (DBI-0242561) is gratefully acknowledged. We thank Professor Sanford A. Asher and Dr. Xiangling Xu for help with sputter coating, and Mr. Masao Fukuda, Shimizu Co., for providing us with a sample of the electrophoretic paint.

REFERENCES

(1) Kuhn, L. S.; Weber, A.; Weber, S. G. *Analytical chemistry* **1990**, *62*, 1631-1636.

(2) Pennarun, G.; Boxall, C.; O'Hare, D. *Analyst (Cambridge, United Kingdom)* **1996**, *121*, 1779-1788.

(3) Casillas, N.; James, P.; Smyrl, W. H. *Journal of the Electrochemical Society* **1995**, *142*, L16-L18.

(4) James, P.; Casillas, N.; Smyrl, W. H. *Proceedings - Electrochemical Society* **1996**, *95-15*, 425-434.

(5) Lee, Y.; Bard, A. J. *Analytical Chemistry* **2002**, *74*, 3626-3633.

(6) Lee, Y.; Ding, Z. F.; Bard, A. J. *Analytical Chemistry* **2002**, *74*, 3634-3643.

(7) Betzig, E.; Trautman, J. K. *Science* **1992**, *257*, 189-195.

(8) Xiong, H.; Guo, J.; Kurihara, K.; Amemiya, S. *Electrochemistry Communications* **2004**, *6*, 615-620.

(9) Ohtsu, M.; Editor *Near-Field Nano/Atom Optics and Technology*, 1998.

(10) Mirkin, M. V.; Fan, F. R. F.; Bard, A. J. *Journal of Electroanalytical Chemistry* **1992**, *328*, 47-62.

(11) Fulian, Q.; Fisher, A. C.; Denuault, G. *Journal of Physical Chemistry B* **1999**, *103*, 4387-4392.

(12) Zoski, C. G.; Mirkin, M. V. *Analytical Chemistry* **2002**, *74*, 1986-1992.

(13) Mononobe, S.; Ohtsu, M. *IEEE Photonic. Technol. Lett.* **1998**, *10*, 99.

(14) Slevin, C. J.; Gray, N. J.; Macpherson, J. V.; Webb, M. A.; Unwin, P. R. *Electrochemistry Communications* **1999**, *1*, 282-288.

(15) Conyers, J. L.; White, H. S. *Analytical Chemistry* **2000**, *72*, 4441-4446.

(16) Bach, C. E.; Nichols, R. J.; Beckmann, W.; Meyer, H.; Schulte, A.; Besenhard, J. O.; Jannakoudakis, P. D. *Journal of the Electrochemical Society* **1993**, *140*, 1281-1284.

(17) Bach, C. E.; Nichols, R. J.; Meyer, H.; Besenhard, J. O. *Surface & Coatings Technology* **1994**, *67*, 139-144.

(18) Schulte, A.; Chow, R. H. *Analytical Chemistry* **1996**, *68*, 3054-3058.

(19) Denuault, G.; Mirkin, M. V.; Bard, A. J. *Journal of Electroanalytical Chemistry and Interfacial Electrochemistry* **1991**, *308*, 27-38.

(20) Hyk, W.; Nowicka, A.; Stojek, Z. *Analytical Chemistry* **2002**, *74*, 149-157.

(21) Watkins, J. J.; Chen, J. Y.; White, H. S.; Abruna, H. D.; Maisonhaute, E.; Amatore, C. *Analytical Chemistry* **2003**, *75*, 3962-3971.

(22) Kwak, J.; Bard, A. J. *Analytical Chemistry* **1989**, *61*, 1221-1227.

(23) Zoski, C. G.; Liu, B.; Bard, A. J. *Analytical Chemistry* **2004**, *76*, 3646-3654.

(24) Demaille, C.; Brust, M.; Tsionsky, M.; Bard, A. J. *Analytical Chemistry* **1997**, *69*, 2323-2328.

(25) Abbou, J.; Demaille, C.; Druet, M.; Moiroux, J. *Analytical Chemistry* **2002**, *74*, 6355-6363.

(26) Selzer, Y.; Mandler, D. *Analytical Chemistry* **2000**, *72*, 2383-2390.

(27) Mauzeroll, J.; Hueske, E. A.; Bard, A. J. *Analytical Chemistry* **2003**, *75*, 3880-3889.

(28) Lee, Y.; Amemiya, S.; Bard, A. J. *Analytical Chemistry* **2001**, *73*, 2261-2267.

8.0 FABRICATION AND CHARACTERIZATION OF NANOMETER-SIZED PROBES FOR SCANNING ELECTROCHEMICAL MICROSCOPY

8.1 ABSTRACT

We describe a method for fabrication of nanoelectrodes for SECM. The nanoelectrodes are formed from chemically etched optical fibers as a template and coated with a thin gold layer by sputtering. Subsequent deposition of an insulation layer (SiO_2) by plasma enhanced chemical vapor deposition (PECVD) and milling at the tip end by focused ion beam (FIB) yields disk-shaped nanoelectrodes. This approach allows fabrication of nanoelectrodes with controlled size and shape, which will enable high spatial resolution electrochemical imaging by SECM.

8.2 INTRODUCTION

In the previous chapter, the fabrication of conical SECM probes by selective etching and electrophoretic paint techniques was introduced. It proved that the selectively etched optical fiber is a good template for reproducibly preparing sharp tips with defined geometry. Well-defined and reproducible conical electrodes with radius as small as 255 nm were successfully fabricated. However, as fabrication of even smaller electrode was attempted, electrophoretic paint technique was not able to give satisfactory results. By repeatedly depositing electrophoretic paint on the gold-coated fibers, we mostly obtained recessed electrodes. Moreover, the multiple-coating process is not controllable to expose the probe tip smaller than submicrometer in diameter, which has also been found by other researchers.[1]

In this chapter, we present a novel approach to SECM nanoprobe production by nanofabrication, which solves the problem of incapability to control the electrode size and shape by the electrophoretic paint technique. PECVD can provide insulating films with controlled thickness. This technique resolves the frequent problem of pinholes when depositing an insulating film (e.g. SiO_2 and Si_3N_4) on a metal film because it can reduce the stress at the interface between the insulator and the metal by deposition at relatively low temperatures.[2] Hence, we utilized PECVD to deposit a thin SiO_2 layer for insulation of the metal-coated etched optical fiber. FIB milling is a modern technique superb in designing and sculpturing nanometer-sized structures with high precision. Therefore, we applied FIB to modify the tip of the fiber probe to fabricate nanoelectrodes. Here we demonstrate that by coating the selectively etched optical fiber, which has been covered by a conductive layer, with an insulating SiO_2 film, and subsequently cutting off the probe end, it is possible to form a disk-shaped nanoelectrode.

8.3 EXPERIMENTAL

8.3.1 Electrode fabrication

A schematic of the nanoelectrode fabrication process is shown in Figure 8-1. The process is composed of four steps: (1) selectively etched optical fibers are made following the procedures described in the previous chapter; (2) Cr/Au/Cr layers are sputter-coated over the etched optical fiber by a Perkin Elmer 2400 6J Sputtering System (Perkin Elmer, Waltham, MA), the thickness of Au layer is ~100 nm and the thickness of the adhesion Cr layer is ~5 nm; (3) subsequent insulation over the fiber probe is carried out by a P-5000 PECVD system; (4) the end of the fiber tip is removed by a Nova FIB/SEM System (FEI, Hillsboro, OR), yielding a nanoelectrode with defined size and shape.

Details of experimental conditions for sputtering, PECVD, and FIB are given as follows: (a) sputtering: etched optical fibers were mounted vertically by a homemade fiber holder in the sputtering chamber; a 5-nm Cr layer (working pressure, 5 mTorr; RF power, 100 W), a 100-nm Au layer (working pressure, 5 mTorr; DC power, 50 W), and a 5-nm Cr layer were sputter-coated in succession; (b) PECVD: a SiO_2 layer was deposited onto the Cr/Au/Cr-coated optical fibers mounted horizontally at 200°C by reacting trimethylsilane (flow rate, 50 SCCM) and O_2 (flow rate, 500 SCCM) at a pressure of 1 Torr and a RF power of 200 W; next, the optical fibers were flipped over and coated for the other side at the same condition; (c) FIB: the FIB system operates at an acceleration voltage of 30 kV with a gallium liquid-metal ion source and the fiber ends were cut at a beam current of 93 pA.

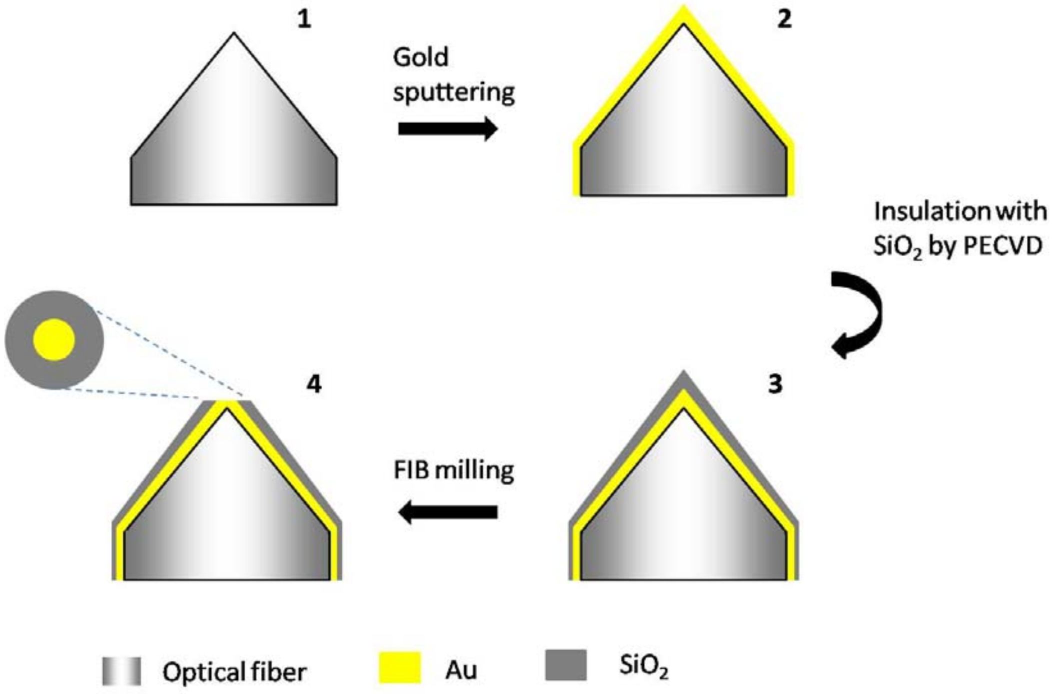

Figure 8-1. Scheme of the nanoprobe fabrication process.

8.3.2 Electrochemical Measurements

For electrochemical measurements, a two-electrode system was used. The working electrode was the prepared tip and the quasi-reference electrode was a silver wire. A CH Instruments (Austin, TX, USA) model 900 was used for all electrochemical measurements.

8.4 RESULTS AND DISCUSSION

8.4.1 Insulation by PECVD

Silicon oxide is commonly used in the micro-fabrication field as an insulating material.[2] We applied PECVD to grow a 100 nm-thick film of SiO_2 on the metal-coated etched optical fiber. Figure 8-2 shows the SEM images of the SiO_2-coated fiber. The fiber is covered by a uniform coating of SiO_2. No evident pinholes are seen throughout the fiber under SEM. In order to assess the insulating process further, I tested the fiber probes electrochemically by approaching the probe from air to an aqueous solution containing 10 mM $Ru(NH_3)_6^{3+}$ and 0.1 M KCl. An approach curve of the SiO_2-coated probe is shown in Figure 8-3. There was no apparent faradic current after the tip approached to the air-solution interface, which indicates that the tip is well-insulated and pinhole-free. Therefore, PECVD yields good insulation for the fiber probes.

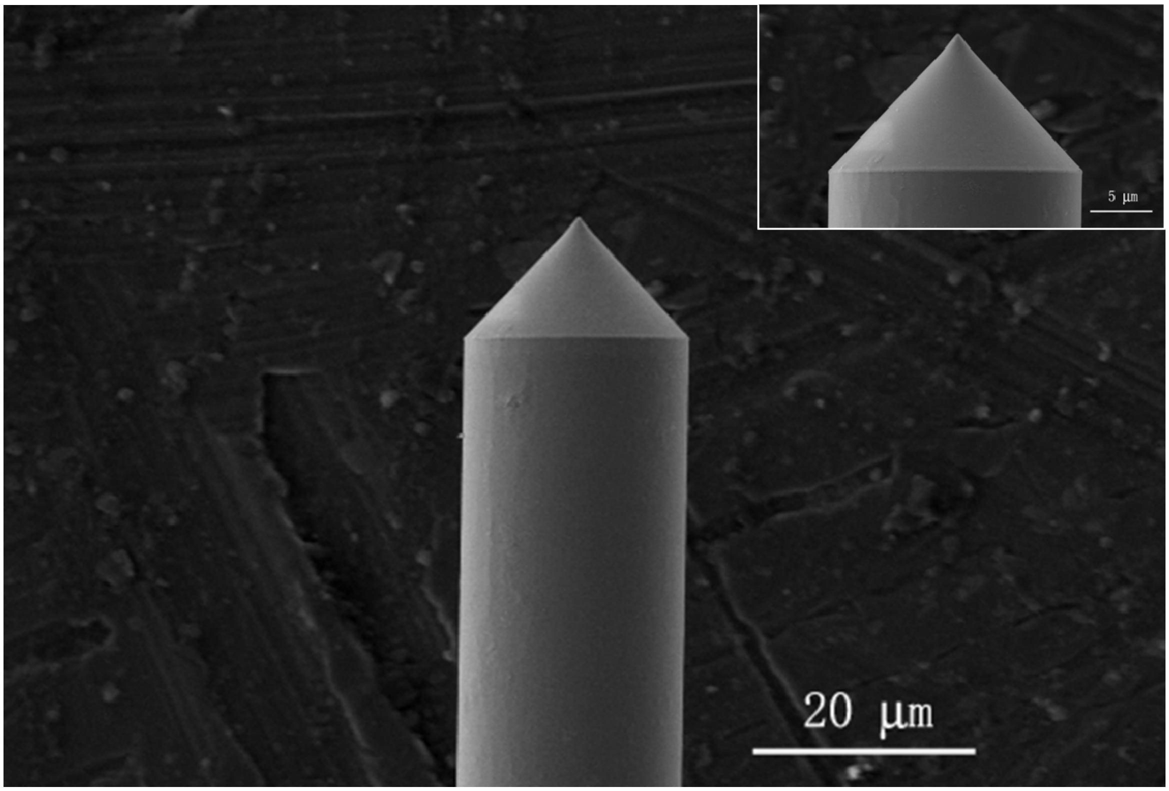

Figure 8-2. SEM image of a fiber probe insulated with SiO_2 by PECVD. Inset is the SEM image of the same probe with a higher magnification.

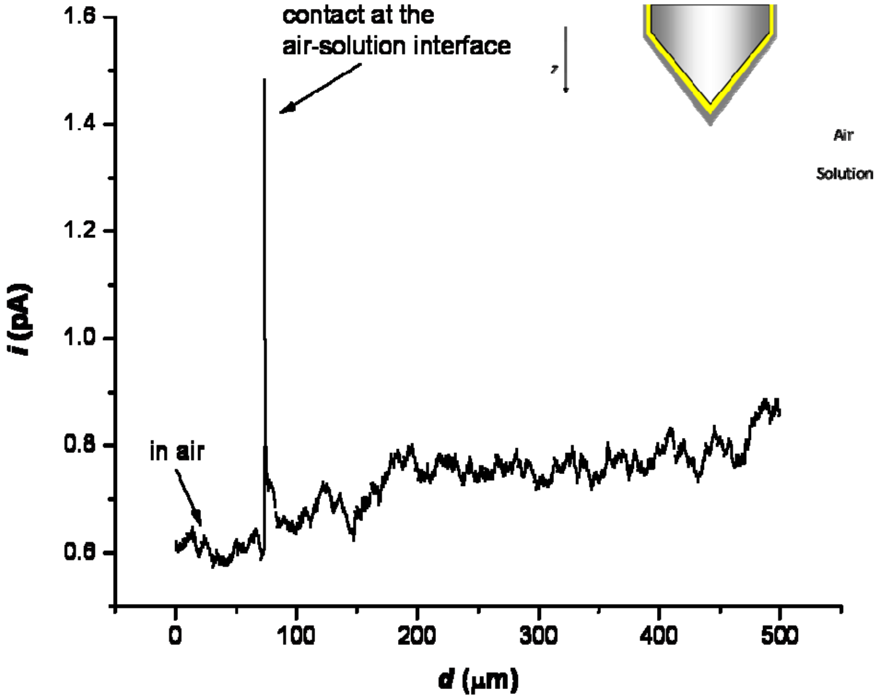

Figure 8-3. Probe approach curve of a SiO_2-coated probe brought from air to a solution containing 10 mM $Ru(NH_3)_6^{3+}$ and 0.1 M KCl.

8.4.2 FIB Milling

The insulated probes were brought under FIB, using a beam direction perpendicular to the probes. Figure 8-4 shows typical SEM images of a fiber probe before (a) and after (b, c) FIB cutting. The disk-shaped gold can be clearly seen from the images. RG of this tip is very small (~ 2) because of the thin insulating film. With this approach, we successfully fabricated disk probes with the tip diameter down to ~ 90 nm.

8.4.3 Steady-state Cyclic Voltammetry

Exposure of a gold layer after FIB milling was also confirmed by cyclic voltammetry carried out in a 30 mM $Ru(NH_3)_6Cl_3$/0.5 M KCl aqueous solution. The cyclic voltammogram of a FIB-milled probe is shown in Figure 8-5. This well-defined sigmoildal cyclic voltammogram represents a good-quality nanoprobe. Calculating from the diffusion-limited steady-state current at this tip for a disk geometry, we obtain that the tip size is about 41.5 nm in radius.

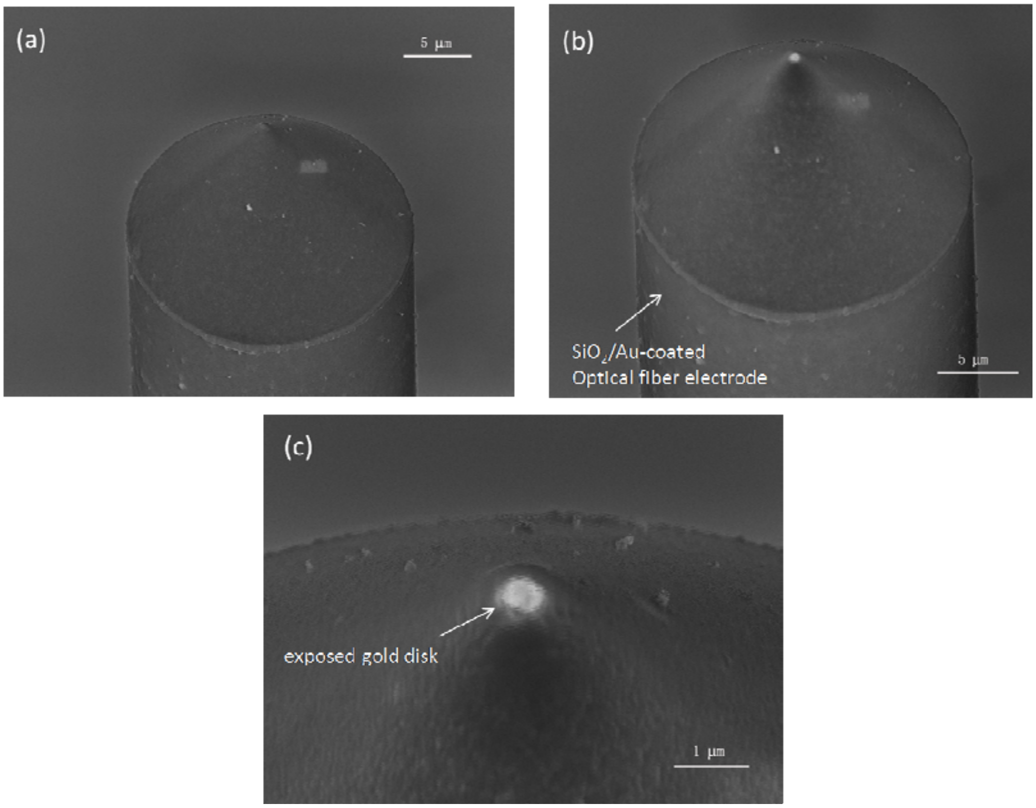

Figure 8-4. SEM images of a fiber probe prior to (a) and after (b, c) FIB milling. (c) is the SEM image with the same probe at a higher magnification.

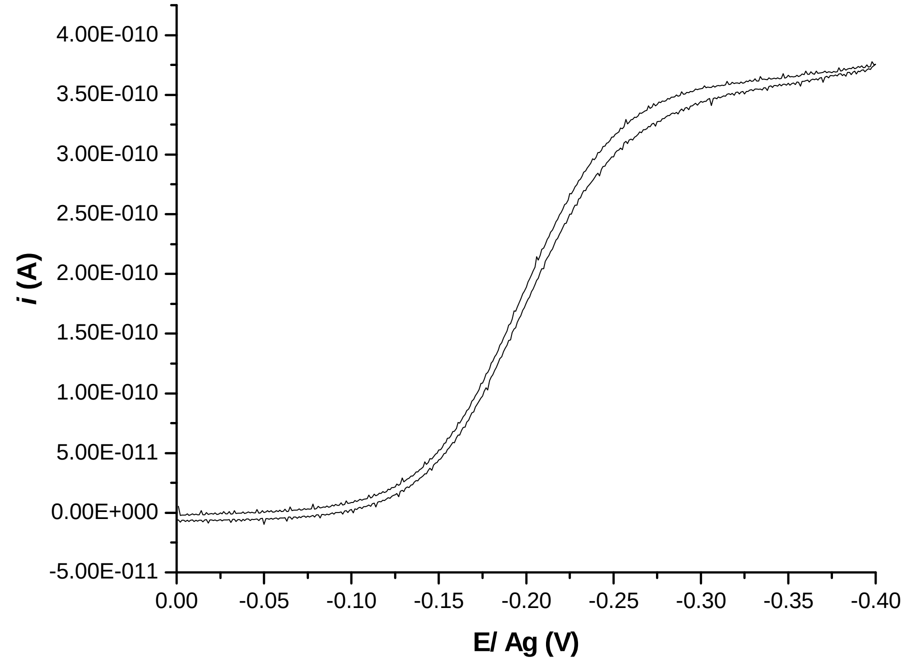

Figure 8-5. Cyclic voltammogram from a disk nanoelectrode in a aqueous solution of 30 mM $Ru(NH_3)_6^{3+}$ and 0.5 M KCl.

8.5 CONCLUSION

We demonstrated a simple but reliable approach to fabricate nanoprobes with controlled electrode diameter and a well-defined disk shape by nanofabrication. The nanoelectrodes with a small RG created in this fashion are suitable for obtaining high-resolution SECM imaging. By adjusting the thickness of the metal layer and insulating coating, we expect that it is possible to fabricate disk-shaped electrode with the diameter below 100 nm. In addition, by varying the ion beam position in milling the optical fiber probe, ring-shaped nanoelectrode can be made in the future, which is especially useful in combined SECM-near-field scanning optical microscopy applications.[3, 4]

SUPPORTING INFORMATION

Figure S 8-1 shows a cross-section SEM image of the fiber probe cut through manually. It is used to access how well we can control the film thickness of both gold and SiO_2 layers by sputtering and PECVD. The thickness of both films is consistent with the values we expected, indicating the fabrication techniques are reliable in controlling the size of the film.

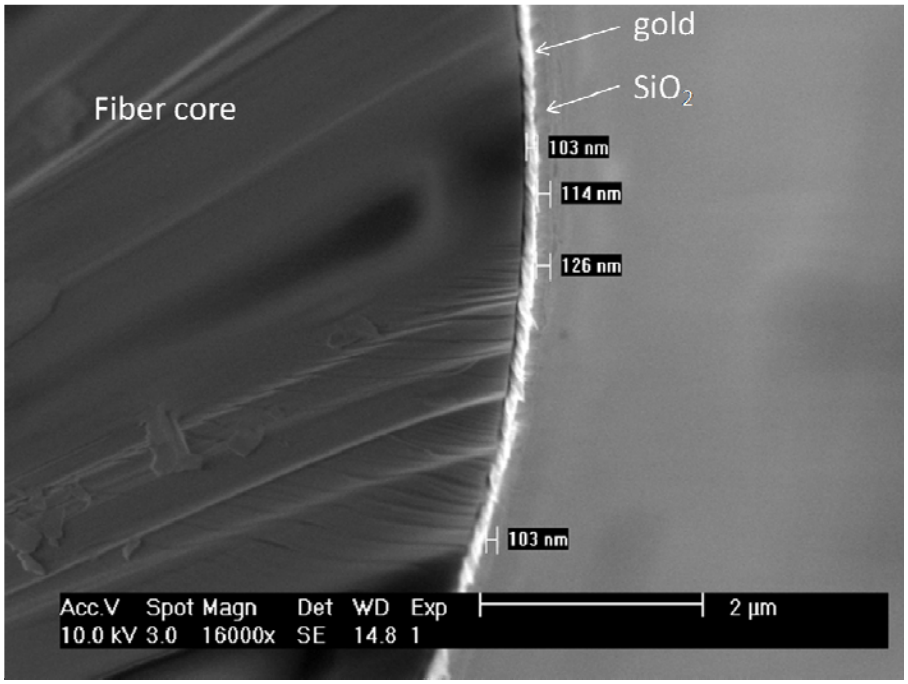

Figure S 8-1. Cross-section SEM image of a SiO_2/Au-coated optical fiber.

ACKNOWLEDGEMENTS

We thank Mr. Guy Lavallee (National Nanotechnology Infrastructure Network, Penn State University) for help with PECVD, Mr. Fred. J. Wiatrowski (Seagate) for help with FIB, and Department of Materials Science and Engineering at University of Pittsburgh for provision of access to the SEM instrument.

REFERENCES

(1) Watkins, J. J.; Chen, J. Y.; White, H. S.; Abruna, H. D.; Maisonhaute, E.; Amatore, C. *Analytical Chemistry* **2003**, *75*, 3962-3971.

(2) Kovacs, G. T. A. *Micromachined Transducers Sourcebook*; McGraw-Hill Companies: New York, 1998.

(3) Lee, Y.; Bard, A. J. *Anal. Chem.* **2002**, *74*, 3626–3633.

(4) Lee, Y.; Ding, Z.; Bard, A. J. *Anal. Chem.* **2002**, *74*, 3634–3643.